



Department: Electrical Engineering

Order N° : / 2021

Defense authorization N°/2021

DOCTORAL THESIS

3rd Cycle Doctoral (D-LMD)

Presented by

Abdelfattah Elhadj BENKHECHIBA

With a view to obtaining the doctoral diploma in 3rd Cycle Doctoral (D-LMD)

Branch: Mechanical Engineering

Specialty: Energetic Mechanics - Mechanical Construction

Topic

Contribution to the numerical homogenization of three dimensional Nano-composites by considering surface effect and the interaction energy

Supported, on 15 /11/ 2020, before the jury composed of:

Last and first name	Grade	Institution of affiliation	Designation
Mr Farid MESSELMY	Professeur	Université of Djelfa	President
Mr Brahim Elkhalil HACHI	Professeur	Université of Djelfa	Supervisor
Mr Mostafa MOUSSAOUI	MCA	Université of Djelfa	Co-Supervisor
Mr Omar ALAOUI	Professeur	Université of Laghouat	Examiner
Mr Yazid DEROUICHE	Professeur	Université of Djelfa	Examiner
Mr HAMMOU Abdelkader Djilali	MCA	Université of Laghouat	Examiner

Djelfa University, FST - 2021

Dedications

To my dear parents for all their sacrifices, their love, their tenderness, their support throughout my studies.

*To my dear brothers and sisters, Mohamed, Said, Mbarka, Houda, Aicha,
To all the moments of my childhood spent with you my dear brothers, as a token of my deep esteem for the help you have given me. May our fraternal bonds be consolidated and perpetuate even more.*

To all my family for their support throughout my university career,

*My dear friends who have supported me of all times: FARHAT Abdelmoumene,
RABOUH Mustapha and LASSALI Youcef.*

*My doctorate colleagues DJELOUD Hamza, RAACH Youcef, LAOUID Ayoub,
KENICH Salem, BELAIBE Baker, et ZERGOT Souad.*

BENKHECHIBA Abdelfattah Elhadj

Acknowledgement

- ◆ Praise be to ALLAH (his Name be glorified) who guided us, and without him we would never have been on the right track. I thank ALLAH for giving me the strength and will that allowed me to continue my studies from primary to university.

- ◆ I would first like to thank, my thesis supervisor Pr. HACHI Brahim ElKhalil, for his patience, his availability and especially his judicious advice, which contributed to my reflection and Co-supervisor Mr. MOUSSAOUI Mostafa who supported, encouraged, and guided throughout my studies, we can forget the teams of the LDMM research laboratory, especially the members of the research team N ° 1 "modelling in structural calculation" Dr. HACHI Dahmane, Dr. KIREM Mohammed Riad and Dr. TAIBI Hadi.

- ◆ I would like to present my warm thanks to Pr. MESSELMY Farid for having accepted to chair my jury, to Pr. ALAOUI Omar , Pr. DEROUICH Yazid and Dr. HAMMOU Abdelkader Djilali for the honor they have given me. 'took an interest in this work and agreed to evaluate it.

- ◆ Finally my thanks to my parents for their constant support and encouragement to have given me a good education, and all the necessary means allowing me to reach this level; my father Abdelbaki and my source of inspiration my mother ZOHRA, my brothers, my sisters.

- ◆ Finally, I thank all those who from far or near have supported me, encouraged me not to be able to name their name.

Nomenclature

σ	Stress tensor
ε	Strain tensor
S	Flexibility tensor
λ, μ	Lamé coefficients
$\bar{\sigma}$	Average stress field
$\bar{\varepsilon}$	Mean field of deformation
T	Stress vector
n	The normal
u	Displacement field
σ^{per}	Periodic stress field
ε^{per}	Periodic strain field
u^{per}	Periodic displacement field
ε^m	The strain tensor of the matrix
ε^f	The strain tensor of the fibre
σ^m	The stress tensor of the matrix
σ^f	The stress tensor of the fibre
E_1	Young's modulus in the direction 1
ν_{12}	Poisson's ratio between directions 1 and 2
E_2	Young's modulus in the direction 2
ν_{23}	Poisson's ratio between directions 2 and 3
G_{12}	The shear modulus between directions 1 and 2
G_{23}	The shear modulus between directions 2 and 3
$\sigma_s^{(i)}$	Surface stress tensor
P	Projection matrix
$\bar{\mathbf{n}}(\mathbf{x})$	Unit normal vector
F	Applied effort
\mathbb{C}	Volume properties matrix
\mathbb{C}^s	Surface properties matrix
ϵ^s	Surface strain tensor
K_{IJ}	Volume stiffness matrix
K_{IJ}^s	Surface stiffness matrix
N	Form function
M_p	Elementary projection matrix
B_I	Matrix of derivatives of form functions
B_I^{enr}	Matrix of derivatives of enrichment form functions

$\widehat{\mathbf{N}}_I$	Enrichment form functions
λ_{eff}, μ_{eff}	Effective lamé coefficients
K_{eff}	Compressibility effective modulus
\mathbf{K}'_S	Surface energy
\mathbf{f}	Volume fraction
\mathbf{f}^S	Surface fraction
E_{int}	The interaction energy

List of Figures

CHAPTER 1: State of the art and bibliographic research	
Fig. 1.1: Composite material	9
Fig. 1.2: Macroscopic crack	17
Fig. 1.3: The three modes of a fracture of a crack	20
CHAPTER 2: Generalities on Homogenization	
Fig. 2.1: The principle of homogenization	27
Fig. 2.2: Choice of REV	28
Fig. 2.3: REV's Configurations: a) Square arrangement, b) Hexagonal arrangement	32
Fig. 2.4: Homogenization flow chart	38
CHAPTER 3: XFEM coupled with multi Level-set(s) technique and presentation of the elaborated code	
Fig. 3.1: Different types of XFEM enrichments	44
Fig. 3.2: Subdivision of the tetrahedron cut element: a) into 4 sub-elements, b) into 6 sub-elements.	50
Fig. 3.3: Description of Level-set linear interpolation.	50
Fig. 3.4: 3D representation of a crack by Level-Set.	51
Fig. 3.5: Flow chart of our calculation code.	53
Fig. 3.6: Numbering of elements and nodes.	55
Fig. 3.7: Under splitting and distribution of gauss points	57
Fig. 3.8: Insertion of an element matrix in the global array.	59
CHAPTER 4: Validation of the code and parametric studies in displacement analysis and homogenization without surface effect	
Fig. 4.1: (a) Description of the physical problem, (b) Level-set within mesh.	65
Fig. 4.2: Evolution of the radial displacement U_r along the z-axis.	65
Fig. 4.3: (a) Cube containing a semi-circular surface crack, (b) Level-set within mesh for XFEM, (c) Mesh for FEM.	66
Fig. 4.4: Evolution of displacement along the y-axis by X-FEM and FEM.	66
Fig. 4.5: Cube containing a Crossing crack.	67
Fig. 4.6: Evolution of displacement along the y-axis by X-FEM and FEM.	67
Fig. 4.7: Cylinder containing an annular surface.	68
Fig. 4.8: Evolution of displacement along the x-axis.	69
Fig. 4.9: Cylinder containing a crack in elliptical form subjected to a tensile loading.	69
Fig. 4.10: Evolution of displacement along the y-axis by X-FEM and FEM.	70
Fig. 4.11: Flattening of a cylinder in a REV.	71
Fig. 4.12: Evolution of K_{ad} of a flattened cylinder with respect to a crossing crack.	71
Fig. 4.13: Flattening of a sphere in a REV.	71
Fig. 4.14: Evolution of K_{ad} of a flattening sphere with respect to a crack.	72
Fig. 4.15: Geometry of the problem.	72
Fig. 4.16: Evolution of K_{ad} versus the crack radius.	73
CHAPTER 5: Homogenization of nanocomposite materials with surface effect	
Fig. 5.1: Multiphase domain with coherent open and close interfaces.	76

Fig. 5.2: Flow chart of our calculation code.	83
Fig. 5.3: Cylindrical fiber into cubic matrix: a) Geometrical configuration; b) Level-set crossing the mesh.	85
Fig. 5.4: Indicator β versus fiber size.	86
Fig. 5.5: Indicator β versus thickness.	86
Fig. 5.6: Relative energy error norm for the cylindrical inclusion problem: (a) versus number of elements; (b) versus the dimensionless mesh size	87
Fig. 5.7: Dimensionless transverse bulk modulus versus void radius: a) with the first REV's configuration; b) with the second REV's configuration.	90
Fig. 5.8: Dimensionless transverse bulk modulus with respect to volume fraction: a) with the first REV configuration; b) with the second REV configuration.	91
Fig. 5.9: Dimensionless effective longitudinal bulk modulus: a) with respect to void size; b) with respect to volume fraction.	92
Fig. 5.10: Dimensionless effective bulk moduli below nanoscale: (a) transverse modulus; (b) longitudinal modulus.	93
Fig. 5.11: Dimensionless effective bulk moduli with amplifying surface characteristics: (a) transverse modulus; (b) longitudinal modulus	94
Fig. 5.12: Orthotropic ratio for theoretical situations: (a) below nanoscale; (b) with amplifying surface characteristics.	95
Fig. 5.13: Spherical void with coherent interface: (a) Into cylindrical matrix; (b) Into cubic matrix; (c) Into spherical matrix.	96
Fig. 5.14: Dimensionless effective bulk modulus for different REV configurations and $K_s' > 0$: a) with respect to void size; b) with respect to volume fraction.	97
Fig. 5.15: Dimensionless effective bulk modulus for different REV's configurations and $K_s' < 0$: a) with respect to void size; b) with respect to volume fraction.	98
Fig. 5.16: Dimensionless effective bulk modulus for different REV's configurations and $K_s' = 0$: a) with respect to void size; b) with respect to volume fraction.	99
Fig. 5.17: Progressive flattening of spherical void in an REV subjected to periodic conditions.	100
Fig. 5.18: Dimensionless linear invariants versus flattening coefficient for different surface fractions.	102
Fig. 5.19: Progressive flattening of cylindrical void in an REV subjected to periodic conditions.	103
Fig. 5.20: Dimensionless linear invariants versus flattening coefficient for different surface fractions.	105
Fig. 5.21: Convergence test for $f_s = 0.3$ and $F_{apl} = 20$: (a) For flattened sphere; (b) For flattened cylinder.	105
<hr/>	
CHAPTER 6: The interaction energy between nanovoids with surface effect	
Fig. 6.1: Scheme of the interaction energy E_{int} between two nanovoids in an infinite.	110
Fig. 6.2: Discretization of the interaction energy between two nanovoids.	111
Fig. 6.3: (a) infinite system with two cylindrical voids, (b) Case double symmetry with internal pressure, (c) Case double symmetry with periodic condition.	112
Fig. 6.4: Variation of the interaction energy E_{int} as a function of the distance D between	112

two nanovoids with internal pressure.

Fig. 6.5: Infinite system with two cylindrical voids and different internal pressure. 114

Fig. 6.6: Variation of the E_{int} between two cylindrical nanovoids with different pressure as a function of distance D and surface effect is ($K'_S = 0$): (a) $p_2/p_1 < 1$, (b) $p_2/p_1 > 1$. 114

Fig. 6.7: Variation of the E_{int} between two cylindrical nanovoids with different pressure as a function of distance D and surface effect is positive ($K'_S > 0$): (a) $p_2/p_1 < 1$, (b) $p_2/p_1 > 1$. 114

Fig. 6.8: Variation the logarithm scale of E_{int} between two cylindrical nanovoids with different values of p_1 as a function of logarithm scale of p_2/p_1 in the case of $D=2.1\text{nm}$: (a) $K'_S=0$, (b) $K'_S>0$. 115

Fig. 6.9: Infinite system with two cylindrical voids of different sizes. 116

Fig. 6.10: Variation of the E_{int} between two cylindrical nanovoids of different size versus distance D^* : (a) $K'_S = 0$, (b) $K'_S > 0$. 117

Fig. 6.11: (a) REV with two spherical nanovoids, (b) One-quarter of REV caused by double symmetry. 118

Fig. 6.12: Variation of the interaction energy in terms of distance D between two nanovoids in spherical form: (a) tensile force in the direction of the convergence of the two voids, (b) tensile force perpendicular to the direction of convergence of the two voids and in the direction of the y-axis, (c) tensile force perpendicular to the direction of convergence of the two voids and in the direction of the z-axis. 119

Fig. 6.13: Dimensionless effective bulk modulus with distance D : (a) $K'_S = 0$, (b) $K'_S > 0$. 119

Fig. 6.14: (a) Domain with two cylindrical voids, (b) One-quarter of REV caused by double symmetry. 120

Fig. 6.15: Variation of the interaction energy in terms of distance D between two nanovoids in cylindrical form: (a) Tensile force in the direction of the convergence of the two voids, (b) tensile force perpendicular to the direction of convergence of the two voids and in the direction of the y-axis, (c) tensile force perpendicular to the direction of convergence of the two voids and in the direction of the z-axis. 121

Fig. 6.16: Dimensionless effective bulk modulus K^* as a function of the distance D between two nanovoids in cylindrical form: (a) $K'_S = 0$, (b) $K'_S > 0$. 122

Fig. 6.17: (a) REV with eight spherical nanovoids, (b) One-eighth of REV caused by triple symmetry. 122

Fig. 6.18: Variation of the interaction energy versus a distance between eight nanovoids in spherical form. 123

Fig. 6.19: Dimensionless effective bulk moduli with distance D for the case with eight spherical nanovoids: (a) $K'_S = 0$, (b) $K'_S > 0$. 123

Fig. 6.20: (a) Infinite domain with fourth cylindrical nanovoids, (b) One-quarter of REV caused by double symmetry. 124

Fig. 6.21: Variation of the interaction energy versus a distance between four voids in cylindrical form: (a) Tensile force in the direction x-axis and y-axis. (b) Tensile force perpendicular to the direction of convergence of the four voids and in the direction of the z-axis. 125

Fig. 6.22: Dimensionless effective bulk moduli with distance D : (a) $K'_S = 0$, (b) $K'_S > 0$.	126
Fig. 6.23: Four examples for the configuration 1, in order to spherical nanovoids randomly.	129
Fig. 6.24: Four examples for the configuration 2, in order to spherical nanovoids randomly.	129
Fig. 6.25: Four examples for the configuration 3, in order to spherical nanovoids randomly.	130
Fig. 6.26: Convergence of the dimensionless linear invariant A_1^* for three configurations versus number of realizations: (a) $K'_S = 0$, (b) $K'_S > 0$.	130
Fig. 6.27: Convergence of the dimensionless bulk modulus K^* for three configurations versus number of realizations: (a) $K'_S = 0$, (b) $K'_S > 0$.	131
Fig. 6.28: Convergence of the dimensionless elastic constants ($c_{11}^*, c_{22}^*, c_{33}^*$) for three configurations versus number of realizations: (a) $K'_S = 0$, (b) $K'_S > 0$.	131
Fig. 6.29: Convergence of the dimensionless elastic constants ($c_{12}^*, c_{13}^*, c_{23}^*$) for three configurations versus number of realizations: (a) $K'_S = 0$, (b) $K'_S > 0$.	131
Fig. 6.30: Convergence of the dimensionless elastic constants ($c_{44}^*, c_{55}^*, c_{66}^*, \bar{\mu}^*$) for three configurations versus number of realizations: (a) $K'_S = 0$, (b) $K'_S > 0$.	132
Fig. 6.31: Four examples for the configuration 1, in order to 30 cylindrical nanovoids randomly.	134
Fig. 6.32: Four examples for the configuration 2, in order to 30 cylindrical nanovoids randomly.	134
Fig. 6.33: Four examples for the configuration 3, in order to 30 cylindrical nanovoids randomly.	135
Fig. 6.34: Convergence of the dimensionless linear invariant A_1^* for three configurations versus number of realizations: (a) $K'_S = 0$, (b) $K'_S > 0$.	135
Fig. 6.35: Convergence of the dimensionless bulk modulus K^* for three configurations versus number of realizations: (a) $K'_S = 0$, (b) $K'_S > 0$.	137
Fig. 6.36: Convergence of the dimensionless elastic constants (c_{11}^*, c_{22}^*) for three configurations versus number of realizations: (a) $K'_S = 0$, (b) $K'_S > 0$.	137
Fig. 6.37: Convergence of the dimensionless elastic constant (c_{33}^*) for three configurations versus number of realizations: (a) $K'_S = 0$, (b) $K'_S > 0$.	137
Fig. 6.38: Convergence of the dimensionless elastic constants (c_{13}^*, c_{23}^*) for three configurations versus number of realizations: (a) $K'_S = 0$, (b) $K'_S > 0$.	137
Fig. 6.39: Convergence of the dimensionless elastic constant (c_{12}^*) for three configurations versus number of realizations: (a) $K'_S = 0$, (b) $K'_S > 0$.	137
Fig. 6.40: Convergence of the dimensionless elastic constants ($c_{44}^*, \bar{\mu}^*$) for three configurations versus number of realizations: (a) $K'_S = 0$, (b) $K'_S > 0$.	138
Fig. 6.41: Convergence of the dimensionless elastic constants (c_{55}^*, c_{66}^*) for three configurations versus number of realizations: (a) $K'_S = 0$, (b) $K'_S > 0$.	138

SUMMARY

General introduction	2
<hr/>	
CHAPTER 1: State of the art and bibliographic research	
1.1 Composite materials	8
1.1.1 Definition	8
1.1.2 General Characteristics	9
1.1.3 Classification of composite materials	11
1.1.3.1 Classification according to the form of the constituents	11
1.1.3.1.1 Fibre composites	11
1.1.3.1.2 Particle composites	12
1.1.3.2 Classification according to the nature of the constituents	13
1.1.4 Volume fraction and mass fraction	14
1.1.4.1 Introduction	14
1.1.4.2 Volume fraction	14
1.1.4.3 Surface fraction	14
1.1.4.4 Mass fraction	14
1.1.5 The presence of porosity	15
1.1.6 Nano-materials	15
1.2 History and theory of fracture mechanics	16
1.2.1 Development and history of fracture mechanics	16
1.2.2 General on fractures by cracking	18
1.2.3 The three modes of a fracture of a crack	18
1.2.3.1 Mode I or opening mode (tensile test):	19
1.2.3.2 Mode II or plan sliding mode (shear test):	19
1.2.3.3 Mode III or anti-plan sliding mode (torsion test):	20
1.3 The Historic of different numerical modelling methods	21
1.3.1 The meshless method:	21
1.3.1.1 Using the meshless method:	21
1.3.2 The finite element method FEM:	22
1.3.3 The extended finite element method XFEM	22
<hr/>	
CHAPTER 2: Generalities on Homogenization	
2.1 State of the art	25
2.2 Behaviour law	25
2.3 Concept of homogenization	27
2.3.1 Representative Elementary Volume (REV)	27
2.3.2 Homogenization and boundary conditions	28
2.4 Homogenization based on the analytical approach	29
2.4.1 Mean field theory	29
2.4.1.4 Reuss Model	31
2.4.1.5 Voigt Model	31
2.4.2 Homogenization based on the numerical approach	31
2.4.2.1 Homogenization configurations	31
2.4.2.2 Boundary conditions applied to REV	33
2.4.3 Direct simulation of the microstructure	34
2.5 Homogenization flowchart	38

2.6	Conclusion	39
-----	------------	----

CHAPTER 3: XFEM coupled with multi Level-set(s) technique and presentation of the elaborated code

3.1	The extended finite element method (XFEM)	42
3.1.1	Implementation of the XFEM method	42
3.1.2	The enrichment of inclusion	42
3.1.3	The enrichment of void	43
3.1.4	The enrichment of crack	43
3.2	Application of the XFEM	44
3.3	The Level-Set method	46
3.3.1	The coupling of the Level-Set technique with the XFEM method	46
3.3.2	Description of a crack by LSM	51
3.4	Presentation of the compute code without surface effect	52
3.4.1	Flow chart of our compute code	52
3.4.2	Presentation of the developed program levels	54
3.4.3	Design and definition of geometry and meshing parameters by G-mesh	54
3.4.4	The numbering of elements and nodes	55
3.4.5	Construction of elementary stiffness matrices	56
3.4.6	Assembly procedure (Location of K_e)	58
3.4.7	Resolution of the System	59
3.4.8	Calculation of strains and stresses	60
3.4.9	Homogenization computing	60
3.5	Conclusion	61

CHAPTER 4: Validation of the code and parametric studies in displacement analysis and homogenization without surface effect

4.1	Validation of the calculation code	64
4.1.1	Spherical inclusion in cube subjected to axial tensile load	64
4.1.2	Semi-circular surface crack into cube under tension	65
4.1.3	Crossing crack into cube under tension	67
4.1.4	Annular surface crack into a cylinder under tension	68
4.1.5	Elliptical crack forms into a cylinder under tension	69
4.2	Parametric study for homogenization	70
4.2.1	Flattened cylindrical void with respect to a crossing crack	70
4.2.2	Flattened spherical void with respect to a circular crack	71
4.2.3	Influence of the size effect of the crack	72
4.3	Conclusion	73

CHAPTER 5: Homogenization of nanocomposite materials with surface effect

5.1	Theoretical model	76
5.2	Flow chart of elaborated code with surface effect	82
5.3	Applications and numerical results	84
5.3.1	Cylindrical inclusion submitted to an Eigen-strain	84
5.3.2	Effective behavior of REV containing cylindrical void	89
5.3.3	Spherical void with coherent interface and different surrounding material	96

	shapes	
5.3.4	Effect of flattening of nanovoids	99
5.3.4.1	Spherical void flattened to a penny shaped crack	99
5.3.4.2	Cylindrical void flattened to a through straight crack	102
5.3.4.3	Mesh refinement effect for flattening problem	105
5.4	Conclusion	106
<hr/>		
	Concluding remarks and outlook	108
	References	112
	Appendix A1	116
	Appendix A2	118
<hr/>		

General Introduction

General Introduction

The presence of heterogeneities whose mechanical behavior differs from that of the surrounding material, the matrix, has an influence on the overall behavior of a material. The study of such heterogeneous materials has several fields of application. Composite materials reinforced by inclusions or fibers, the appearance of micro heterogeneities within a material during its development or heat treatments are examples. In all these cases, we want to know the mechanical properties of the two-phase material but for different purposes. For composites, for example, it is desired to precisely improve certain overall elastic proprieties.

The advent of nanotechnology enables the fabrication of various nanostructured material and nanosized devices such as nanobeam, nanocomposites, and NEMS (Nano Electro-Mechanical systems). Compared with their bulky counterparts, these systems may show very enhanced physical properties like higher elastic stiffness, electrical and thermal conductivities. This property enhancement is related to role assigned to the surface of the nanoobject in these systems. In fact, as the number of atoms near the surface/interface in these nanostructured materials is relatively large compared to the total number of atoms, the surface/interface starts to have a specific behavior that affects significantly the properties of the nano particle or the nanostructured material [1]. This specific behavior of the surface/interface is materialized by a proper constitutive law like the one established/investigated by Miller and Shenoy [2] at the free surface of nanovoids in aluminum matrix as example. The results regarding the surface constitutive law obtained by Miller and Shenoy have been used in many works in literature and in the present study as well. The investigations of these researchers suggest that the modification of the crystallographic orientation leads theoretically to different free surface behavior. Hence, it could be possible to tailor the surface structure in order to get particular behavior by chemical functionalization [3]. It will then be possible to obtain novel and unusual effective behavior of the nanostructured material as it was evidenced in 2D by Duan et al. [4] and Kired et al. [5], and once more in the present work following a 3D implementation. In Duan et al. [4] and Kired et al. [5] the unusual behavior consists in a nanoporous materials whose stiffness matches or even exceeds that of the parent materials. In the present work we will retrieve thus unusual behavior. The 3D

General Introduction

implementation enables to show another unusual property: a nanoporous material expected to be orthotropic turns pseudo isotropic because of the effect of the surface energy of nanovoids. This may enable considerable reduction in size and weight of structural elements, and tailoring the material properties without compromising their stiffness and other important properties. Moreover, the 3D modeling carried out here allowed to tackle several extensions and generalizations of some previous works in the literature performed in 2D context. Among these works, there is that of Yvonnet et al. [6] for which heterogeneities are limited to inclusions and voids, that of Farsad et al. [7] which addressed crack and decohesion problems in 2D, and the work of Kired et al. [5] where the flattening of voids to crack-like and the effect of size, number and orientation of voids and cracks were addressed in 2D. Hence, the 3D modeling sought here aims for handling and analyzing 3D “real” problems without going through 2D simplifications such as those used in [4-6]. Indeed, in these references cracks were presented by lines and the cylindrical or spherical voids/inclusions by circles, provided that the 2D context of plane strain, plane stress or axisymmetric states is admitted. Except the work of Chatzigeorgiou et al. [8] in which several types of interface models of discontinuities were treated analytically, it was not possible to find in the literature 3D numerical studies of elasticity problems. This was also mentioned by Kushch et al.[9], who conducted an analytical 3D study on the interaction between interfaces of nanoheterogeneities. Besides, the few 3D studies found were devoted to the analysis of thermal conductivity [10] and piezoresistivity [11-13] of nanocomposites.

The main objective of the first part of this work (chapter 4 and 5) is the numerical study in 3D of the effect of nano-heterogeneities on the effective stiffness of medium hosting such nano-heterogeneities. For this purpose, the mechanical equilibrium equation of the bulk material were solved in Matlab® in conjunction with the equations of surface equilibrium of Laplace-Young equations for coherent interfaces [8,14-15]. This has been achieved by using eXtended Finite Element Method (XFEM) based on “the partition of unity” concept and the Level-Set function method (LSM), [6,10,16-22]. The implementation of the problem leads to a 3D numerical simulation tool that was employed to carry out several parametric studies. Note that the free software Gmsh® [23] was used to perform the geometric modeling and the meshing parts. The applications carried out concern the evaluation of the effective properties of a medium containing single (which can be multiple) nano-inclusion/void, which can tend towards crack by

General Introduction

successive flattening without remeshing. This latter functionality becomes possible thanks the combination of the XFEM (which becomes FEM for voids as the enrichment is disabled) and the technique of Level-Set Method (LSM) [6,10,16-22].

To show the usefulness of the proposed 3D modeling in numerical homogenization of nanostructures, various problems have been addressed, including validation, for which the analytical solution concerning effective bulk moduli is available. Some extensions are also discussed, such as the stiffness and the orthotropic ratio analysis of the composite processed for two theoretical cases; by going down below the nano scale or by amplifying the surface elastic parameters of the interface. This latter case was also recently addressed by Chatzigeorgiou et al. [8] in order to show the influence of interface proprieties on the effective behavior of nano composites. In these tests, it is found possible to get composites stiffer than their parent materials in different directions (parallel and perpendicular to cylindrical void orientation), and/or to have a constant longitudinal stiffness along these directions (pseudo isotropy). This could be interesting if one manages to concretize these tests by passing from the theory to the practice, considering its technological interests. Quoting among them the gain in weight without compromising stiffness and/or insuring a pseudo-isotropic behavior.

The other type of treated problems concerns the flattening of the cylindrical or spherical voids and its influence on the overall effective behavior of the composite as well as the influence of the surface energy versus the degree of flattening until its limit case, i.e. a crack (instead of a void). The evolution of the global behavior is followed by evaluating the effective elasticity stiffness matrix of the composite as well as the two linear elastic invariants, defined by Ahmed [24], comprising different types of stiffness (longitudinal, transversal and shear modulus).

After that in the last part of this work we are care of the interaction energy effect between nanovoids under pressure and periodic conditions and analyze the effect of the random nanostructure on the effective behavior of nanomaterials. This is done by evaluation of the linear elastic invariant A_1 , the effective compressibility modulus K_{eff} and elastic constants for the C_{eff} matrix.

In summary, the major contributions of the present work are:

General Introduction

- Full 3D mechanical homogenization of nanostructured medium containing different kinds of heterogeneities (void, inclusion and/or crack) with surface energy contribution, by XFEM/FEM combined with Level-Set technique.

- Parametric studies on the effective 3D behavior of nanocomposite/porous medium are carried out without assumption on the dimensionality of the problem. The examined parameters are: the size of heterogeneity, its volume fraction, the sign of surface elastic constants, the shape of the surrounding material or the Representative Elementary Volume (REV), the type of boundary conditions applied to REV and the flattening rate of heterogeneities.

- Analyzing the link between flat voids and cracks of comparable sizes regarding the influence of the surface energy on the effective behavior.

- Simulating particular and unusual cases where the nanoporous medium can be stiffer than its parent or when the material initially orthotropic becomes pseudo-isotropic thanks to the surface energy effect.

- Confining the interaction energy effect on nanoporous materials behavior with organized and randomized repartitions of voids.

This thesis is organized in 6 chapters as follows: in chapter 1, State of the art and bibliographic research on the composite materials, fracture mechanics and numerical modelling methods. Then in chapter 2: generalities on homogenization. In chapter 3, the XFEM discretization of the mathematical model is detailed, combined with the Level Set technique. In chapter 4 5 and 6 respectively, we presented the efficiency of elaborate calculation code without surface effect after that the numerical homogenization procedure within surface effect, and in the last part the effect of the interaction energy in the nanostructures behavior. This thesis is ended by general concluding remarks and outlooks.

CHAPTER 1

State of the art and bibliographic research

CHAPTER 1

State of the art and bibliographic research

1.1	Composite materials	8
1.1.1	Definition	8
1.1.2	General Characteristics	9
1.1.3	Classification of composite materials	11
1.1.3.1	Classification according to the form of the constituents	11
1.1.3.1.1	Fibre composites	11
1.1.3.1.2	Particle composites	12
1.1.3.2	Classification according to the nature of the constituents	13
1.1.4	Volume fraction and mass fraction	14
1.1.4.1	Introduction	14
1.1.4.2	Volume fraction	14
1.1.4.3	Surface fraction	14
1.1.4.4	Mass fraction	14
1.1.5	The presence of porosity	15
1.1.6	Nano-materials	15
1.2	History and theory of fracture mechanics	16
1.2.1	Development and history of fracture mechanics	16
1.2.2	General on fractures by cracking	18
1.2.3	The three modes of a fracture of a crack	18
1.2.3.1	Mode I or opening mode (tensile test):	19
1.2.3.2	Mode II or plan sliding mode (shear test):	19
1.2.3.3	Mode III or anti-plan sliding mode (torsion test):	20
1.3	The Historic of different numerical modelling methods	21
1.3.1	The meshless method:	21
1.3.1.1	Using the meshless method:	21
1.3.2	The finite element method FEM:	22
1.3.3	The extended finite element method XFEM	22

1.1 Composite materials:

1.1.1 Definition:

In this part we are going to give a general definition of the composite material, the word “composite” means “made up of two or more different parts”. In fact, the term composite or composite material is used in a much more restrictive sense. We give for the moment the following general definition. A composite material is made up of the assembly of two materials of different natures, complementing each other and making it possible to end up with a material whose overall performance is superior to that of the components taken separately[25]. Examples of composite materials taken in the broad sense are given in Table 1.1.

1.1.2 general Characteristics:

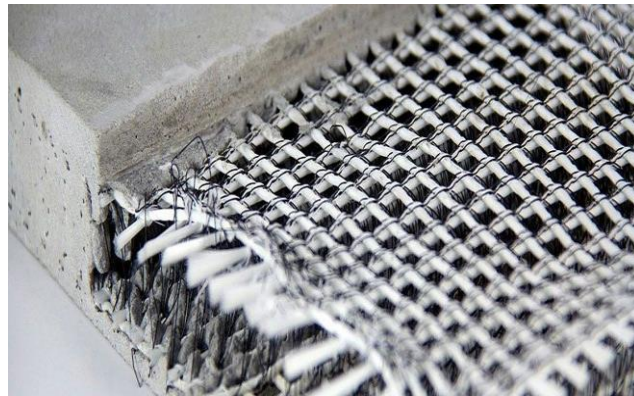
A composite material consists in the most general case of one or more discontinuous phases distributed in a continuous phase. In the case of several discontinuous phases of different natures, the composite is said to be hybrid. The discontinuous phase is usually harder with better mechanical properties than the continuous phase [25]. The continuous phase is called the matrix. The discontinuous phase is called the reinforcement or reinforcing material (fig.1.1). An important exception to the preceding description is the case of polymers modified by elastomers, for which a rigid polymer matrix is loaded with elastomeric particles. For this type of material, the static characteristics of the polymer (Young's modulus, fracture stress, etc.) are practically not modified by the addition of elastomer particles, while the impact characteristics are improved

The properties of composite materials result from:

- The properties of the constituent materials,
- Their geometric distribution,
- Their interactions, etc...

Table 1.1: Examples of composite materials

Composite type	Constituents	Application areas
1. Organic Matrix Composites - Cardboard - Particle boards - Fiber boards - Coated fabrics - Sealing materials - Tires - Laminates - Reinforced plastics	Resin / fillers / fibers cellulosic Resin / wood chips Resin / wood fibers Soft resins / fabrics Elastomers / bitumen / textiles Rubber / canvas / steel Resin / fillers / fibers glass, carbon, etc. Resins / microspheres	Printing, packaging, etc. Carpentry Building Sports, building Roof, terrace, etc. Automotive Multiple domains
2. Ceramic matrix composites - Concrete - Carbon-carbon composite - Ceramic composite	Cement / sand / aggregates Carbon / carbon fibers Ceramic / fibers ceramics	Civil engineering Aviation, space, sports, bio-medicine, etc. Thermal mechanical parts
3. Metal matrix composites	Aluminum / boron fibers Aluminum / carbon fibers	Space

**Fig.1.1:** Composite material

Thus, to access the description of a composite material, it will be necessary to specify:

- The nature of the constituents and their properties,
- The geometry of the reinforcement and its distribution,
- The nature of the matrix-reinforcement interface.

The geometry of the reinforcement will be characterized by: its shape, its size, the concentration of the reinforcement and its arrangement (its orientation), etc. If all of these parameters contribute to determine the properties of the composite, the descriptive models will only take into account certain parameters, due to the complexity of the phenomena involved. For example, the shape of the reinforcement will be roughly approximated either by spheres or by cylinders.

The concentration of the reinforcement is usually measured by the volume fraction (volume fraction) or by the mass fraction (mass fraction). The concentration of the reinforcement is a determining parameter of the properties of the composite material.

For a given concentration, the distribution of the reinforcement in the volume of the composite is also an important parameter. A uniform distribution will ensure “homogeneity” of the material: the properties of the composite will be independent of the measuring point. In the case of a non-uniform distribution of the reinforcement, the rupture of the material will be initiated in the areas of poor reinforcement, thus reducing the strength of the composite.

In the case of composite materials in which the reinforcement consists of fibres, the orientation of the fibers determines the anisotropy of the composite material. This aspect constitutes one of the fundamental characteristics of composites: the possibility of controlling the anisotropy of the finished product by a design and manufacture adapted to the desired properties.

1.1.3 Classification of composite materials:

1.1.3.1 Classification according to the form of the constituents:

According to the shape of the constituents, composites are classified into two main classes: composite materials with particles and composite materials with fibers.

1.1.3.1.1 Fiber composites:

A composite material is a fiber composite if the reinforcement is in the form of fibers. The fibers used are either in the form of continuous fibers or in the form of discontinuous fibers: cut fibers, short fibers, etc. The arrangement of the fibers

and their orientation allow the mechanical properties of composite materials to be modulated as required, to obtain materials ranging from highly anisotropic materials to isotropic materials in a plane[25]. The designer therefore has here a type of material of which he can modify and modulate at will the mechanical and physical behavior by playing on:

- The nature of the constituents,
- The proportion of constituents,
- The orientation of the fibers,

According to the specifications imposed.

The importance of fiber-based composite materials justifies an exhaustive study of their mechanical behavior. As a result, the present work is essentially devoted after that to the study of this type of material.

1.1.3.1.2 Particle composites:

A composite material is a particulate composite when the reinforcement is in the form of particles. A particle, as opposed to fibers, does not have a privileged dimension.

Particles are generally used to improve certain properties of materials or dies, such as stiffness, temperature resistance, abrasion resistance, reduced shrinkage, etc. In many cases, the particles are simply used as fillers to reduce the cost of the material, without diminishing its characteristics.

The choice of the matrix-particle association depends on the desired properties. For example, lead inclusions in copper alloys will increase their ease of machining. Particles of brittle metals such as tungsten, chromium and molybdenum, incorporated in ductile metals, will increase their properties at elevated temperatures, while retaining the ductile character at room temperature [25].

Cermets are also examples of particulate metal-ceramic composites, suitable for high temperature use. For example, oxide based cermet are used for high speed cutting tools, and for high temperature protections.

In addition, elastomer particles can be incorporated into fragile polymer matrices, so as to improve their properties at break and impact, by reducing the susceptibility to cracking.

1.1.3.2 Classification according to the nature of the constituents:

Depending on the nature of the matrix, the composite materials are classified according to composites with an organic matrix, a metal matrix or a mineral matrix. Various reinforcements are associated with these matrices. Only certain pairs of associations currently have industrial use, others are being developed in research laboratories [25]. Among these composites are:

- a. Composites with an organic matrix (resin, fillers), with:
 - Mineral fibers: glass, carbon, etc.
 - Organic fibers: Kevlar, polyamides, etc.
 - Metal fibers: boron, aluminum, etc.
- b. Metal matrix composites (light and ultralight aluminum alloys, magnesium, titanium), with:
 - Mineral fibers: carbon, silicon carbide (SiC),
 - Metal fibers: boron,
 - Metallo-mineral fibers: boron fibers coated with carbon silicon (BorSiC).
- c. Composites with mineral matrix (ceramic), with:
 - Metal fibers: boron,
 - Metallic particles: cermets,
 - Mineral particles: carbides, nitrides, etc.

Composite materials with an organic matrix can only be used in the range of temperatures not exceeding 200 to 300 °C, whereas composite materials with metallic or mineral matrices are used above: up to 600 °C for a matrix metallic, up to 1000 °C for a ceramic matrix.

1.1.4 Volume fraction and mass fraction:

1.1.4.1 Introduction:

One of the most important factors that determine the mechanical characteristics of a composite material is the relative proportion of matrix and reinforcement. This proportion can be expressed either as a volume fraction or as a mass fraction. Mass fractions are easier to measure when developing materials. On the other hand, volume fractions intervene directly in the theoretical models describing the mechanical behavior of materials [25]. It is therefore necessary to know how to switch from one of these fractions to the other. These expressions will be established for a material with two phases, and then extended to a material with more than two phases.

1.1.4.2 Volume fraction:

Consider a volume V_c of composite material, composed of a volume V_f of fibers and a volume V_m of matrix. Subsequently, the indices c , f and m will be systematically used as respective indices of the characteristics of the composite material, of the fibers and of the matrix. The volume fraction of fibers is:

$$V_f = \frac{v_f}{v_c} \quad (1.1)$$

The volume fraction of the matrix is:

$$V_m = \frac{v_m}{v_c} \quad (1.2)$$

With

$$V_m = 1 - V_f \quad (1.3)$$

Since

$$v_c = v_f + v_m \quad (1.4)$$

1.1.4.3 Surface fraction:

For example an elliptical inclusion with greater radius a and lower radius b , the area fraction is given by $f' = a/w$, since the thickness is taken unitary with w is taken half the width of the composite.

1.1.4.4 Mass fraction:

In the same way as the volume fractions, the mass fraction of the fiber is written as a function of the mass of the composite m_c , the mass of the fiber m_f is the mass of the matrix m_m as follows [2]:

$$M_f = \frac{m_f}{m_c} \quad (1.5)$$

The mass fraction of the matrix is:

$$M_m = \frac{m_m}{m_c} \quad (1.6)$$

Giving:

$$M_m = 1 - M_f \quad (1.7)$$

1.1.5 The presence of porosity:

The presence of porosities in a composite can lead to a significant reduction in its mechanical characteristics, by increasing the dispersion of its values. The presence of porosities also increases the sensitivity of the composite material to the external environment: increase in moisture absorption, decrease in resistance to chemicals, etc [25]. It is therefore important to have an estimate of the proportion of porosities, in order to assess the quality of a composite. A quality composite material contains less than 1% by volume porosity, while a poor quality composite may reach 5%.

1.1.6 Nano-materials:

A nanomaterial is a natural material, accidentally formed or manufactured, containing free particles, in an aggregate or agglomerate form, of which at least 50% of the particles, in the numerical distribution by size, have one or more external dimensions, between 1 nm and 100 nm [26].

According to the ISO TS 80004-1 standard, a nanomaterial is a material in which at least one external dimension is at the nano-metric scale, that is to say between approximately 1 and 100 nm or which has an internal or surface structure at the nano-scale.

There are two main families of nano-materials:

a. Nano-objects:

Which are materials of which one, two or three external dimensions are located at the nano-metric scale, which means approximately between 1 and 100 nm, among the nano-objects, it is possible to distinguish three categories:

- Nanoparticles
- Nanofibers, nanotubes, nano-filaments or nano-drams.
- Nano-sheets, nano-plates or nano-plates.

b. Nano-structured materials:

It has an internal or surface structure at the nanometric scale. Among the nanostructured materials, it is possible to distinguish several families among which:

- **Aggregates and agglomerates of nano-objects:** Nano-objects can be in individual form (that is, in the form of primary particles) or in the form of aggregates or agglomerates which their size is substantially greater than 100 nm.
- **Nano-composites:** These materials are composed of all or part of nano-objects which give them improved or specific properties of the nano-metric dimension. Nano-objects are incorporated in a matrix or on a surface in order to provide new functionality or to modify certain mechanical, magnetic, thermal properties, etc. Polymers loaded with carbon nanotubes used in the sports equipment sector to improve their mechanical strength and reduce their weight are an example of nanocomposites.
- **Nano-porous materials:** These materials have nano-metric sized pores. Silica aerogels are nano-porous materials that exhibit excellent thermal insulation properties.

1.2 History and theory of fracture mechanics:

1.2.1 Development and history of fracture mechanics:

Fracture mechanics were initiated by Griffith [27] around 1920. The objective of fracture mechanics is to characterize the cracking behavior of structures using parameters that can be quantified in the engineer's sense, in particular the stress field, the size of the crack and the resistance to cracking of the material. The first theoretical developments in the analysis of displacement, strain and stress fields in the vicinity of a crack were undertaken by Westergaard around 1940, a failure theory based on the stability of the crack valid only for brittle materials, not taking into account the energy dissipation due to plasticization. In 1948 Irwin proposed a modification of Griffith's theory by precisely including the energy due to plasticization in the energy balance, so that Griffith's approach was applicable to ductile materials.

In 1956, a group of US Navy researchers extended the concept of the rate of energy release from Griffith's theory into a form that could be easily used by structural designers. In 1957, based on the work of Westergaard [28], Irwin [29] showed that the displacements and the stresses in the vicinity of the end of a crack can be described using a single parameter related to the energy release rate. This parameter characterizes the state of stress in the region in which the failure occurs; it is called the Stress Intensity Factor (SIF).

The period from 1960 to 1980 saw an intensification of research on the fracture with two competing schools. On the one hand, the proponents of the approach using linear fracture mechanics and on the other hand those who were mainly interested in the plasticization that develops at the end of a crack. To take into account the effect of this plasticization on the stress and displacement fields at the end of a crack, several authors such as Barenblatt [30] gave what is called a plastic zone correction. The size of the crack is then increased by this plastic zone to

find the elastic stress fields described by the SIF. Later, Hutchinson in 1968, Rice and Rosengren (HRR) [31] developed a new parameter called J-integral. This parameter perfectly describes the distribution of stresses in plasticized zones (HRR field).

1.2.2 Generalities on fractures by cracking:

Cracking is a defect that affects materials and degrades its mechanical strength. Cracks are initially small in size (microscopic cracks) that can come together to lead to the appearance of a dangerous incision. Most cracks are due to physical phenomena (shrinkage, expansion).

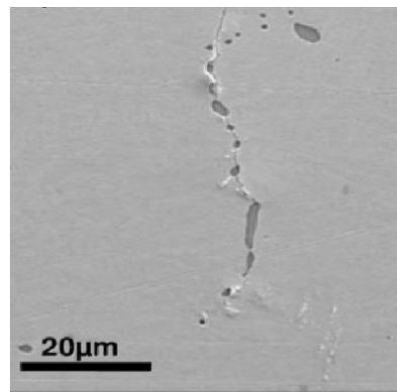


Fig.1.2: Macroscopic crack

Cracking is the result of local damage, by repeated mechanical stress, or a maximum stress exceeding the allowable stress (greater than the possibilities) of the material. Permanent plastic deformations are created at the microscopic level.

There are several types of cracks:

- Detachment cracks between different types of materials (for example between a fibre and matrix or in the vicinity of an empty hole in the materials).
- Fracture cracks which may be through (or partial) and which correspond to excessive stress (tensile or shear stress greater than the "possibilities" of the material).

1.2.3 The three modes of a fracture of a crack:

If someone finds a crack in a plan, he will recognize it according to the direction of stress three modes of displacement of the lips of the crack. The modes indicated on the figure 1.3 correspond to various kinematics of displacement to the lips of the crack:

1.2.3.1 Mode I or opening mode (tensile test):

The loading or the applied force is perpendicular both to the plan of the crack and to the line at the end of the crack. The field of displacement and stress in the vicinity of a crack is defined by:

- **Stress field in mode I:**

$$\sigma_{xx} = \frac{KI}{\sqrt{2\pi r}} \cos\left(\frac{\theta}{2}\right) \left[1 - \sin\left(\frac{\theta}{2}\right) \sin\left(\frac{3\theta}{2}\right)\right]$$

$$\sigma_{yy} = \frac{KI}{\sqrt{2\pi r}} \cos\left(\frac{\theta}{2}\right) \left[1 - \sin\left(\frac{\theta}{2}\right) \sin\left(\frac{3\theta}{2}\right)\right]$$

$$\sigma_{xy} = \frac{KI}{\sqrt{2\pi r}} \cos\left(\frac{\theta}{2}\right) \sin\left(\frac{\theta}{2}\right) \cos\left(\frac{3\theta}{2}\right)$$

$$\sigma_{zz} = \nu (\sigma_{xx} + \sigma_{yy}) \text{ in plan strain}$$

$$\sigma_{zz} = 0 \text{ in plan stress}$$

$$\sigma_{xz} \text{ and } \sigma_{yz} = 0$$

- **Displacement field in mode I:**

$$u_x = \frac{KI}{2\mu} \sqrt{\frac{r}{2\pi}} \cos\left(\frac{\theta}{2}\right) \left[\kappa - 1 + 2 \sin^2\left(\frac{\theta}{2}\right)\right]$$

$$u_y = \frac{KI}{2\mu} \sqrt{\frac{r}{2\pi}} \sin\left(\frac{\theta}{2}\right) \left[\kappa + 1 - 2 \cos^2\left(\frac{\theta}{2}\right)\right]$$

$$\kappa = 3 - 4\nu \text{ in plan strain}$$

$$\kappa = \frac{3-\nu}{1+\nu} \text{ in plan stress}$$

1.2.3.2 Mode II or plan sliding mode (shear test):

The loading is parallel with the plane of the crack and perpendicular to the line of the end of the crack. The field of displacement and stress in the vicinity of crack is defined by:

- **Stress field in mode II:**

$$\sigma_{xx} = \frac{K_{II}}{\sqrt{2\pi r}} \sin\left(\frac{\theta}{2}\right) \left[2 + \cos\left(\frac{\theta}{2}\right) \cos\left(\frac{3\theta}{2}\right)\right]$$

$$\sigma_{yy} = \frac{K_{II}}{\sqrt{2\pi r}} \sin\left(\frac{\theta}{2}\right) \cos\left(\frac{\theta}{2}\right) \cos\left(\frac{3\theta}{2}\right)$$

$$\sigma_{xy} = \frac{K_{II}}{\sqrt{2\pi r}} \cos\left(\frac{\theta}{2}\right) \left[1 - \sin\left(\frac{\theta}{2}\right) \sin\left(\frac{3\theta}{2}\right)\right]$$

$$\sigma_{zz} = \nu (\sigma_{xx} + \sigma_{yy}) \text{ in plane strain}$$

$$\sigma_{zz} = 0 \text{ in plane stress}$$

$$\sigma_{xz} \text{ et } \sigma_{yz} = 0$$

- **Displacement field in mode II:**

$$u_x = \frac{K_{II}}{2\mu} \sqrt{\frac{r}{2\pi}} \sin\left(\frac{\theta}{2}\right) \left[\kappa + 1 + 2 \cos^2\left(\frac{\theta}{2}\right)\right]$$

$$u_y = \frac{K_{II}}{2\mu} \sqrt{\frac{r}{2\pi}} \cos\left(\frac{\theta}{2}\right) \left[\kappa - 1 - 2 \sin^2\left(\frac{\theta}{2}\right)\right]$$

$$\kappa = 3 - 4\nu \text{ in plane strain}$$

$$\kappa = \frac{3-\nu}{1+\nu} \text{ in plane stress}$$

1.2.3.3 Mode III or anti-plan sliding mode (torsion test):

The loading is parallel with the plane of the crack and parallel to the line of the end of the crack. The field of displacement in the vicinity of crack is defined by:

- **Stress field and Displacement field in mode III:**

$$\sigma_{xz} = \frac{K_{III}}{\sqrt{2\pi r}} \sin\left(-\frac{\theta}{2}\right)$$

$$\sigma_{yz} = \frac{K_{III}}{\sqrt{2\pi r}} \cos\left(\frac{\theta}{2}\right)$$

$$U_z = 2 \frac{K_{III}}{\mu} \sqrt{\frac{r}{2\pi}} \sin\left(\frac{\theta}{2}\right)$$

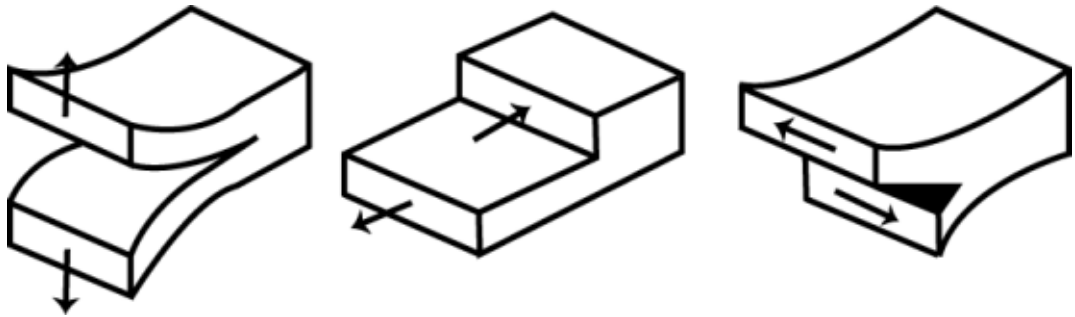


Fig.1.3: The three modes of a fracture of a crack

1.3 The Historic of different numerical modelling methods:

1.3.1 The meshless method:

This method was invented in 1977 to review the phenomena of astrophysics such as the explosion of stars. Subsequently, several research works were interested in the developments of this method led to the emergence of new variants.

The literary definition of the non-mesh method is: "a method which does not use any mesh for solving a physical problem or is a method based on the building of the shape function not dependent on any mesh".

Another definition proposed by N. Calvo et al. [32] which joins the first proposition in a more concise way: "A method without mesh is a method where the function of form employed depends on the positions of the nodes only." Through these two definitions we can notice that the key step in these methods is that of the construction of the shape function. The latter should not depend on any mesh; however it leaves the possibility of using a mesh in the rest of the solving process.

1.3.1.1 Using the meshless method:

The meshless method is useful in the following cases:

Mesh degeneration during simulation (the re-meshing operation can introduce errors).

In the case of deformable boundaries (multiphase flows ...) or large deformations (plastic materials, etc.), where it is very difficult to maintain the connectivity of the mesh without introducing errors during the simulation [33]:

- Complex 3D geometries: Difficult mesh requiring human assistance.
- Creation or destruction of nodes (simulation of crack propagation).
- Problematic geometry misalignment for a fixed mesh in bending simulations...
- Nonlinearities, discontinuities or singularities.

1.3.2 The meshing methods:

1.3.2.1 The finite element method FEM:

The origin of this mathematical method was discovered by the mathematician COURANT in 1943 based on the variational method of Rayleigh (1870) and Ritz (1909) which was discovered in the 1940s. This led them to try to combine with continuous structures, by making an approximation on small portions in a continuous problem of a long bar, hence the basic idea of finite elements.

Argyris (1955), Turner (1956), Glough (1956) and Martin (1956) made a direct analogy by adopting a simplified behavior for small portions: they represent an elastic continuous medium in two dimensions by an assembly of triangular panels, on which displacements are supposed to be linearly varied as for each bar or beam of the discrete system [34]: each panel is described by a stiffness matrix and the assembly gave the total rigidity of the continuous medium, from where the birth of finite elements.

1.3.2.2 The extended finite element method XFEM:

Historic:

In 1997, Babuška and Melenk introduced a method to have the functions describing the singularity while respecting the boundary conditions. Their principle is to introduce as a form function functions capable of taking into account the singularity that one wants to treat (known by different approaches) and to regularize them on the edge thanks to a function (which preserves the properties of the functions introduced on the inside of the domain). They have shown that with this method, the normal convergence rate can be found.

This new method is an original idea of Belytschko and Black [35]; the authors presented a method for the enrichment of finite elements so that the crack growth problems can be solved with a minimal meshing.

Möes et al. [36] completely eliminated the meshing operations by adding a discontinuous function in the enrichment base. Sukumar et al. [37] presented the implementation of X-FEM in 3D crack modelling. They demonstrated the accuracy of this technique for three-dimensional stationary cracks, a discontinuous function was used to model the inner surface of the crack, and asymptotic functions derived from the two-dimensional displacement field for the enrichment of the crack boundaries.

Jack Chessa and Ted Belytschko [38] generalized the method for the representation of the arbitrary discontinuity. Stolarska et al. [39] used X-FEM in conjunction with the method level set to treat the crack propagation in two dimensions. Belytschko et al. [40] presented a simplified method based on implicit functions to describe discontinuities between materials, surface slippage and cracks.

In the extended finite element method, firstly, the usual finite element mesh is produced. Then, by considering the location of the discontinuities, some degrees of freedom are added to the classical finite element model in selected nodes close to the discontinuities to provide a higher level of precision with the consideration of a discontinuity within an element.

The advantages of this method are:

- A least meshing.
- Introduction of singular fields.
- Intrinsic positioning of the crack.

CHAPTER 2

Generalities on Homogenization

CHAPTER 2

Generalities on Homogenization

In the calculation of structures, materials are often assumed to be homogeneous or at least homogeneous by area. In reality, the materials are always heterogeneous on a smaller scale, more or less small depending on the materials. When we go down to this so-called microscopic scale, we generally notice that the material consists of different zones that can be considered to be homogeneous. The homogenization philosophy consists in replacing a non-homogeneous real material by a homogeneous fictitious material with equivalent macroscopic properties. The homogenization procedures can be applied to determine a wide range of physical properties which can be mechanical, electrical, acoustic, thermal, and others. For a possible homogenization, it is necessary to be able to define a representative elementary volume (R.E.V) of the material. The result of the homogenization will be the behavior of the equivalent homogeneous material. In this chapter, we will present the homogenization technique used in linear elasticity.

SUMMARY

2.1	State of the art	25
2.2	Behaviour law	25
2.3	Concept of homogenization	27
2.3.1	Representative Elementary Volume (REV)	27
2.3.2	Homogenization and boundary conditions	28
2.4	Homogenization based on the analytical approach	29
2.4.1	Mean field theory	29
2.4.1.4	Reuss Model	31
2.4.1.5	Voigt Model	31
2.4.2	Homogenization based on the numerical approach	31
2.4.2.1	Homogenization configurations	31
2.4.2.2	Boundary conditions applied to REV	33
2.4.3	Direct simulation of the microstructure	34
2.5	Homogenization flowchart	38
2.6	Conclusion	39

2.1 State of the art:

Most multiscale approaches are based on the principle of homogenization. The first works consisted in setting up spatial homogenization methods based on analytical or semi-analytical studies at the microscopic scale thus leading to the identification of a macroscopic behavior between “effective” average quantities Eshelby 1957, Hashin 1962, Hill 1965, Mori and Tanaka 1973. However, the latter do not allow strengthening to local properties. The taking into account of increasingly complex mechanisms at the microscopic level has given rise to methods called "Unit Cell Methods" Christman et al. 1989, Tvergaard 1990, Sluis et al. 1999. They make it possible to identify a macroscopic model by "numerical tests" on a representative elementary volume (REV) of the structure and to obtain local information on the solution. Unfortunately, the a priori definition of a macroscopic model remains penalizing when it comes to dealing with problems where large gradients of deformations occur (near edges, holes, cracks) and more usually when it comes to handle non-linear problems. Moreover, these “phenomenological” approaches are not necessarily multi-scale approaches.

2.2 Behaviour law:

In the context of small disturbances, the systems studied in this thesis are considered to have a linear elastic response to mechanical stresses. The behavioral relations are expressed for each of the phases within the framework of linear elasticity using generalized Hooke's law:

$$\boldsymbol{\sigma} = \mathbf{C} : \boldsymbol{\varepsilon} \quad (2.1)$$

Where \mathbf{C} , tensor of order 4, is called tensor of elastic moduli or tensor of elastic rigidities, it allows expressing the stress tensor as a function of the strain tensor. Furthermore, it is possible to express the strain tensor as a function of the stress tensor via the flexibility tensor or flexibilities tensor \mathbf{S} , the inverse of the stiffness matrix:

$$\boldsymbol{\varepsilon} = \mathbf{S} : \boldsymbol{\sigma} \quad (2.2)$$

With $\mathbf{S} = \mathbf{C}^{-1}$

Using symmetry, the 81 components of C_{ijkl} and S_{ijkl} are reduced to 21 components. These 21 components can then be represented in the form of a C_{ij} and S_{ij} matrix with 21 independent components as follows:

The stiffness tensor can be written in the following matrix form:

$$\begin{Bmatrix} \sigma_{11} \\ \sigma_{22} \\ \sigma_{33} \\ \sigma_{23} \\ \sigma_{31} \\ \sigma_{12} \end{Bmatrix} = \begin{bmatrix} c_{11} & c_{12} & c_{13} & c_{14} & c_{15} & c_{16} \\ c_{12} & c_{22} & c_{23} & c_{24} & c_{25} & c_{26} \\ c_{13} & c_{23} & c_{33} & c_{34} & c_{35} & c_{36} \\ c_{14} & c_{24} & c_{34} & c_{44} & c_{45} & c_{46} \\ c_{15} & c_{25} & c_{35} & c_{45} & c_{55} & c_{56} \\ c_{16} & c_{26} & c_{36} & c_{46} & c_{56} & c_{66} \end{bmatrix} \begin{Bmatrix} \varepsilon_{11} \\ \varepsilon_{22} \\ \varepsilon_{33} \\ 2\varepsilon_{23} \\ 2\varepsilon_{31} \\ 2\varepsilon_{12} \end{Bmatrix} \quad (2.3)$$

The flexibility matrix is obtained by inverting (2.3). We then obtain:

$$\begin{Bmatrix} \varepsilon_{11} \\ \varepsilon_{22} \\ \varepsilon_{33} \\ 2\varepsilon_{23} \\ 2\varepsilon_{31} \\ 2\varepsilon_{12} \end{Bmatrix} = \begin{bmatrix} s_{11} & s_{12} & s_{13} & s_{14} & s_{15} & s_{16} \\ s_{12} & s_{22} & s_{23} & s_{24} & s_{25} & s_{26} \\ s_{13} & s_{23} & s_{33} & s_{34} & s_{35} & s_{36} \\ s_{14} & s_{24} & s_{34} & s_{44} & s_{45} & s_{46} \\ s_{15} & s_{25} & s_{35} & s_{45} & s_{55} & s_{56} \\ s_{16} & s_{26} & s_{36} & s_{46} & s_{56} & s_{66} \end{bmatrix} \begin{Bmatrix} \sigma_{11} \\ \sigma_{22} \\ \sigma_{33} \\ \sigma_{23} \\ \sigma_{31} \\ \sigma_{12} \end{Bmatrix} \quad (2.4)$$

In the particular case of an isotropic material, the stiffness matrix is:

$$\begin{Bmatrix} \sigma_{11} \\ \sigma_{22} \\ \sigma_{33} \\ \sigma_{23} \\ \sigma_{31} \\ \sigma_{12} \end{Bmatrix} = \begin{bmatrix} c_{11} & c_{12} & c_{12} & 0 & 0 & 0 \\ c_{12} & c_{11} & c_{12} & 0 & 0 & 0 \\ c_{12} & c_{12} & c_{11} & 0 & 0 & 0 \\ 0 & 0 & 0 & \frac{1}{2}(c_{11} - c_{12}) & 0 & 0 \\ 0 & 0 & 0 & 0 & \frac{1}{2}(c_{11} - c_{12}) & 0 \\ 0 & 0 & 0 & 0 & 0 & \frac{1}{2}(c_{11} - c_{12}) \end{bmatrix} \begin{Bmatrix} \varepsilon_{11} \\ \varepsilon_{22} \\ \varepsilon_{33} \\ 2\varepsilon_{23} \\ 2\varepsilon_{31} \\ 2\varepsilon_{12} \end{Bmatrix} \quad (2.5)$$

Generally, the stiffness constants are expressed by introducing the Lamé coefficients λ and μ , from where : $C_{11} = \lambda + 2\mu$; $C_{12} = \lambda$; $\frac{1}{2}(C_{11} - C_{12}) = \mu$

In the same way for the matrix of flexibility, but with $S = C^{-1}$

2.3 Concept of homogenization:

The main purpose of the homogenization concept is to determine the macroscopic behaviour from the elementary behaviours of the different phases, constituting the studied material, in order to replace the heterogeneous real material with an equivalent effective homogeneous material. Once subjected to the same loadings, this material is supposed to behave in the same way as the actual material.

This behaviour is determined on a volume element of dimension, sufficiently small compared to the dimensions of the considered structure. This volume element is called the Representative Elementary Volume (REV) of the material as shown in Figure 1.

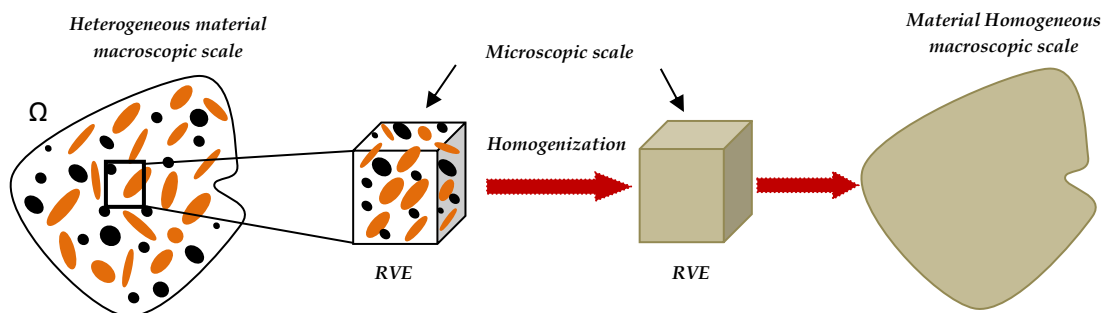


Fig.2.1: The principle of homogenization

2.3.1 Representative Elementary Volume (REV) ;

A REV for a "material point" of a given mass at the macroscopic scale is a volume of matter which is representative on the microscopic scale of the internal constitution of the material as will be presented in figure (2.2).

The REV must meet several conditions:

- Be large enough in relation to the size of the heterogeneities to be representative of the material and to be statistically equivalent from one zone to another;
- Be small enough in relation to the dimensions of the structure under consideration so that it can be considered to be under uniform stress or subjected to uniform deformation.

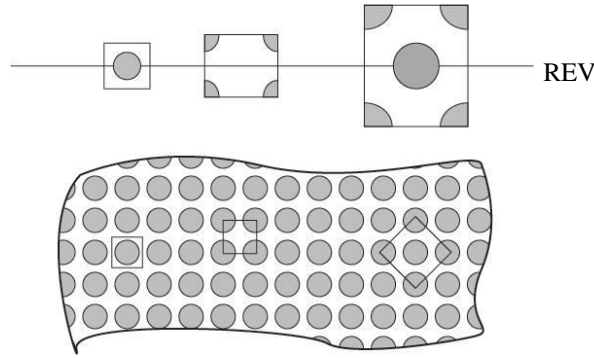


Fig.2.2: Choice of REV

2.3.2 Homogenization and boundary conditions:

Homogenization in solid mechanics consists in evaluating the effective behavior of the composite based on a calculation carried out on a Representative Elementary Volume (REV), on which predefined Boundary Conditions (BCs) are applied. The apparent behavior resulting from the REV calculation shall not depend on the prescribed boundary conditions, nor the statistical realization. This will be the case when the REV is sufficiently large. Hence, we are aware that the REV we adopted in the present study is not very large and consequently there could be an effect of the boundary conditions and the statistical realizations, on the computed values of the effective properties. Nevertheless, in the performed numerical simulations, it has been checked by the authors that the effect of BCs and/or REV size is quantitatively limited and not significant for the conducted parametric studies.

Regarding the boundary conditions prescribed on the REV, there are three types of boundary conditions, viz. SUBC (static uniform boundary condition), KUBC (kinetic uniform boundary condition) and PBC (periodic boundary condition) that can possibly be adopted. All these BCs verify the Hill-Mandel condition [41-42], and in that respect, are expressed as function of the macroscopic/average strain or stress. Hence, in the present work where the KUBC and PBC boundary conditions were adopted, the prescribed displacements BCs on the REV are function of the macroscopic strain. The effective properties can then be deduced by imposing particular values on the macroscopic strain. As more explained below, a judicious choice is for example, to set $\epsilon_{11} = 1$ and the other macro

strain components equal to zero. We then have access to the first column of the stiffness tensor by simply averaging over the stress field components calculated.

2.4 Homogenization based on the analytical approach:

Analytical approaches to homogenization theory can be divided into two main families: mean field theory and the asymptotic approach. In this chapter we are only interested in mean field theory.

2.4.1 Mean field theory:

2.4.1.1 Volume average of a stress and strain field in equilibrium on the REV:

A REV of volume V in equilibrium is subjected to stresses on the boundary ∂V , these forces being assumed in equilibrium without volume forces.

It is considered that the volume average of the stress field defined by:

$$\bar{\sigma} = \frac{1}{V} \int_V \sigma \, dV \quad (2.6)$$

And the volume average of strain field defined by:

$$\bar{\varepsilon} = \frac{1}{V} \int_V \varepsilon \, dV \quad (2.7)$$

2.4.1.2 Boundary conditions in homogeneous stresses and strains:

Subsequently, the solution of the problem of homogenization of the heterogeneous medium will be obtained either from the condition in displacement imposed on the boundary compatible with a uniform strain on the edge of the field, or from an imposed stress vector condition on the border compatible with a uniform stress field.

- Stress approach:

For the case where the stress vector is imposed on the contour ∂V compatible with the uniform stress tensor Σ , we obtain:

$$\mathbf{T} = \sigma \cdot \mathbf{n} \quad \text{Sur } \partial V \quad (2.8)$$

The relation between the volume average of the stress field and the constant stress σ is given by:

$$\bar{\sigma} = \frac{1}{V} \int_V \sigma \, dV = \sigma \quad (2.9)$$

- **Strain approach:**

A field of linear displacement and function of the constant strain ε is imposed on the border ∂V :

$$u(x) = \varepsilon \cdot x \quad (2.10)$$

Where ε is uniform

The relation between the volume average of the strain field and the constant strain ε is given by:

$$\bar{\varepsilon} = \frac{1}{V} \int_V \varepsilon dV = \varepsilon \quad (2.11)$$

2.4.1.3 Periodic boundary condition at contour:

The periodic boundary conditions on the contour of the REV and for this type of boundary conditions, one can also distinguish an approach in stresses and an approach in d deformations.

• **stress approach:**

The stress field at the point x of base cell V is considered to be of the form:

$$\bar{\sigma}(x) = \sigma + \sigma^{per}(x) \quad (2.12)$$

Where $\sigma^{per}(x)$ is a periodic stress field.

It is notable that such a stress field is in equilibrium on the edge of the domain, because the periodicity of the stress tensor implies the anti-periodicity of the stress vector on the edge of the domain. Moreover, its volume average can be fixed at the value as in the case of fixed boundary conditions.

• **strain approach:**

The field of displacement at the point x of the basic cell V is determined in a similar way by the relationship:

$$u(x) = \varepsilon x + u^{per}(x) \quad (2.13)$$

Where $u^{per}(x)$ is a periodic displacement field

Then, the strain field at point (x) of the base cell V is given by:

$$\bar{\varepsilon}(x) = \varepsilon + \varepsilon^{per}(x) \quad (2.14)$$

2.4.1.4 Reuss Model:

The Reuss model (also called rule of mixtures) assumes that the strain tensors in the fiber, matrix, and composite are the same $\boldsymbol{\varepsilon} = \boldsymbol{\varepsilon}^f = \boldsymbol{\varepsilon}^m$ [25]; so, the strain concentration tensors are all equal to the identity matrix $\boldsymbol{\varepsilon}_i = I$.

2.4.1.5 Voigt Model:

The Voigt model (also called inverse rule of mixtures) assumes that the stress tensors in the fiber, matrix, and composite are the same $\boldsymbol{\sigma} = \boldsymbol{\sigma}^f = \boldsymbol{\sigma}^m$; so, the stress concentration tensors are all equal to the identity matrix $\boldsymbol{\sigma}_i = I$ [25].

2.4.2 Homogenization based on the numerical approach:

As the analytical application of homogenization theory is very complex for cases other than simple cases, research has focused on its coupling with numerical methods.

2.4.2.1 Homogenization configurations:

The case of a nano-composite with cylindrical regular arranged fibers is considered in this study. The REV can be a parallelepipedic domain with only a central fiber as shown in figure 2.3a. This configuration (with $\mathbf{a}_1 = \mathbf{a}_2 = \mathbf{a}_3$) was adopted in 2D works in order to predict numerically, [6], and analytically, [43-44], the effective elastic behavior of an aluminum nano-composite. In these two studies, it was assumed that the REV possesses transverse isotropy in the plane orthogonal to the axis of the cylindrical heterogeneity, [43-44]. In fact, the transverse isotropy is ensured only for hexagonal arrangement (Fig. 2.3b, ($\mathbf{a}_1 = \mathbf{a}_2 = \mathbf{a}_3 / \tan(\frac{\pi}{3})$)) [25] of the cylindrical fiber expressed by equation (2.15), otherwise the symmetry is tetragonal.

$$\mathbf{C}_{\text{eff}} = \begin{bmatrix} C_{11} & C_{12} & C_{12} & 0 & 0 & 0 \\ C_{12} & C_{22} & C_{23} & 0 & 0 & 0 \\ C_{12} & C_{23} & C_{22} & 0 & 0 & 0 \\ 0 & 0 & 0 & \frac{1}{2}(C_{22} - C_{23}) & 0 & 0 \\ 0 & 0 & 0 & 0 & C_{66} & 0 \\ 0 & 0 & 0 & 0 & 0 & C_{66} \end{bmatrix} \quad (2.15)$$

Nevertheless, the results obtained in Example 5.2 in chapter 5 with square arrangement (Fig. 2.3a) do not show significant changes on C_{eff} compared to the hexagonal arrangement (Fig. 2.3b), justifying thus the simplifying considerations adopted here and in [6-44].

The engineering elasticity constants in the case of transverse isotropy are given by [3]:

$$\left. \begin{aligned} E_1 &= C_{11} - 2C_{12}^2/(C_{22} - C_{23}), v_{12} = v_{13} = C_{12}/(C_{22} + C_{23}) \\ E_2 = E_3 &= [C_{11}(C_{22} + C_{23}) - 2C_{12}^2]/(C_{11}C_{22} - C_{12}^2) \\ v_{23} &= [C_{11}C_{23} - C_{12}^2]/(C_{11}C_{22} - C_{12}^2), G_{12} = G_{13} = C_{66}, G_{23} = C_{44} = \frac{1}{2}(C_{22} - C_{23}) = E_1 \frac{E_2}{2(1-\nu_{23})} \end{aligned} \right\} \quad (2.16)$$

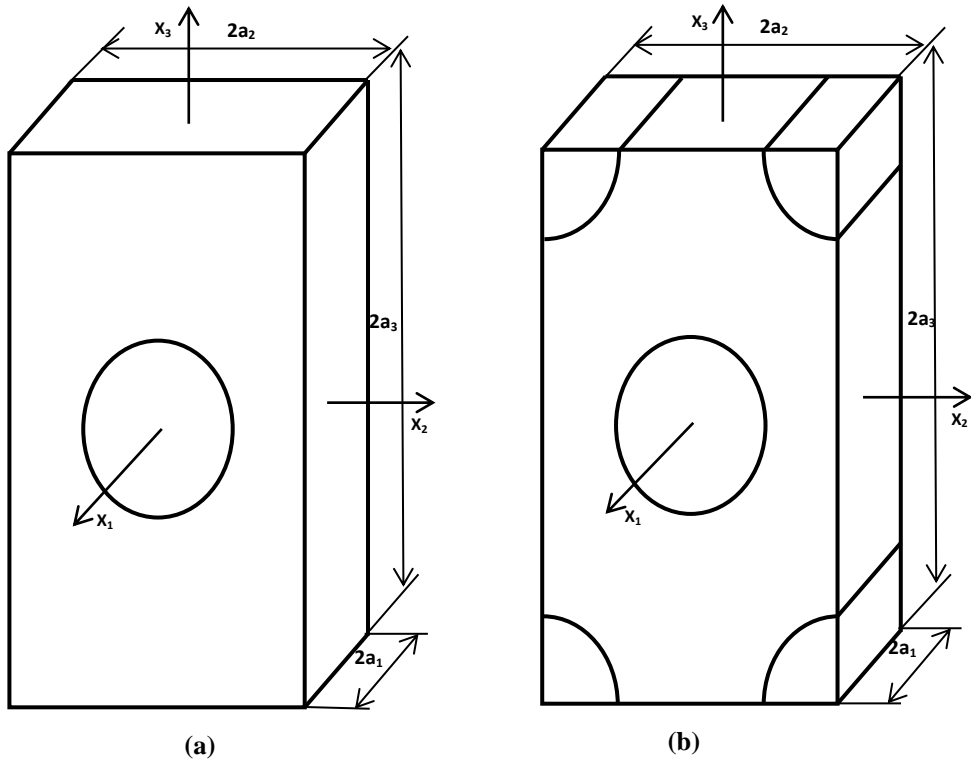


Fig.2.3: REV's Configurations: **a)** Square arrangement, **b)** Hexagonal arrangement

In the following the procedure to evaluate C_{eff} will be explained. The matrix C_{eff} links between the average strain $\bar{\epsilon}$ and stress $\bar{\sigma}$:

$$\bar{\sigma} = C_{eff} \bar{\epsilon} \quad (2.17)$$

Imposing BCs that verify the Hill-Mandel condition, enables to express the prescribed BCs here of displacement type as a function of the imposed average strain ϵ^0 .

The effective properties can then be deduced by imposing particular values on the macroscopic strain. A judicious choice is for example:

$$\epsilon^0 = [\epsilon_{11}^0 = 1 \quad \epsilon_{22}^0 = 0 \quad \epsilon_{33}^0 = 0 \quad 2\epsilon_{12}^0 = 0 \quad 2\epsilon_{23}^0 = 0 \quad 2\epsilon_{13}^0 = 0]^T \quad (2.18)$$

We then have access to the first column of the stiffness tensor by simply averaging the stress field over the REV $\bar{\sigma} = \frac{1}{V} \int_V \sigma \cdot dV$, according to:

$$\bar{\sigma} = C_{eff} \epsilon^0 \quad (2.19)$$

2.4.2.2 Boundary conditions applied to REV:

- a. **For periodic boundary conditions (PBC)**, the boundary conditions prescribed on the REV's boundaries of Figure 2.3 are:

$$u(x + L/2) = u(x - L/2) + \epsilon^0 \cdot L, \forall x \in \partial\Omega_{RVE} \quad (2.20)$$

Where L refers to the periodicity vector, defined here as $[2a_1 \ 2a_2 \ 2a_3]^T$.

which yield to, [3]:

$$\begin{aligned} u_i(a_1, x_2, x_3) - u_i(-a_1, x_2, x_3) &= 2a_1 \epsilon_{i1}^0 ; \quad \begin{cases} -a_2 \leq x_2 \leq a_2 \\ -a_3 \leq x_3 \leq a_3 \end{cases} \\ u_i(x_1, a_2, x_3) - u_i(x_1, -a_2, x_3) &= 2a_2 \epsilon_{i2}^0 ; \quad \begin{cases} -a_1 \leq x_1 \leq a_1 \\ -a_3 \leq x_3 \leq a_3 \end{cases} \\ u_i(x_1, x_2, a_3) - u_i(x_1, x_2, -a_3) &= 2a_3 \epsilon_{i3}^0 ; \quad \begin{cases} -a_1 \leq x_1 \leq a_1 \\ -a_2 \leq x_2 \leq a_2 \end{cases} \end{aligned} \quad (2.21)$$

- b. **For kinetic uniform strain boundary conditions (KUBC)**, the boundary conditions prescribed on the REV's boundaries of Figure 4 are:

$$u(x) = \epsilon^0 \cdot x, \forall x \in \partial\Omega_{RVE} \quad (2.22)$$

which yield to, [3]:

$$\begin{aligned} u_i(\pm a_1, x_2, x_3) &= \pm a_1 \epsilon_{i1}^0 + x_2 \epsilon_{i2}^0 + x_3 \epsilon_{i3}^0 ; \quad \begin{cases} -a_2 \leq x_2 \leq a_2 \\ -a_3 \leq x_3 \leq a_3 \end{cases} \\ u_i(x_1, \pm a_2, x_3) &= x_1 \epsilon_{i1}^0 \pm a_2 \epsilon_{i2}^0 + x_3 \epsilon_{i3}^0 ; \quad \begin{cases} -a_1 \leq x_1 \leq a_1 \\ -a_3 \leq x_3 \leq a_3 \end{cases} \\ u_i(x_1, x_2, \pm a_3) &= x_1 \epsilon_{i1}^0 + x_2 \epsilon_{i2}^0 \pm a_3 \epsilon_{i3}^0 ; \quad \begin{cases} -a_1 \leq x_1 \leq a_1 \\ -a_2 \leq x_2 \leq a_2 \end{cases} \end{aligned} \quad (2.23)$$

To find the coefficients in C by setting a different problem for each column in (2.15), as follows:

2.4.3 Direct simulation of the microstructure:

- 1st Column of the matrix C:

The following strain is applied to stretch the REV in the fiber direction (x_1 -direction), in order to determine the components C_{il} , with $i = 1, 2,$ and 3 :

$$\epsilon_1^0 = 1 \quad \epsilon_2^0 = \epsilon_3^0 = \gamma_4^0 = \gamma_5^0 = \gamma_6^0 = 0 \quad (2.24)$$

Thus, the displacement boundary conditions (2.21) for the REV in Figure 2.3b become:

$$\begin{aligned} u_1(+a_1, x_2, x_3) - u_1(-a_1, x_2, x_3) &= 2a_1 \\ u_2(+a_1, x_2, x_3) - u_2(-a_1, x_2, x_3) &= 0 \\ u_3(+a_1, x_2, x_3) - u_3(-a_1, x_2, x_3) &= 0 \end{aligned} \quad \begin{cases} -a_2 \leq x_2 \leq a_2 \\ -a_3 \leq x_3 \leq a_3 \end{cases}$$

$$u_i(x_1, +a_2, x_3) - u_i(x_1, -a_2, x_3) = 0 \quad \begin{cases} -a_1 \leq x_1 \leq a_1 \\ -a_3 \leq x_3 \leq a_3 \end{cases} \quad (2.25)$$

$$u_i(x_1, x_2, +a_3) - u_i(x_1, x_2, -a_3) = 0 \quad \begin{cases} -a_1 \leq x_1 \leq a_1 \\ -a_2 \leq x_2 \leq a_2 \end{cases}$$

$$\begin{aligned} u_1(a_1, x_2, x_3) &= a_1 \\ u_1(0, x_2, x_3) &= 0 \\ \sigma_{12}(a_1, x_2, x_3) &= 0 \\ \sigma_{12}(0, x_2, x_3) &= 0 \\ \sigma_{13}(a_1, x_2, x_3) &= 0 \\ \sigma_{13}(0, x_2, x_3) &= 0 \end{aligned} \quad \begin{cases} 0 \leq x_2 \leq a_2 \\ 0 \leq x_3 \leq a_3 \end{cases}$$

$$\begin{aligned} u_2(x_1, a_2, x_3) &= 0 \\ u_2(x_1, 0, x_3) &= 0 \\ \sigma_{21}(x_1, a_2, x_3) &= 0 \\ \sigma_{21}(x_1, 0, x_3) &= 0 \\ \sigma_{23}(x_1, a_2, x_3) &= 0 \\ \sigma_{23}(x_1, 0, x_3) &= 0 \end{aligned} \quad \begin{cases} 0 \leq x_1 \leq a_1 \\ 0 \leq x_3 \leq a_3 \end{cases} \quad (2.26)$$

$$\begin{aligned} u_3(x_1, x_2, a_3) &= 0 \\ u_3(x_1, x_2, 0) &= 0 \\ \sigma_{31}(x_1, x_2, a_3) &= 0 \\ \sigma_{31}(x_1, x_2, 0) &= 0 \\ \sigma_{32}(x_1, x_2, a_3) &= 0 \\ \sigma_{32}(x_1, x_2, 0) &= 0 \end{aligned} \quad \begin{cases} 0 \leq x_1 \leq a_1 \\ 0 \leq x_2 \leq a_2 \end{cases}$$

These boundary conditions are very easy to apply. Symmetry boundary conditions are applied on the planes $x_1 = 0$, $x_2 = 0$, $x_3 = 0$. Then, a uniform displacement is applied on the plane $x_1 = a_1$. The stress boundary conditions do not need to be applied explicitly in a displacement-based formulation. The displacement components in (2.26) represent strains that are non-zero along the x_1 -direction and zero along the other two directions. The stress boundary conditions listed in (2.26) reflect the fact that, in the coordinate system used, the composite material is macroscopically orthotropic and that the constituent materials are orthotropic too. Therefore, there is no coupling between extension and shear strains. This is evidenced by the zero coefficients above the diagonal in columns 4 to 6 in (2.15).

- **2nd Column of the matrix C:**

The components C_{i2} , with $i = 1, 2, 3$, are determined by setting

$$\epsilon_2^0 = 1 \quad \epsilon_1^0 = \epsilon_3^0 = \gamma_4^0 = \gamma_5^0 = \gamma_6^0 = 0 \quad (2.27)$$

Thus, the following boundary conditions on displacements can be used:

$$\left. \begin{aligned} u_1(a_1, x_2, x_3) &= 0 \\ u_1(0, x_2, x_3) &= 0 \\ u_2(x_1, a_2, x_3) &= a_2 \\ u_2(x_1, 0, x_3) &= 0 \\ u_3(x_1, x_2, a_3) &= 0 \\ u_3(x_1, x_2, 0) &= 0 \end{aligned} \right\} \quad (2.28)$$

- **3rd Column of the matrix C:**

The components $C_{\alpha 3}$, with $\alpha = 1, 2, 3$, can be found by applying the following strain

$$\epsilon_3^0 = 1 \quad \epsilon_1^0 = \epsilon_2^0 = \gamma_4^0 = \gamma_5^0 = \gamma_6^0 = 0 \quad (2.29)$$

Thus, the following boundary conditions on displacements can be used

$$\left. \begin{aligned} u_1(a_1, x_2, x_3) &= 0 \\ u_1(0, x_2, x_3) &= 0 \\ u_2(x_1, a_2, x_3) &= 0 \\ u_2(x_1, 0, x_3) &= 0 \\ u_3(x_1, x_2, a_3) &= a_3 \\ u_3(x_1, x_2, 0) &= 0 \end{aligned} \right\} \quad (2.30)$$

- **4th Column of the matrix C:**

For a transversally isotropic material, according to (2.15), only the term C_{44} is expected to be different from zero and it can be determined as a function of the other components, so no further computation is needed. Therefore, it can be determined as:

$$C_{44} = \frac{1}{2} (C_{22} - C_{23}) \quad (2.28)$$

If the material is orthotropic, a procedure similar to that used for column number six must be used.

- **5th Column of the matrix C:**

For a transversally isotropic material, according to (2.15), only the term C_{55} is different from zero and it is equal to C_{66} , which can be found from column number six. If the material is orthotropic, a procedure similar to that used for column number six must be used.

- **6th Column of the matrix C:**

Because of the lack of symmetry of the loads, in this case it is not possible to use boundary conditions as was done for the first three columns. Thus, the boundary conditions must be enforced by using coupling constraint equations (called CE in most FEA commercial packages). According to (2.15), only the term C_{66} is different from zero. The components $C_{\alpha 6}$ are determined by setting:

$$\gamma_4^0 = \epsilon_{12}^0 + \epsilon_{21}^0 = 1 \quad \epsilon_1^0 = \epsilon_2^0 = \epsilon_3^0 = \gamma_4^0 = \gamma_5^0 = 0 \quad (2.29)$$

Note that $\epsilon_{12}^0 = 1/2$ is applied between $x_1 = \pm a_1$ and another one-half is applied between $x_2 = \pm a_2$. In this case, the CE applied between two periodic faces (except points in the edges and vertices) is given as a particular case of (2.21) as follows:

$$\begin{aligned} u_i(x_1, a_2, x_3) - u_i(x_1, -a_2, x_3) &= 0 \\ u_i(x_1, a_2, x_3) - u_i(x_1, -a_2, x_3) &= a_1 \\ u_i(x_1, a_2, x_3) - u_i(x_1, -a_2, x_3) &= 0 \\ u_i(x_1, a_2, x_3) - u_i(x_1, -a_2, x_3) &= a_2 \\ u_i(x_1, a_2, x_3) - u_i(x_1, -a_2, x_3) &= 0 \\ u_i(x_1, a_2, x_3) - u_i(x_1, -a_2, x_3) &= 0 \end{aligned} \quad \begin{cases} -a_2 \leq x_2 \leq a_2 \\ -a_3 \leq x_3 \leq a_3 \\ -a_1 \leq x_2 \leq a_1 \\ -a_3 \leq x_3 \leq a_3 \end{cases} \quad (2.30)$$

$$\begin{aligned}
u_i(x_1, a_2, x_3) - u_i(x_1, -a_2, x_3) &= 0 \\
u_i(x_1, a_2, x_3) - u_i(x_1, -a_2, x_3) &= 0 & \begin{cases} -a_1 \leq x_1 \leq a_1 \\ -a_2 \leq x_2 \leq a_2 \end{cases} \\
u_i(x_1, a_2, x_3) - u_i(x_1, -a_2, x_3) &= 0
\end{aligned}$$

One way to solve homogenization problems is to use numerical simulation techniques on microstructure samples. In this case, the notion of REV is of paramount importance. Usually considered as a volume of heterogeneous material efficiently including a sampling of all heterogeneities, Furthermore, the response of the REV must be independent of the type of conditions at the limits prescribed on its edge (average stress or given average force) [45].

To determine the homogenized properties of a heterogeneous material, it is necessary to calculate the mean stress and strain on the REV using (2.5) and (2.6), then (2.8) and (2.10) the stiffness or flexibility constants can be deduced using (2.3) and (2.4).

PARAPGRAPH OF FLAW CHART

2.5 Homogenization flowchart:

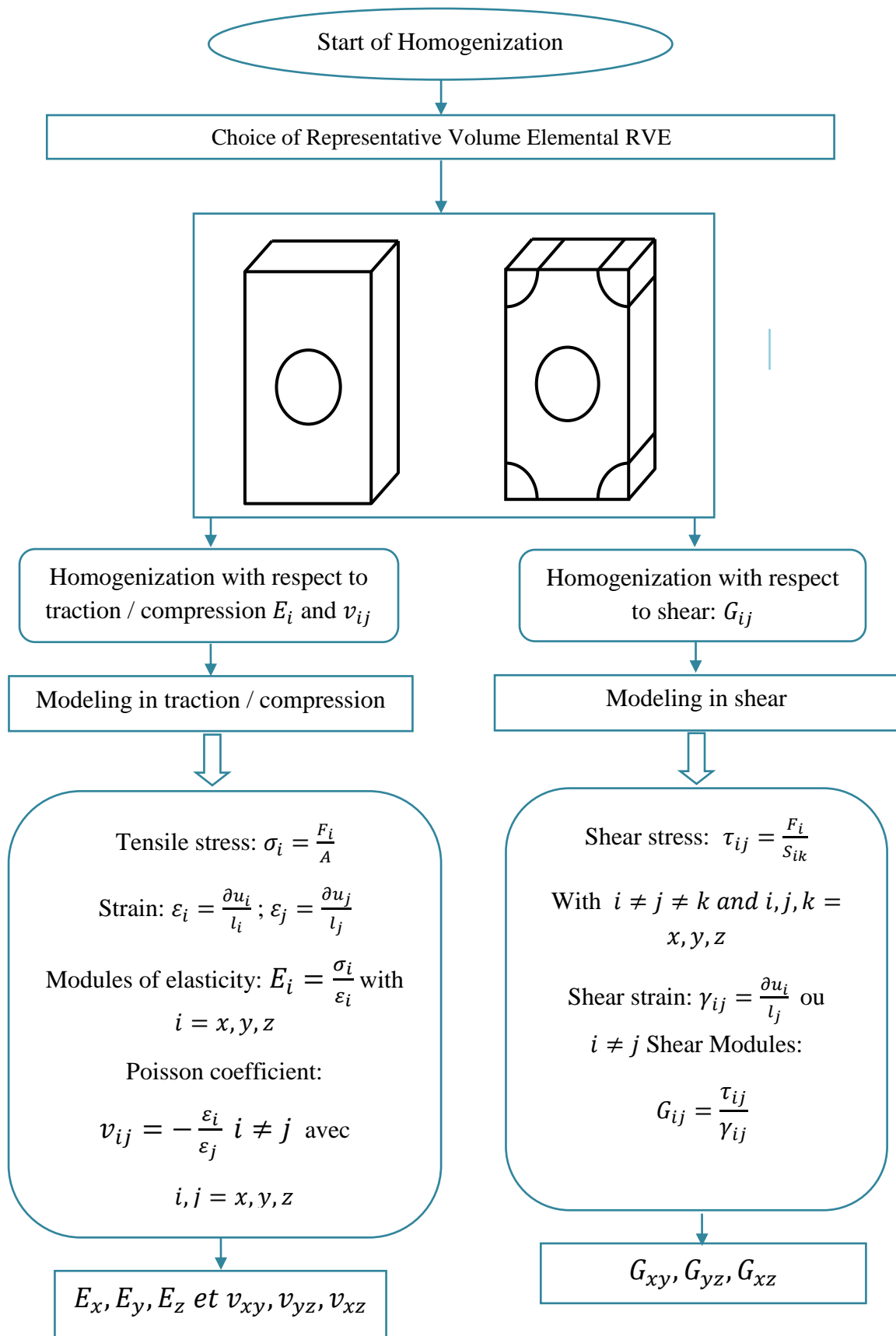


Fig.2.4: Homogenization flowchart

2.6 Conclusion:

In this chapter, a very brief review of the behavior law and different approaches to the calculation of analytical and numerical homogenization were presented. Each one of these later was well adapted to defined problems.

The homogenization computation allows us to obtain an approximation of the effective properties for a medium described by heterogeneous properties.

CHAPTER 3

XFEM coupled with
multi Level-set(s)
technique and
presentation of the
elaborated code

CHAPTER 3

XFEM coupled with multi Level-set(s) technique
and presentation of the elaborated code

The presence of discontinuities in the structures (inclusions, voids and cracks), poses the problem of their numerical representation, several solutions have been proposed among which the extended finite element method (X-FEM), recognized for its ability to model weak (inclusion) and strong (void and crack) discontinuities. Initially, the technique used to model interfaces with XFEM elements consisted in representing them explicitly by parametric curves. However, very quickly, researchers began to study several interfaces that coalesce, which was obviously not without some difficulties in the representation of these interfaces. Therefore, another method had to be considered; it consists in representing the interfaces implicitly by a surface called Level Set. This method is of particular interest to us in our study, since it could allow us to modify the shape of the interface, without any restriction on the connectivity of the structural elements.

SUMMARY

3.1	The extended finite element method (XFEM)	42
3.1.1	Implementation of the XFEM method	42
3.1.2	The enrichment of inclusion	42
3.1.3	The enrichment of void	43
3.1.4	The enrichment of crack	43
3.2	Application of the XFEM	44
3.3	The Level-Set method	46
3.3.1	The coupling of the Level-Set technique with the XFEM method	46
3.3.2	Description of a crack by LSM	51
3.4	Presentation of the compute code without surface effect	52
3.4.1	Flow chart of our compute code	52
3.4.2	Presentation of the developed program levels	54
3.4.3	Design and definition of geometry and meshing parameters by G-mesh	54
3.4.4	The numbering of elements and nodes	55
3.4.5	Construction of elementary stiffness matrices	56
3.4.6	Assembly procedure (Location of K_e)	58
3.4.7	Resolution of the System	59
3.4.8	Calculation of strains and stresses	60
3.4.9	Homogenization computing	60
3.5	Conclusion	61

3.1 The extended finite element method (XFEM):

3.1.1 Implementation of the XFEM method:

The XFEM is used to represent the discontinuities independently of the finite element mesh by exploiting the Partition Unit Finite Element Method (PUFEM). Arbitrary-oriented discontinuities can be modelled by enriching all discontinued elements by using enrichment functions that satisfy the discontinuous behaviour and adding additional nodal degrees of freedom (DOF). In general, the approximation of the displacement field in the XFEM takes the following form:

$$\mathbf{u}(\mathbf{x}) = \mathbf{u}^{\text{FEM}} + \mathbf{u}^{\text{Enr}} = \underbrace{\sum_{i \in \Omega} \mathbf{N}_i(\mathbf{x}) \mathbf{u}_i}_{\text{FEM}} + \underbrace{\sum_{j \in \Omega_d} \mathbf{N}_j(\mathbf{x}) \mathbf{a}_j}_{\text{Enrichment}} \quad (3.1)$$

Ω and Ω_d	: Elements in the whole domain and elements in the domain containing discontinuities, respectively;
$N_i(\mathbf{x})$: Conventional interpolation function;
$N_j(\mathbf{x})$: The enrichment interpolation functions of the discontinuity;
u_i and a_j	: The classic and the enriched DOF respectively.

3.1.2 The enrichment of inclusion:

Inclusions are defined as heterogeneities in a matrix with different material properties. A practical way to represent this discontinuity created by the bi-material interface, across which a continuity of displacement and stress fields and a discontinuity the strain one, is to consider the following enrichment function:

$$\mathbf{u}^{\text{Enr}} = \sum_{j \in \Omega_d} \mathbf{N}_j(\mathbf{x}) \psi(\mathbf{x}) \quad (3.2)$$

Where $\psi(\mathbf{x})$ is the value of level-set at a given point or is the shortest signed-distance from any point in the domain of discontinuity at the interface, in order to ensure the correspondence between real displacement and enriched displacement at node levels, $\psi(\mathbf{x})$ is modified by Moës et al. [36] as follows:

$\psi(\mathbf{x}) - \psi(\mathbf{x}_j)$ with \mathbf{x}_j corresponding to the nodes of the concerned element. The formulation of equation (3.1) in this case can be expressed:

$$\mathbf{u}(\mathbf{x}) = \sum_{i \in \Omega} \mathbf{N}_i(\mathbf{x}) \mathbf{u}_i + \sum_{j \in \Omega_d} \mathbf{N}_j(\mathbf{x}) (\psi(\mathbf{x}) + \psi(\mathbf{x}_j)) \mathbf{a}_j \quad (3.3)$$

3.1.3 The enrichment of void:

In the case of the presence of a void, the equation (3.1) becomes [17]:

$$\mathbf{u}(\mathbf{x}) = \mathbf{V}(\mathbf{x}) \sum_{i \in \Omega} \mathbf{N}_i(\mathbf{x}) \mathbf{u}_i \quad (3.4)$$

$\mathbf{V}(\mathbf{x})$ is the enrichment of voids taking a value of 0 inside the void and 1 outside the void.

3.1.4 The enrichment of crack:

For the modelling of a crack in a homogeneous material, the enrichment is defined for an element completely cut by the crack (see Fig.3.1), by the enrichment Heaviside function of $\mathbf{H}(\mathbf{x})$ as such:

$$\mathbf{H}(\mathbf{x}) = \begin{cases} +1 & \text{above the crack} \\ -1 & \text{below the crack} \end{cases} \quad (3.5)$$

In order to ensure the correspondence between real displacement and enriched displacement at node levels, $\mathbf{H}(\mathbf{x})$ has been modified by Moës et al. [36] to: $\mathbf{H}(\mathbf{x}) - \mathbf{H}(\mathbf{x}_j)$ with \mathbf{x}_j corresponding to the nodes of the concerned element. So like equation (3.1), the displacement field becomes:

$$\mathbf{u}(\mathbf{x}) = \sum_{i \in \Omega} \mathbf{N}_i(\mathbf{x}) \mathbf{u}_i + \sum_{j \in \Omega_H} \mathbf{N}_j(\mathbf{x}) (\mathbf{H}(\mathbf{x}) - \mathbf{H}(\mathbf{x}_j)) \mathbf{a}_j \quad (3.6)$$

It should be noted that there is a third term in the expression of $\mathbf{u}(\mathbf{x})$ which expresses the singularity of the fields near the end of the crack. This term paramount is the calculations of the local parameters such as the stress intensity factor where it is not necessary in this study since we do not land at these parameters at this stage (this will be incorporated in our code in the future work).

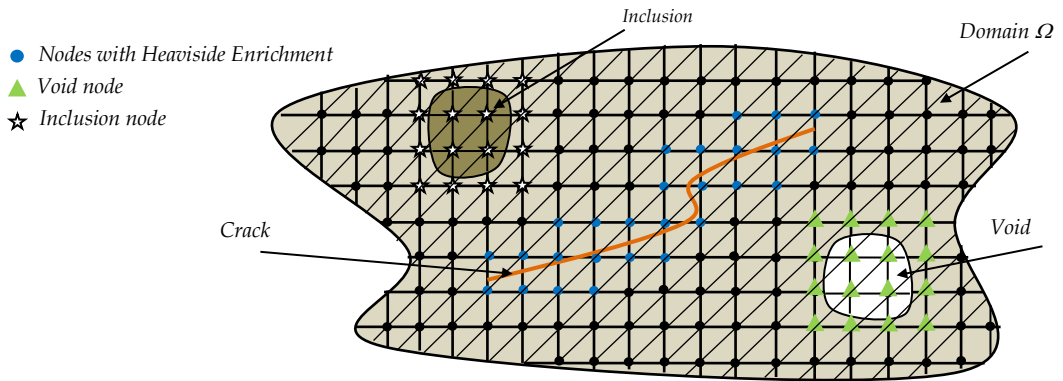


Fig 3.1: Different types of XFEM enrichments

3.2 Application of the XFEM:

The Bubnov-Galerkin method can be used to convert the displacement approximation given by equation (3.1) into a system of linear equations of form:

$$Ku = f \quad (3.7)$$

With

K : global stiffness matrix.

u : nodal displacement vector.

f : nodal force vector.

By appropriately ordering degrees of freedom, the overall stiffness matrix K can be considered as:

$$K = \begin{bmatrix} k_{uu} & k_{ua} \\ k_{ua} & k_{aa} \end{bmatrix} \quad (3.8)$$

Where:

k_{uu} : The rigidity matrix of classical elements.

k_{aa} : The stiffness matrix of the enriched elements.

k_{ua} : The coupling matrix between classical and enriched stiffness components.

The elementary stiffness matrix K for any member of k can be calculated as follows:

$$k_e = \int_{\Omega} B_{\alpha}^t C B_{\beta} d\Omega \quad \alpha, \beta = u, a \quad (3.9)$$

With:

C : the matrix of elastic properties.

B_u : is the matrix of the derivatives of the classical form function.

B_a : is the matrix of the derivatives of the enriched form function.

The general form of B_u and B_a is given by:

$$B_u = \begin{bmatrix} N_{i,x} & 0 & 0 \\ 0 & N_{i,y} & 0 \\ 0 & 0 & N_{i,z} \\ 0 & N_{i,z} & N_{i,y} \\ N_{i,z} & 0 & N_{i,x} \\ N_{i,y} & N_{i,x} & 0 \end{bmatrix} \quad (3.10)$$

$$B_a = \begin{bmatrix} (N_i \psi)_x & 0 & 0 \\ 0 & (N_i \psi)_y & 0 \\ 0 & 0 & (N_i \psi)_z \\ 0 & (N_i \psi)_z & (N_i \psi)_y \\ (N_i \psi)_z & 0 & (N_i \psi)_x \\ (N_i \psi)_y & (N_i \psi)_x & 0 \end{bmatrix} \quad \text{For inclusion} \quad (3.11)$$

$$B_a = \begin{bmatrix} (N_i H)_x & 0 & 0 \\ 0 & (N_i H)_y & 0 \\ 0 & 0 & (N_i H)_z \\ 0 & (N_i H)_z & (N_i H)_y \\ (N_i H)_z & 0 & (N_i H)_x \\ (N_i H)_y & (N_i H)_x & 0 \end{bmatrix} \quad \text{For crack} \quad (3.12)$$

Similarly, f in equation (3.8) is given by: $f' = \{f'_u \quad f'_a\}$

Where f_u and f_a are the vectors of the applied forces for the classical and enriched components of the displacement approximation, the vectors f_u and f_a are given in terms of applied tractions $\bar{\mathbf{t}}$ and the volume forces \mathbf{b} as:

$$f_u = \int_{\Gamma_i} N_i \bar{\mathbf{t}} d\Gamma + \int_{\Omega} N_i \mathbf{b} d\Omega \quad (3.13)$$

$$f_a = \int_{\Gamma_i} N_i \psi \bar{\mathbf{t}} d\Gamma + \int_{\Omega} N_i \psi \mathbf{b} d\Omega \quad (3.14)$$

$$f_a = \int_{\Gamma_i} N_i H \bar{\mathbf{t}} d\Gamma + \int_{\Omega} N_i H \mathbf{b} d\Omega \quad (3.15)$$

3.3 The Level-Set method:

The Level-Set method or level function method is an interface monitoring technique initially developed in 1987.

In 1988, Osher and Sethian published a synthesis of expertise in interface evolution and hyperbolic conservation laws in an article. The simple and versatile method to compute and analyze the motion of an interface in two or three dimensions, one of the initial motivations was to develop a simple interface tracking technique that could correctly describe topological changes.

The main idea of this method is to describe an interface in two or three dimensions by a signed function called Level-Set function. The temporal tracking of this interface is determined by solving a non-conservative advection equation of the scalar: the Level-Set equation.

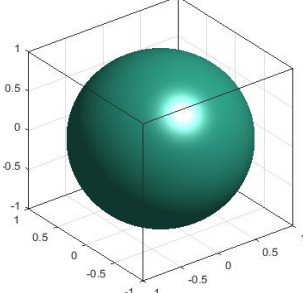
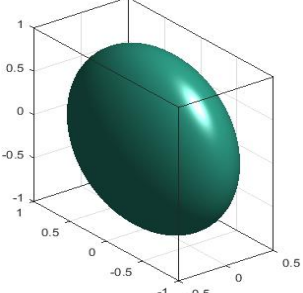
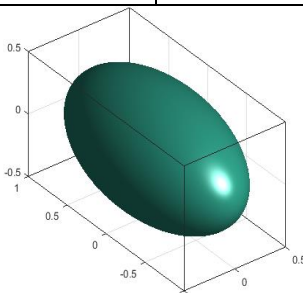
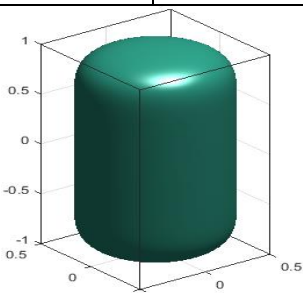
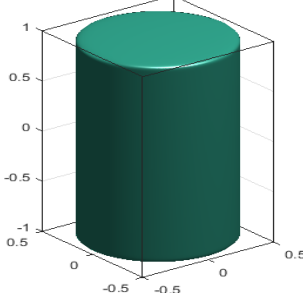
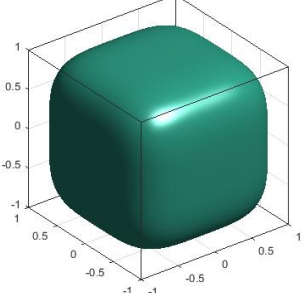
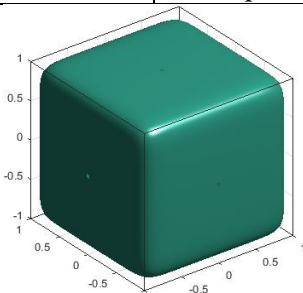
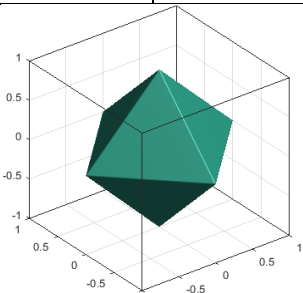
3.3.1 The coupling of the Level-Set technique with the XFEM method:

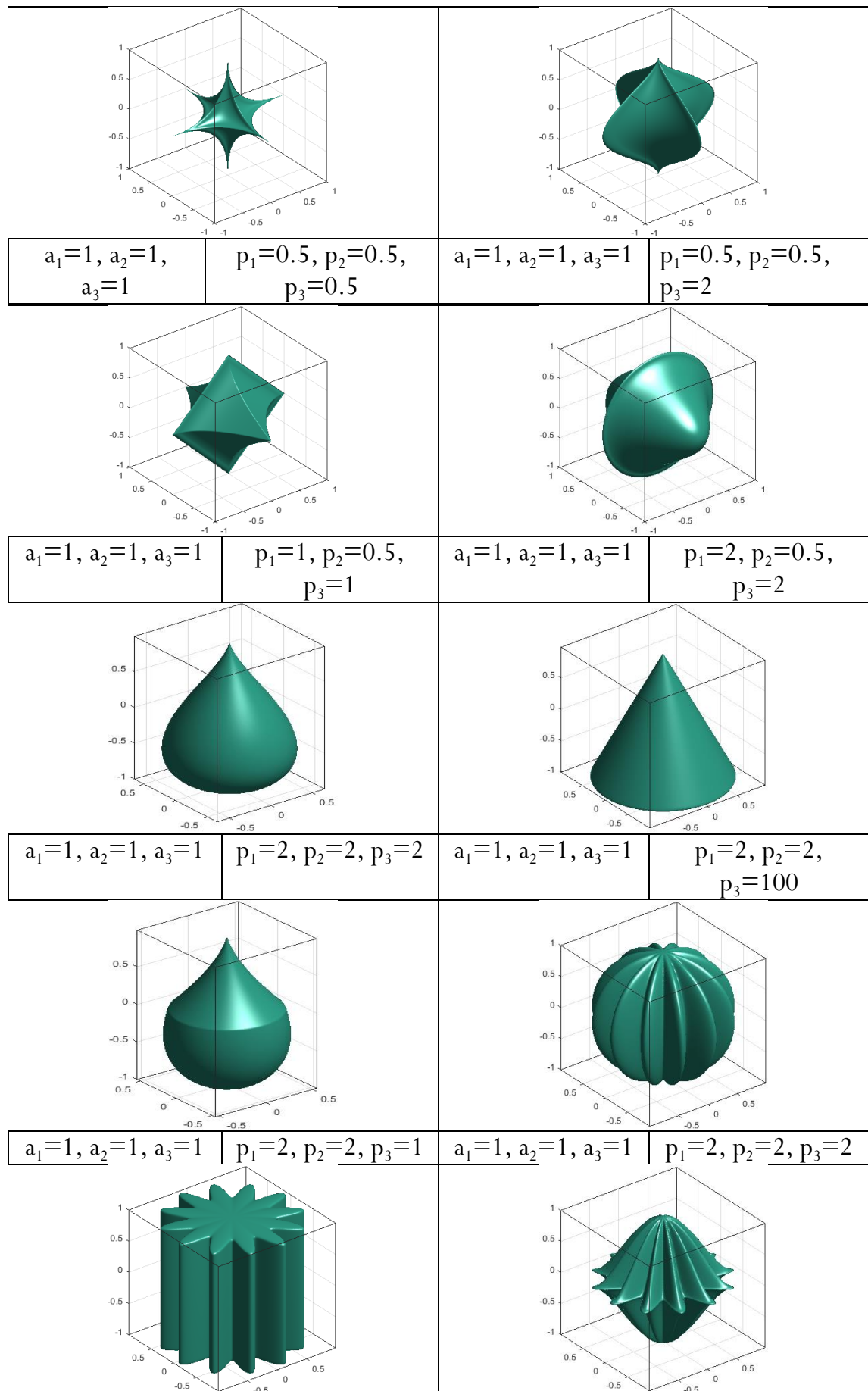
Consider a discretization of the domain (Ω) into n_e elements (of tetrahedral linear type in this study) thus generating n_d nodes. By using the Level-Set technique, the nodes do not necessarily need to be located at the interface described by the level function ϕ , taking a zero value on that location. Hence, the mesh is independent of Γ . Thus, the value of ϕ at each point of the domain (Ω) will be of capital importance for defining the point relative position to the interface, during the different stages of the discretization. The Level-Set function used in this study is, [46]:

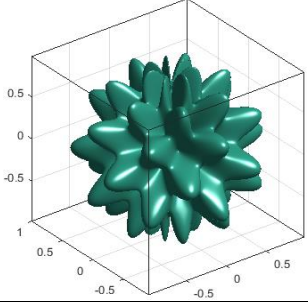
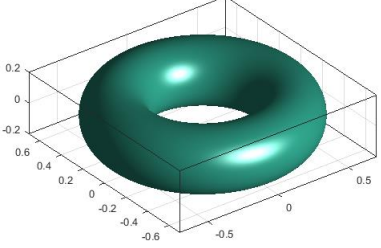
$$\phi(\mathbf{x}) = \left(\frac{|x-x_c|}{a_1}\right)^{p_1} + \left(\frac{|y-y_c|}{a_2}\right)^{p_2} + \left(\frac{|z-z_c|}{a_3}\right)^{p_3} - 1 \quad (3.16)$$

By varying the parameters a_i and p_i , this function allows to describe various closed forms of center coordinates (x_c, y_c, z_c) , such as sphere, 3D star, polygon, cube, cylinder, cone, etc (see table.3.1). The coming parametric studies of the effect of the discontinuity/interface shape, geometrically governed by function ϕ , will demonstrate the large options enabled by this function.

Table 3.1:Deffrent forme of Level-set(s)

			
$a_1=1, a_2=1, a_3=1$	$p_1=2, p_2=2, p_3=2$	$a_1=0.5, a_2=1, a_3=1$	$p_1=2, p_2=2, p_3=2$
			
$a_1=0.5, a_2=1, a_3=0.5$	$p_1=2, p_2=2, p_3=2$	$a_1=0.5, a_2=0.5, a_3=1$	$p_1=2, p_2=2, p_3=10$
			
$a_1=0.5, a_2=0.5, a_3=1$	$p_1=2, p_2=2, p_3=100$	$a_1=1, a_2=1, a_3=1$	$p_1=4, p_2=4, p_3=4$
			
$a_1=1, a_2=1, a_3=1$	$p_1=10, p_2=10, p_3=10$	$a_1=1, a_2=1, a_3=1$	$p_1=1, p_2=1, p_3=1$



$a_1=1, a_2=1, a_3=1$	$p_1=2, p_2=2,$ $p_3=100$	$a_1=1, a_2=1, a_3=1$	$p_1=2, p_2=2,$ $p_3=0.5$
			
$a_1=1, a_2=1, a_3=1$	$p_1=2, p_2=2, p_3=2$	$a_1=1, a_2=1, a_3=1$	$p_1=2, p_2=2, p_3=2$

The unit normal at each point x in the vicinity of Γ is defined as a function of ϕ by:

$$\mathbf{n}(x) = \frac{\nabla \tilde{\phi}(x)}{\|\nabla \tilde{\phi}(x)\|} \quad (3.17)$$

With

$$\nabla \tilde{\phi}(x)_i = \sum_{j=1}^n \frac{\partial N_j(x)}{\partial x_i} \phi_j \quad (3.18)$$

The intersection of mesh elements with the interface is approximated, depending of the element orientation, either by a triangle (see figure 3.2a) or by a quadrangle (see figure 3.2b). The first case generates a sub-tetrahedron and a prismatic sub-element, while the second generates two prismatic sub-elements. Each prism (in both cases) is subdivided into three sub-tetrahedra. The identification of these sub-elements is primordial with elements that are cut by the interface.

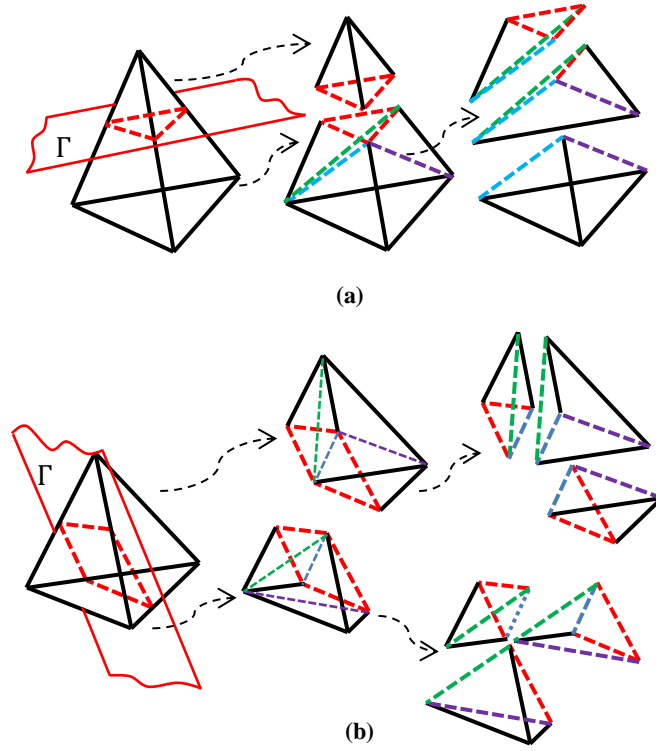


Fig 3.2: Subdivision of the tetrahedron cut element: **a)** into 4 sub-elements, **b)** into 6 sub-elements.

As shown in figure 3.3, the vertices of these intersections are obtained using a linear interpolation approximation of the Level-Set ϕ evaluated at the two nodes i and j of each element cut side. Drawing \bar{x} from the equation $\phi(x)=0$ gives the coordinates of these vertices:

$$\bar{x} = f(\bar{x}_i, \phi_i, \bar{x}_j, \phi_j) \quad (3.19)$$

$$\bar{x} = \bar{x}_i + \xi(\bar{x}_j - \bar{x}_i) \quad \text{with} \quad \xi = \frac{\phi_i}{\phi_i - \phi_j} \quad (3.20)$$

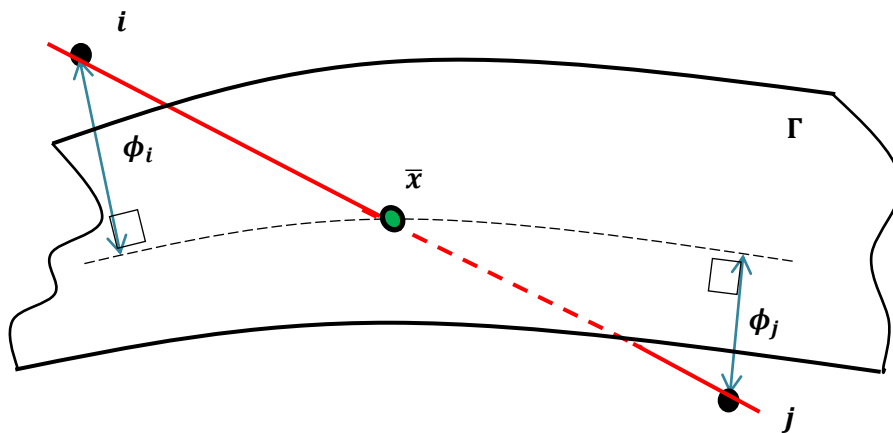


Fig.3.3: Description of Level-set linear interpolation.

3.3.2 Description of a crack by LSM:

The Level-Set method offers an elegant way to model different kind of discontinuities such as cracks. The key point in modelling of cracks or any discontinuity using the Level-Set method, is to represent the discontinuity as a Level-Set zero-level of this function [47]. For crack modelling, the Level-Set function is defined as a signed distance function. As the crack is a discontinuity that does not completely divide the domain into two distinct parts. So, only a part of the domain is divided to completely characterize a crack. For that two functions of Level-Set are defined by:

- A normal Level-Set (**LS_n**) that represents the distance to the surface of the crack.
- A tangent Level-Set (**LS_t**) that represents the distance to the crack tip.

The zero level of the normal Level-Set defines the surface of the crack, extended by continuity to the entire domain. The intersection of the zero-levels of the two Level-Set defines the crack tip. In addition, the sign of the tangent Level-Set is chosen so that the surface of the crack corresponds to the space generated by the sign of the normal Level-Set is chosen arbitrarily. The points x for which is negative are said to be "below" the crack, and those for which is positive are said to be "above" the crack [48] (Figure.3.4).

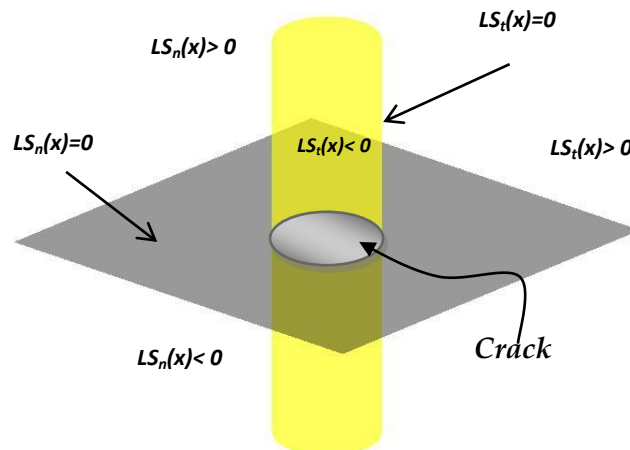


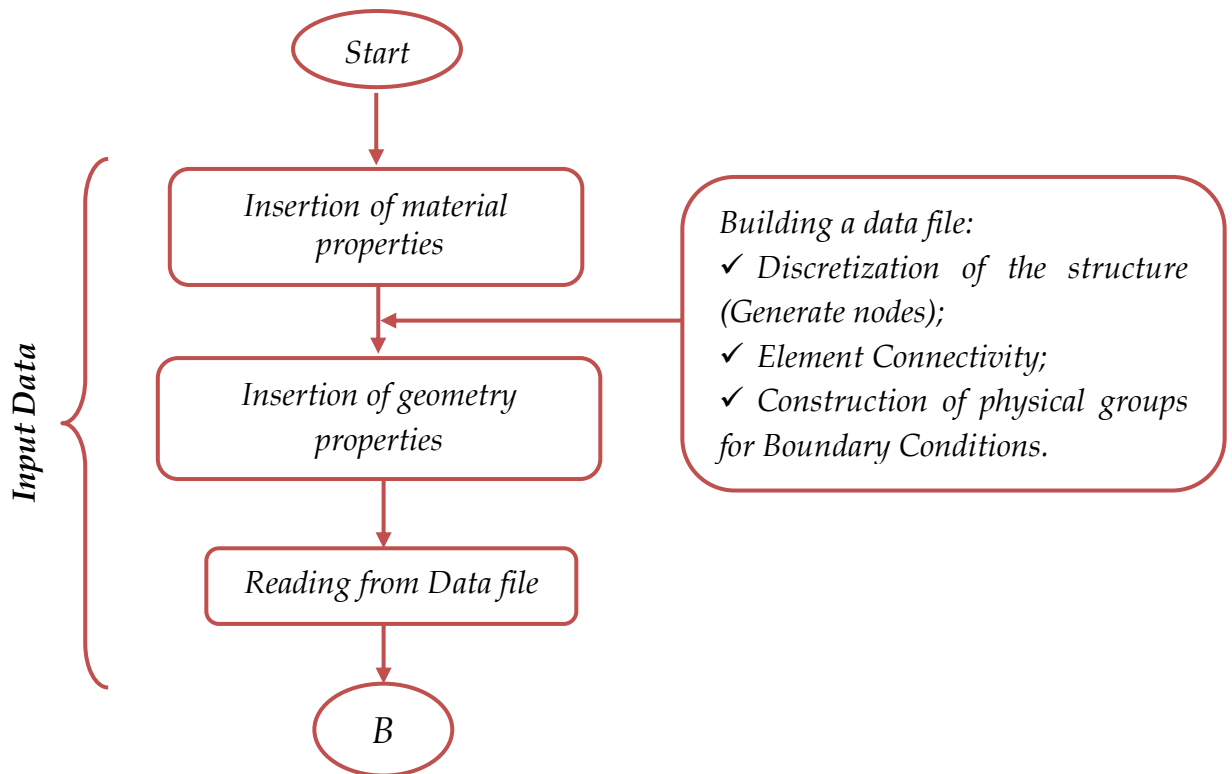
Fig.3.4: 3D representation of a crack by Level-Set.

3.4 Presentation of the compute code without surface effect:

In the case of study and analysis of the homogenization of cracked structures by XFEM, several calculation operations must be performed. The calculation time of these last ones becomes very important for complex problems. Therefore, it is essential to develop a reliable calculation code judiciously.

In this part we present our compute code which takes into account the theories studied in the previous chapter. We will propose a flow chart which will explain the approaches of our compute code, in order to show the robustness and performance of the developed program.

3.4.1 Flow chart of our compute code:



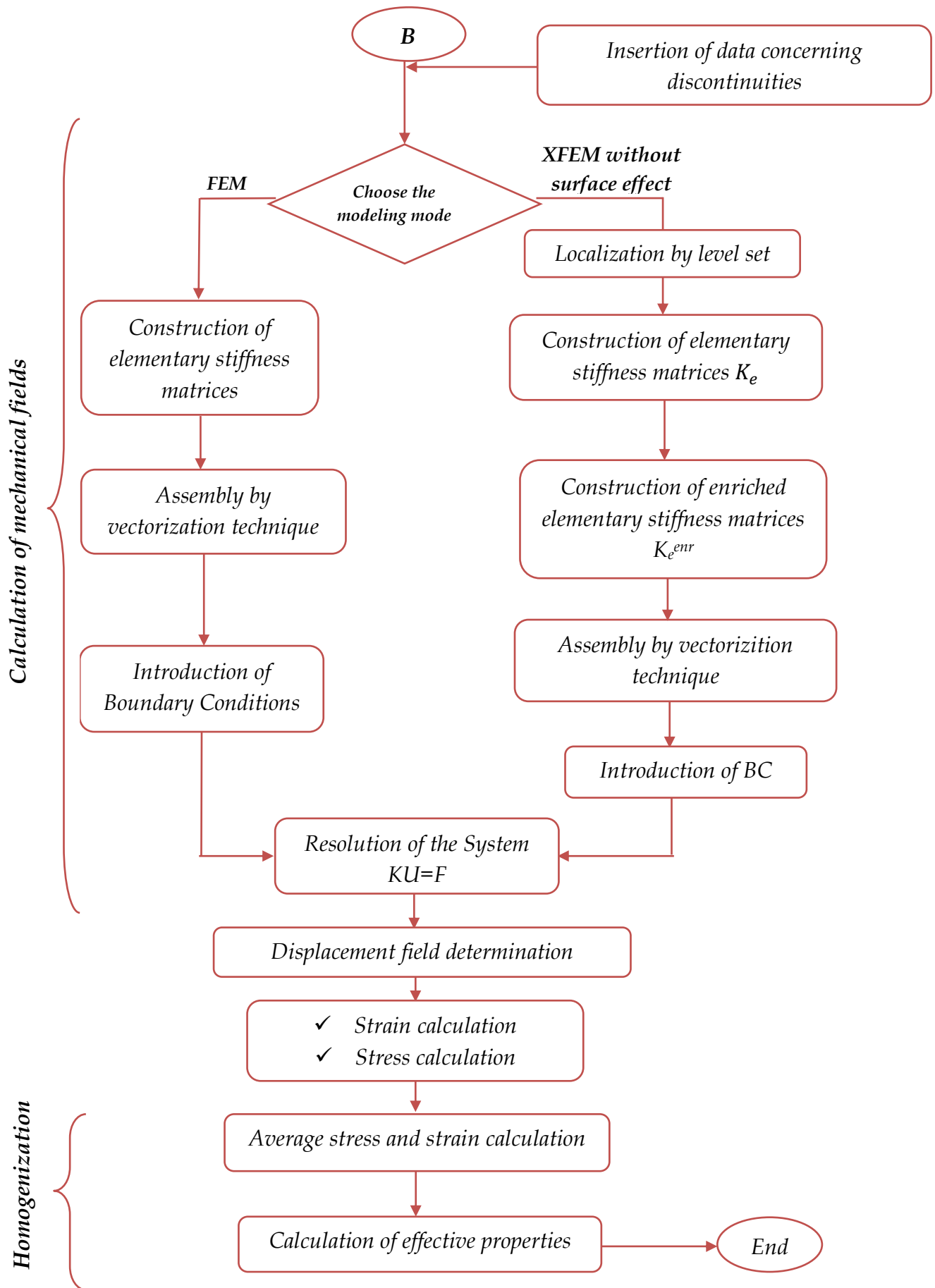


Fig 3.5: Flowchart of our calculation code.

3.4.2 Presentation of the developed program levels:

In this work, the X-FEM modeling method coupled with LS for homogenization described in the previous chapter was programmed, through the use of MATLAB® (R2015b) programming software, our compute program is similar in its composition with any FEM-based program. But with some attention will be given to enrichment and LS. This program consists of the following steps:

- ✓ Data definitions (geometry mesh definition by G-mesh, insertion of material characteristics)
- ✓ Construction of elementary stiffness matrix K_e
- ✓ Location of K_e in the global matrix K_G
- ✓ Insert the boundary conditions.
- ✓ Resolution of the System (computation field of displacement).
- ✓ Calculation of strain and stress field.
- ✓ Calculation field of strain and average stresses.
- ✓ Calculate the effective parameters.
- ✓ Results display.

3.4.3 Design and definition of geometry and meshing parameters by G-mesh:

The mesh is a spatial discretization of a continuous medium. The importance of this operation is to discretize the geometry into elements and nodes, in our work this discretization was performed using G-msh.

G-msh is a free software which allows to generate 2D and 3D finite element type meshes with pre / post processing tools. This software was developed by Christophe Geuzaine et Jean-François Remacle in March 2003.

Meshing geometry through the G-msh has to go through several stages. In this section we mention the most important.

✓ Definition of geometry:

The G-mesh allows defining different geometries, the latter can be created by two methods: at the level of a text file see appendix A1 (fig.1) or at the level of the software's graphical interface, see appendix A1 (fig.2).

✓ Selection of physical groups:

This part is to be done in order to prepare the structure for the injection of the boundary conditions, it allows to consider any part of mesh (line, point, surface, volume) as a physical group see appendix A1 (fig.3).

✓ Mesh generation:

In our case, the element that has chosen is tetrahedron. This element is chosen automatically by G-msh, to generate the mesh of this element just click on 3D see appendix A1 (fig.4).

3.4.4 The numbering of elements and nodes:

The classification of the nodes and the elements is made in qualitative form by G-msh, for example the figure 3.5:

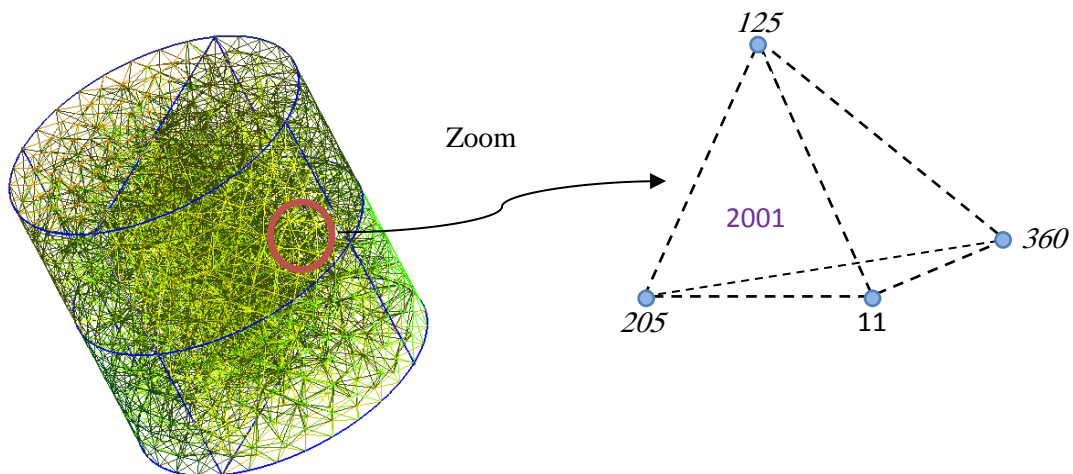


Fig 3.6: Numbering of elements and nodes.

After these steps the software gives a data file which will be used in computation code, at step: mesh with G-msh in the previous flowchart.

3.4.5 Construction of elementary stiffness matrices K_e :

Because of the discontinuity, the calculation of the elementary stiffness matrix will be modified, this latter depends on the nature of the enriched element or not (simple).

In a discretized field (our study case), two types of elements can appear, the elements which are not crossed by the crack (simple element) and the elements which are completely crossed by the crack where the enrichment must be brought to all nodes of these elements. This case requires special digital processing.

Due to the presence of enrichments, there are additional DOF. During a crack which crosses an element, two DOF for each node of the element will be added.

The presence of discontinuity in the elements which are cut by crack poses a problem of their numerical integration. Among the proposed solutions is to increase the number of integration points on either side of the discontinuity by dividing the cut element into simple sub-elements (figure 3.7). One evaluates thereafter the elementary matrix on the points of gauss of these elements.

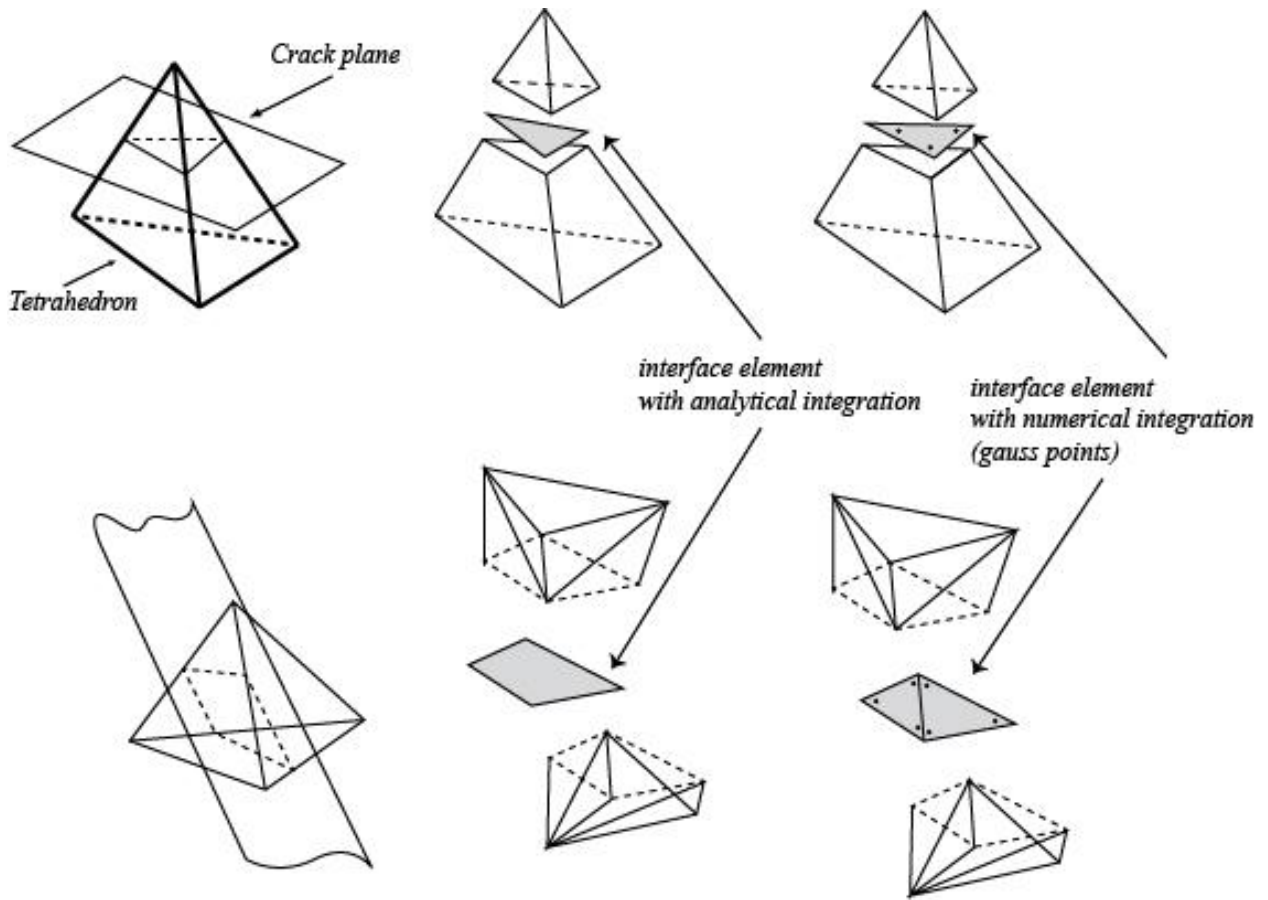


Fig 3.7: Under splitting and distribution of gauss points.

The numerical integration of the elementary matrices of the elements which cut by the crack will be carried out on these sub-elements:

$$K_e = W * B^t * C * B \quad (3.19)$$

Or:

B: *The matrix of derivatives of the interpolation functions;*

B^t: *Transpose from the matrix;*

W: *Gauss point weight;*

C: *Matrix of material properties.*

3.4.6 Assembly procedure (Location of \mathbf{K}_e):

In our computer code, we used a vectorization assembly technique, where for each elementary stiffness matrix, we have:

- ✓ A vector named \mathbf{I}_e which contains the global row indices associated with the elements stored in \mathbf{K}_e .
- ✓ Another vector named \mathbf{J}_g which contains the global column indices associated with the elements stored in \mathbf{K}_e .
- ✓ A vector named \mathbf{k}_g which contains the values of \mathbf{K}_e .
- ✓ Then after the loop of the elements one uses the Sparse instruction (contains the vectors mentioned below) to build the total stiffness matrix \mathbf{K}_G .

We present the optimized code where we completely eliminate loops. This version consists in building 3 tables allowing storing all the elementary matrices as well as the positions in the total matrix. We denote by \mathbf{K}_g , \mathbf{I}_g and \mathbf{J}_g these arrays:

$$\mathbf{K}_g(\text{il},k)=\mathbf{K}_k^e(\text{il})$$

$$\mathbf{I}_g(\text{il},k)=\mathbf{I}_k^e(\text{il})$$

$$\mathbf{J}_g(\text{il},k)=\mathbf{J}_k^e(\text{il})$$

The three local arrays \mathbf{K}_k^e , \mathbf{I}_k^e and \mathbf{J}_k^e are stored in the k-th column of the global arrays \mathbf{K}_g , \mathbf{I}_g and \mathbf{J}_g respectively.

A natural way to build these three arrays consists in using a loop through the triangles T_k in which we insert the local arrays column-wise, see Figure 3.8. Once these arrays are determined, the matrix assembly is obtained with:

$$\mathbf{M}=\text{sparce}(\mathbf{I}_g(:), \mathbf{J}_g(:), \mathbf{K}_g(:), n, n)$$

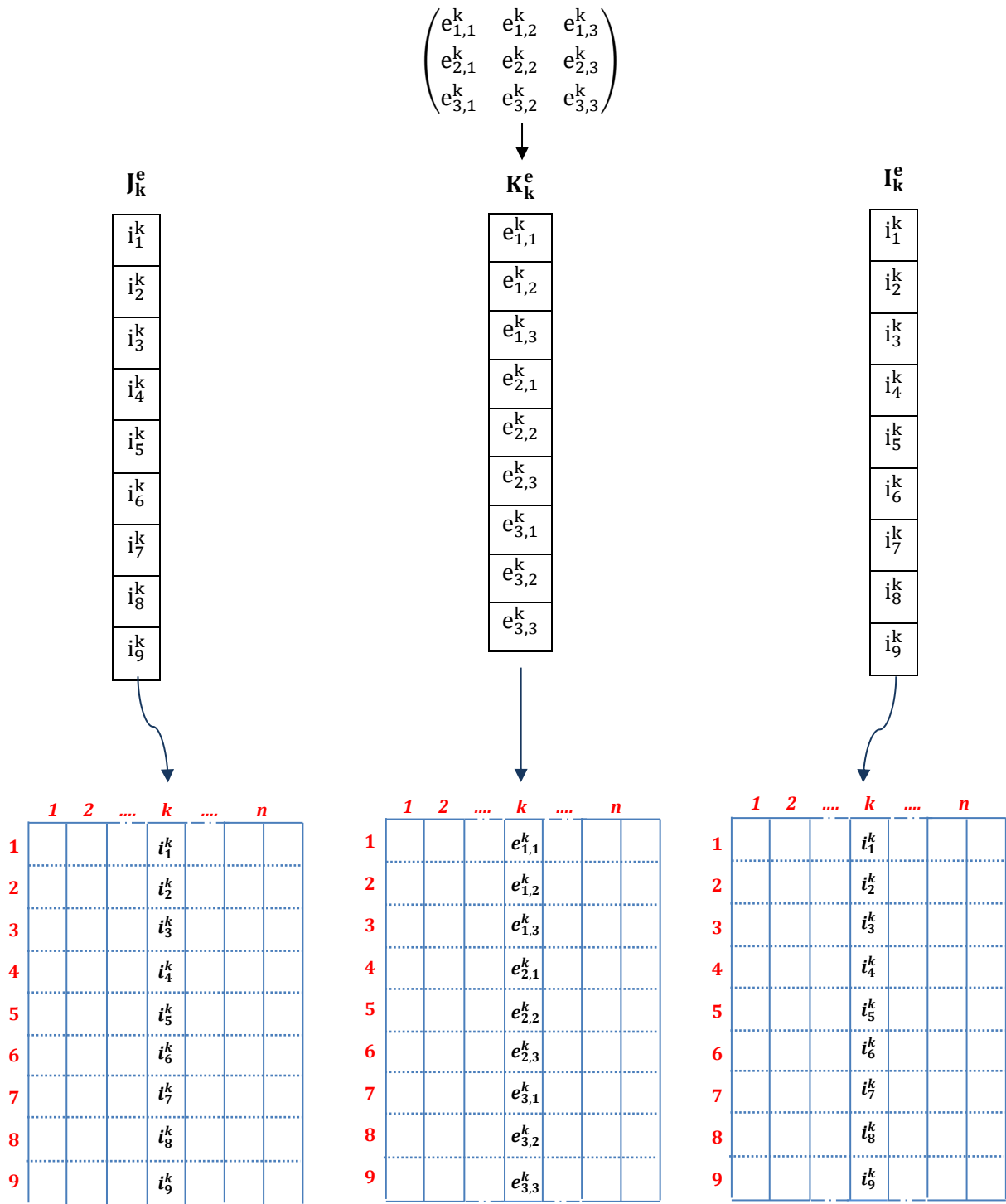


Fig 3.9: Insertion of an element matrix in the global array.

3.4.7 Resolution of the System:

In this step for the compute code we are going to notice the methods of resolution of the system $KU=F$.

The developed computer code contains two methods to solve the system: iterative and direct methods. In general, direct methods are used as long as it is possible and that it does not cost too much in terms of computation time and consumes more RAM. Otherwise, failing that, the iterative methods are used such as: (minres, bicg, bicgstab, gmres, cgs, symmlq) these later consume less RAM and is a bit slow in terms of time.

3.4.8 Calculation of strains and stresses:

The computation of field of the strains and the stresses is to carry out to make a buckle on the elements (simple and enriched):

- The following relation allows us to calculate the strain field for classical elements (not cut elements) :

$$\{\boldsymbol{\varepsilon}\} = [\mathbf{B}]\{\mathbf{u}\} \quad (3.20)$$

And for the stress field we have:

$$\{\boldsymbol{\sigma}\} = [\mathbf{C}]\{\boldsymbol{\varepsilon}\} \quad (3.21)$$

3.4.9 Homogenization computing:

The homogenization is the last step in the process; it aims to determine the effective elastic properties at the macroscopic scale by determining the relationship between macroscopic stresses and macroscopic deformations.

Then the effective parameters can be calculated after applying equation (2.25) and the following formula:

$$\left. \begin{aligned} \bar{\sigma}_{22} &= C_{12} = \lambda_{eff} \\ \frac{c_{11}-c_{12}}{2} &= \frac{\bar{\sigma}_{11}-\bar{\sigma}_{12}}{2} = \frac{(\lambda_{eff}+2\mu_{eff})-\lambda_{eff}}{2} \\ k_{eff} &= \lambda_{eff} + \left(\frac{2}{3}\right)\mu_{eff} \end{aligned} \right\} \quad (3.21)$$

Where:

$\bar{\sigma}$: Medium stress

λ_{eff} and μ_{eff} : Effective lamé constants

k_{eff} : Effective compressibility modulus

3.5 Conclusion:

The extended finite element method is a modern modelling method that gives a numerical solution, which effectively makes sense of discontinuities. The representation of these later is based on the Level-Set technique; this description is then used to enrich the displacement field. The success of discontinuities representation using the level-set method allows it to be coupled with other methods (e.g. LSM coupling with XFEM).

For the second part, all the steps were put into practice by a computer code created within our research team from the LDMM research lab, from the University of Djelfa.

Our compute code will be tested through several validation and application examples in the next chapter.

CHAPTER 4

Validation of the code and parametric studies in displacement analysis and homogenization without surface effect

CHAPTER 4

Validation of the code and parametric studies in displacement analysis and homogenization without surface effect

In this chapter, we are interested in the validation and application examples in order to prove the efficiency and the robustness of our numerical simulation tool without surface effect. Firstly, the obtained results for several validation tests are compared to those evaluated analytically and those obtained by using the free software “Caste3M2018” based on the Finite Element Method (FEM). After that and as a parametric study in homogenization context, several cases of Representative Elementary Volume (REV) are then studied, to get the evolution of the bulk compressibility modulus according to the void flattening ratio and according to its size when the void became a crack.

SUMMARY

4.1	Validation of the calculation code	64
4.1.1	Spherical inclusion in cube subjected to axial tensile load	64
4.1.2	Semi-circular surface crack into cube under tension	65
4.1.3	Crossing crack into cube under tension	67
4.1.4	Annular surface crack into a cylinder under tension	68
4.1.5	Elliptical crack forms into a cylinder under tension	69
4.2	Parametric study for homogenization	70
4.2.1	Flattened cylindrical void with respect to a crossing crack	70
4.2.2	Flattened spherical void with respect to a circular crack	71
4.2.3	Influence of the size effect of the crack	72
4.3	Conclusion	73

4.1 Validation of the calculation code:

In this part, we are interested in some examples of validation, in order to prove the efficiency and the robustness of the elaborated software of computation. This is possible by comparing the obtained results with the analytical solution when it is available, otherwise with those obtained by standard software based on FEM. In all presented simulations, the meshing was realized by the free software Gmsh (version 4.4.1) [49] with 4-nodes tetrahedron linear element. The mesh size varies from $h_e = 1/21$ for a cube (from 71299 to 53320 elements and from 285196 to 213280 nodes) to $h_e = 1/50$ for a cylinder (115897 elements and 463588 nodes), as well in the developed software as in standard FEM.

4.1.1 Spherical inclusion in cube subjected to axial tensile load:

In this example, the geometrical characteristics and the mechanical properties are grouping in table 1. As shown in Figure 4.1. This cube is subjected to a static loading q in the z-axis, and the analytical solution of the displacement field of this problem is given in the reference [50].

Table 4.1: Mechanical properties and Geometrical characteristics for example 1

<i>Mechanical properties</i>	
E_1 (Young's modulus of matrix)	1 GPa
E_2 (Young's modulus of inclusion)	10 GPa
ν_1 (Poisson's ratio of matrix)	0.25
ν_2 (Poisson's ratio of inclusion)	0.32
q (Static loading)	20 N/m ²
<i>Geometrical characteristics</i>	
L (Cube side)	1 m
R (Inclusion radius)	0.2 m

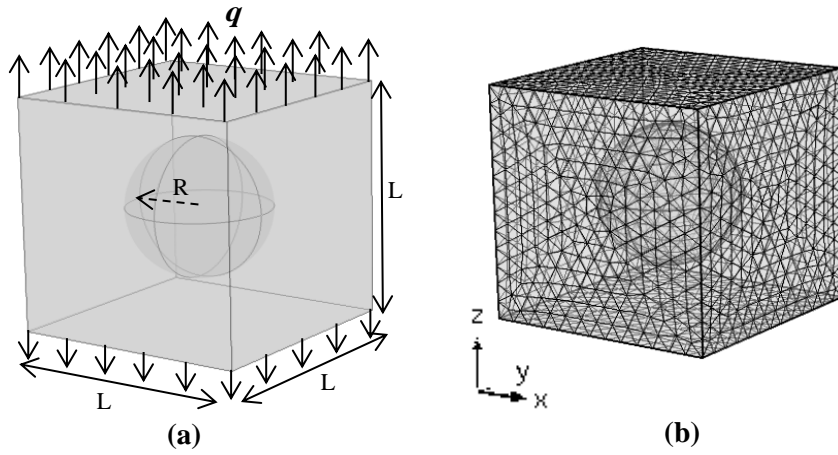


Fig.4.1: (a) Description of the physical problem, (b) Level-set within mesh.

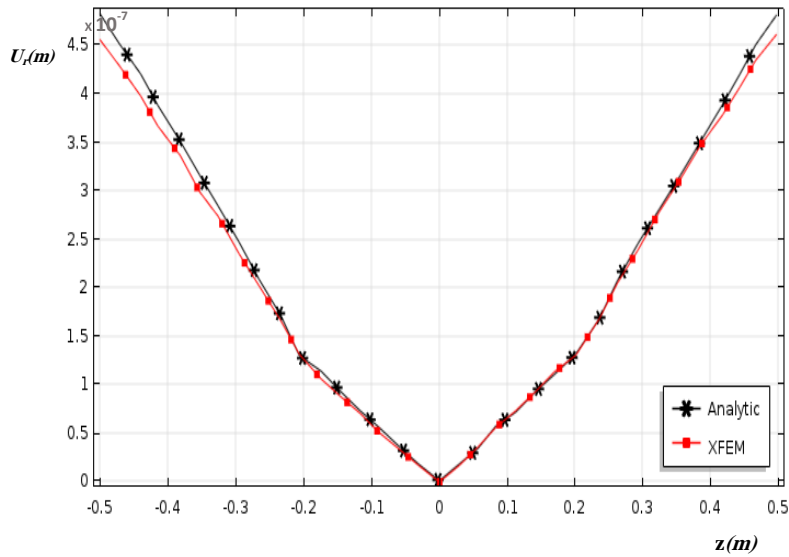


Fig.4.2: Evolution of the radial displacement U_r along the z -axis.

Figure 4.2 shows the evolution of the radial displacement component U_r at the z -axis, which is quasi-linear in each phase (matrix or inclusion) with continuity at the interface and a discontinuity of its gradient (strain), according to the adopted interface conditions. A good correlation between the obtained results and the analytical solution is observed.

4.1.2 Semi-circular surface crack in a cube under tension:

The second example concern an aluminium alloy cube containing an emergent semi-circular crack subjected to a tensile loading q along the z

direction, as shown in Figure 4.3. The dimensions and the mechanical properties are shown in the table 4.2. The aim of this example is to follow the evolution of displacement along the y-axis. The obtained results are regrouped in Figure 4.4.

Table 4.2: Mechanical properties and Geometrical characteristics for example

<i>Mechanical properties</i>	
E (Young's modulus of cube)	70 GPa
ν (Poisson's ratio of cube)	0.32
q (Static loading)	20 N/m ²
<i>Geometrical characteristics</i>	
L (Cube side)	1 m
r (Crack radius)	0.25 m

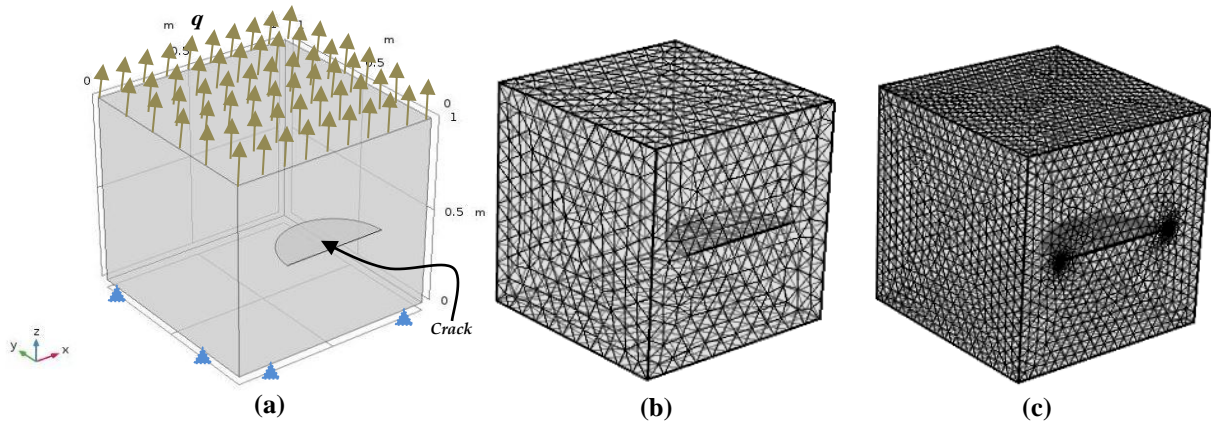


Fig.4.3: (a) Cube containing a semi-circular surface crack, (b) Level-set within mesh for XFEM, (c) Mesh for FEM.

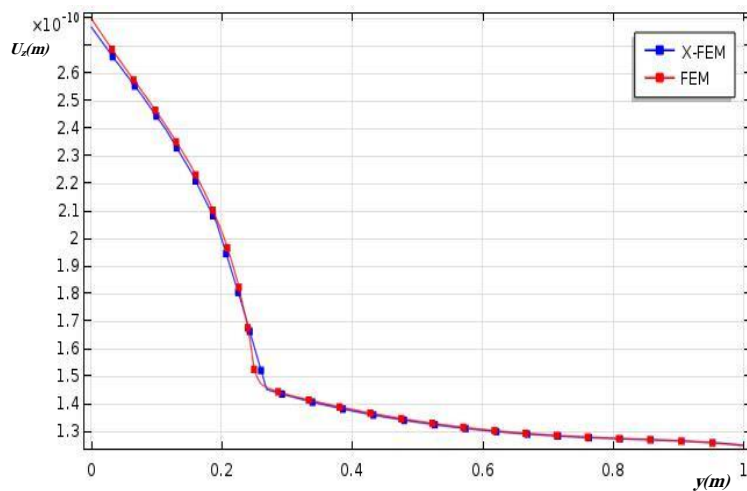


Fig.4.4: Evolution of displacement along the y-axis by X-FEM and FEM.

The comparison of the two results shows an excellent agreement between them, as shown in Figure 4.4. Thus, it gives a good judgment on the accuracy and robustness of our software. It is important to note that the emergent position of the crack has increased the displacement at the boundary level that contains the crack.

4.1.3 Crossing crack into cube under tension:

We consider the same mechanical properties and Geometrical characteristics in the table 4.2 but in this case with a Crossing crack. The obtained results are presented in the figure 4.6.

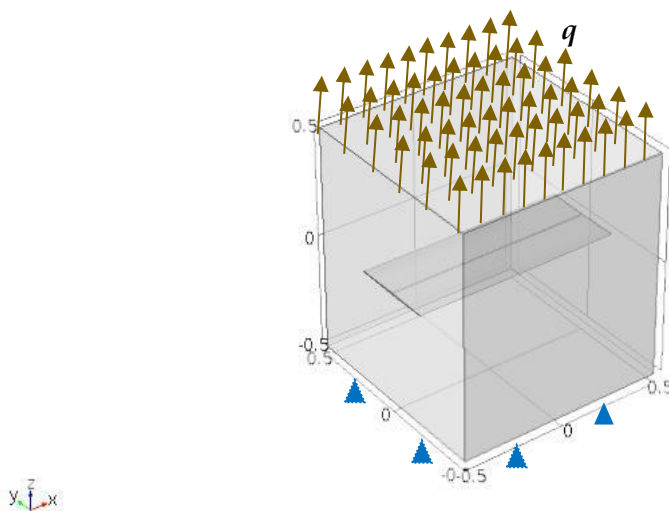


Fig 4.5: Cube containing a Crossing crack.

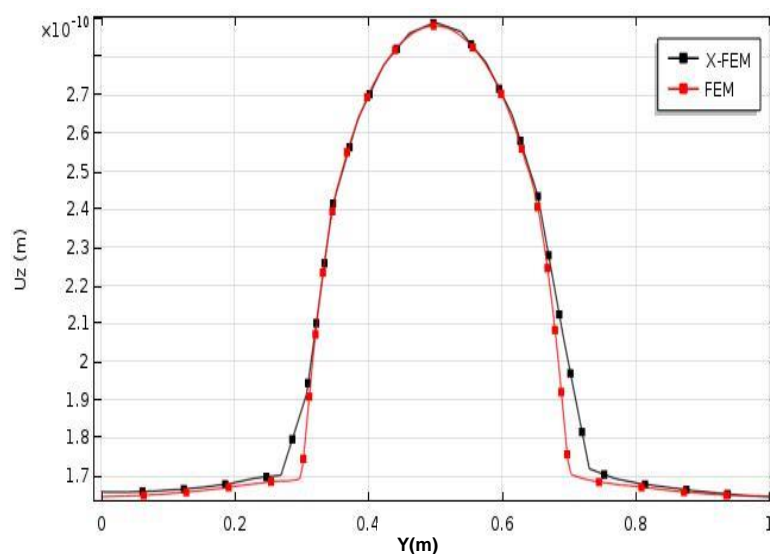


Fig 4.6: Evolution of displacement along the y -axis by X-FEM and FEM.

From Figure 4.6, a concordance between the results obtained by X-FEM and FEM is remarked; it also noticed that the maximum values of displacement are on the crack plan.

4.1.4 Annular surface crack into a cylinder under tension:

For the third validation example, an aluminium cylinder of geometrical dimensions $h = 1\text{m}$ and $R = 0.564\text{m}$ and the same mechanical properties of the previous example, which contains an annular crack, and subjected to a tensile loading q in the z direction, as shown in Figure 4.7. The obtained results give the variation of the displacement component U_z along the x -axis as presented in Figure 4.8. It is easily noticed that there is a good concordance between the two calculating tools. This testifies again to the efficiency of the developed code.

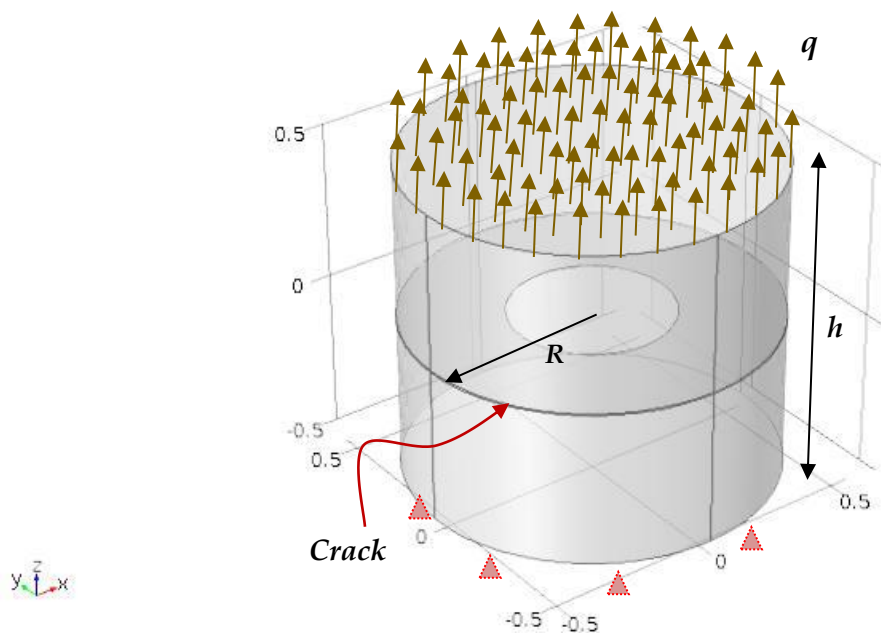


Fig.4.7: Cylinder containing an annular surface.

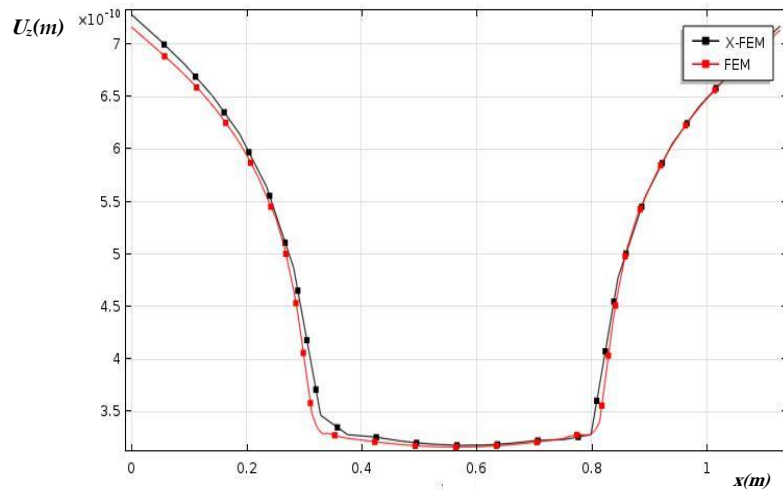


Fig.4.8: Evolution of displacement along the x-axis.

4.1.5 Elliptical crack forms into a cylinder under tension:

The geometry of this example is the same as the previous example with an elliptical crack of lower radius $R1 = 0.25m$ and upper radius $R2 = 0.5$ (figure 4.9). In this example, we are interested in the evolution of the displacement field at the level of the axes of the ellipse (major axis and minor axis). The obtained results are presented in figure 4.10 .

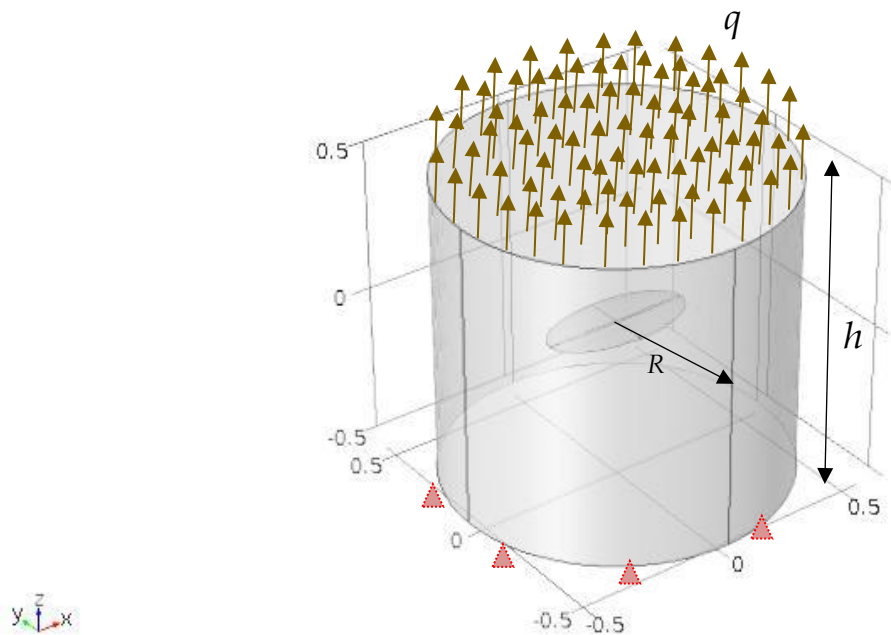


Fig. 4.9: Cylinder containing a crack in elliptical form subjected to a tensile loading.

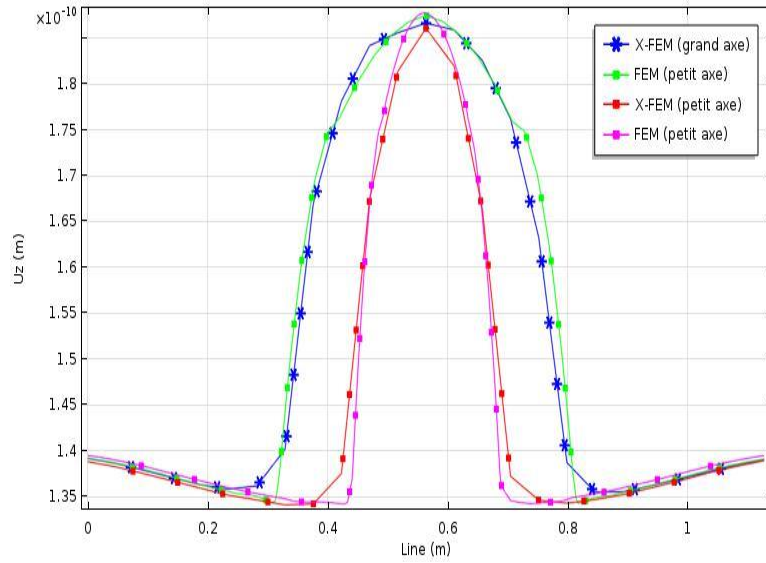


Fig. 4.10: Evolution of displacement along the y -axis by X-FEM and FEM.

From the results, we always notice the agreement between the results found with the two methods XFEM and FEM.

4.2 Parametric study for homogenization:

4.2.1 Flattened cylindrical void with respect to a crossing crack:

This example is concerned with a cube containing a flattened cylindrical void (of elliptical section), with a variable flattening rate a (small axis / major axis) and a constant surface fraction (major axis / cube side) $f = 0.4$, as shown in Figure 4.11. The matrix is in aluminium with the same mechanical properties of the table 4.2. We are interested to the evolution of the dimensionless compressibility modulus K_{ad} defined as $K_{ad} = K_{eff} / K_M$, with K_M is the compressibility modulus of the matrix and K_{eff} is the effective compressibility modulus of the composite.

The results presented in Figure 4.12 show an increase in dimensionless compressibility modulus K_{ad} with the increasing of the coefficient a followed by stabilization for large values to get a similarity with crack case. This augmentation is due to the decrease of the volume fraction in the zone of high values of a .

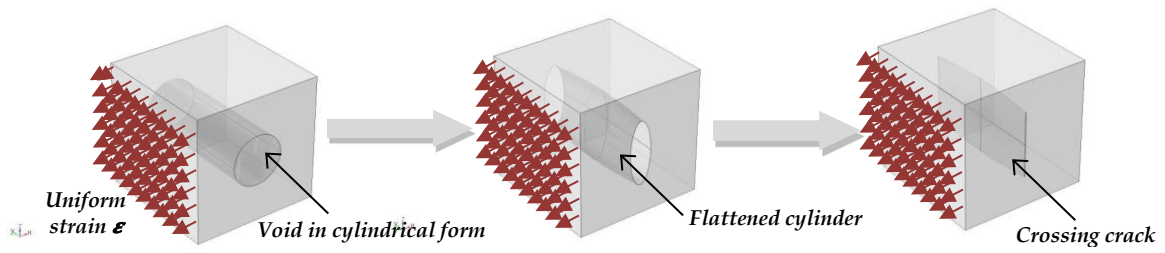


Fig.4.11: Flattening of a cylinder in a RVE.

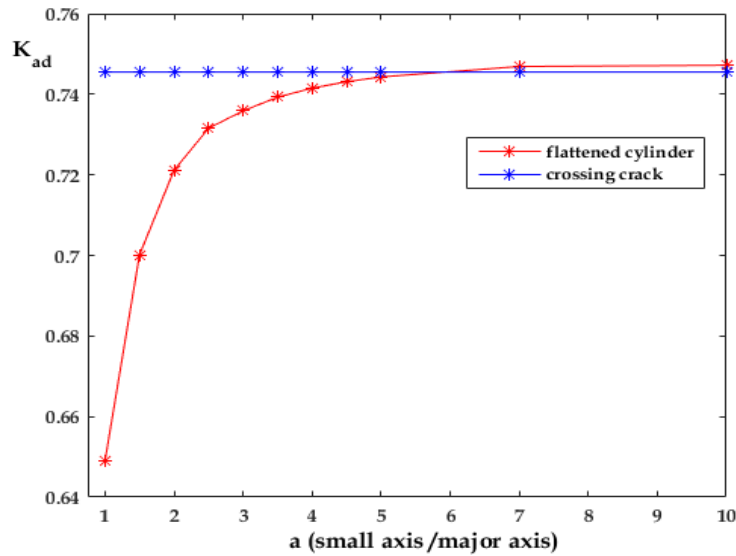


Fig.4.12: Evolution of K_{ad} of a flattened cylinder with respect to a crossing crack.

4.2.2 Flattened spherical void with respect to a circular crack:

In this example, the same cube of the previous example contains a flattened spherical void with respect to a circular crack, with a variable flattening rate a , and a constant surface fraction $f = 0.4$, as shown in Figure 4.13. We are interested to the evolution of K_{ad} versus a . The results are shown in Figure 4.14, in which the same remarks observed in the previous example are found.

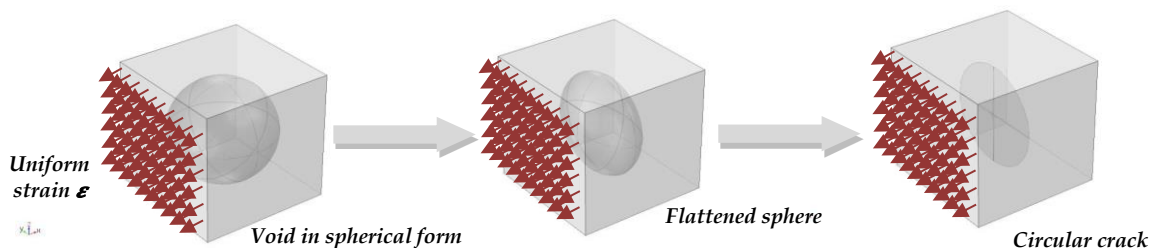


Fig.4.13: Flattening of a sphere in a RVE.

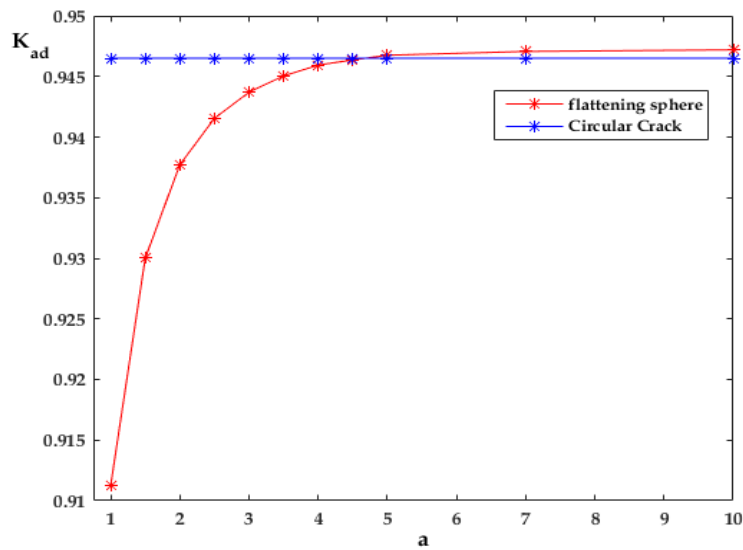


Fig.4.14: Evolution of K_{ad} of a flattening sphere with respect to a crack.

4.2.3 Influence of the size effect of the crack:

In this part, the effect of crack size on the K_{ad} coefficient is analysed. To do this, we assumed the case of a cube with similar proprieties as the previous example, where six (06) radius are tested $r(m) = \{0.4, 0.5, 0.6, 0.7, 0.8, 0.9\}$ of the supposedly circular crack (Figure.4.15).

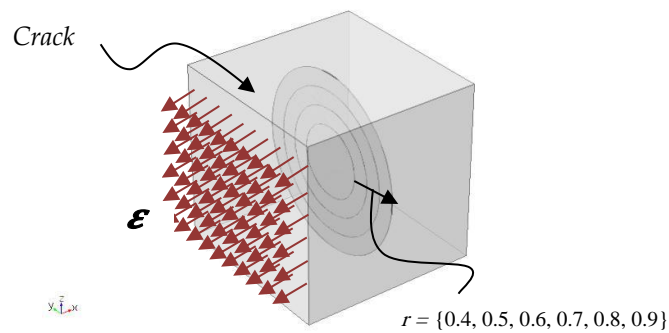


Fig.4.15: Geometry of the problem.

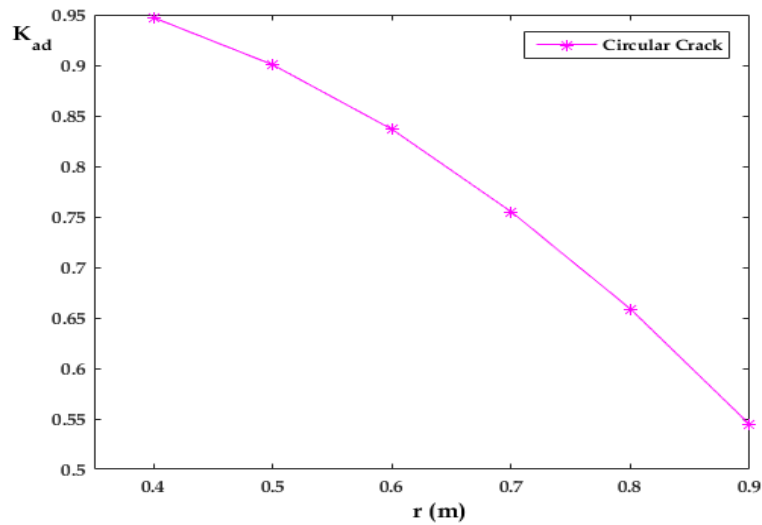


Fig.4.16: Evolution of K_{ad} versus the crack radius.

Figure 4.16 shows the evolution of K_{ad} as a function of the crack radius variation. It is noted that there is an inverse proportion between the dimensionless compressibility modulus and the size of the crack, because when the radius of the crack increases the K_{ad} decreases, that means that the crack affects negatively the rigidity of the structure, which is physically expected.

4.3 Conclusion:

Through the treated examples in this chapter, it has been shown that the X-FEM is able to treat the cracked structures in view of its concordance with the validation examples carried out. Under the context of a linear homogenization, the objective is to evaluate the effective parameter, in particular the effective compressibility modulus K_{eff} , for a Representative Elementary Volume (REV) containing voids and cracks, under the effect of a few parameters which addressed, the effect of the defect shape, its size and the effect of void flattening. This last effect concerns voids of two different forms (cylindrical and spherical), where it shows by accentuating more and more flattening, an effective behavior approaching to the crack of comparable size. This again testifies to the accuracy of this approach and the robustness of the developed code.

CHAPTER 5

Homogenization of nanocomposite materials with surface effect

CHAPTER 5

Homogenization of nanocomposite materials with surface effect

In this chapter we are interested in the problem of homogenization of medium containing heterogeneities (nanoinclusions, nanovoids and/or nano-cracks) with surface energy effects which is numerically addressed within Matlab® code, by XFEM/FEM combined with the Level-set technique, for various forms of nanoheterogeneities in a full 3D context. It is noted that this part of our study is considered as a generalization of a previous work of our research team limited to 2D framework carried out by Kired *et al.* [5]. The developed simulation tool is first validated by comparison with analytical and 2D numerical results from the literature, before being used to perform 3D numerical investigations accounting for the real 3D spherical and cylindrical shapes of the nanoheterogeneities in presence. The limit case of flattened or crack-like 3D nanovoids with surface energy compared to purely nano-cracks is also emphasized. Furthermore, the numerical simulations enable us to assess the slight effect of the adopted shape of the surrounding medium and the type of applied boundary conditions on the computed effective properties.

SUMMARY

5.1	Theoretical model	76
5.2	Flow chart of elaborated code with surface effect	82
5.3	Applications and numerical results	84
5.3.1	Cylindrical inclusion submitted to an Eigen-strai	84
5.3.3	Spherical void with coherent interface and different surrounding material shapes	96
5.3.4	Effect of flattening of nanovoids	99
5.3.4.1	Spherical void flattened to a penny shaped crack	99
5.3.4.2	Cylindrical void flattened to a through straight crack	102
5.3.4.3	Mesh refinement effect for flattening problem	105
5.4	Conclusion	106

5.1 Theoretical model:

In this section, the mathematical modeling of a multiphase medium (Figure. 5.1) with coherent interfaces is given in an elastic framework, in both strong and weak formulations.

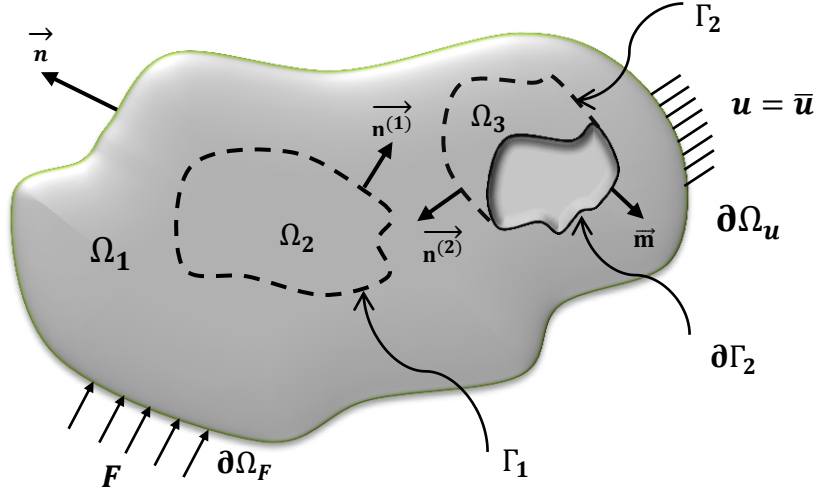


Fig.5.1: Multiphase domain with coherent open and close interfaces.

We consider an elastic 3D medium (Ω) composed of several isotropic phases ($\Omega^{(i)}$) separated by coherent interfaces Γ^i ($\Gamma = \cup \Gamma^i$) (see figure 5.1). This medium is in equilibrium under applied loading and kinetic constraints. The strong mathematical formulation of this problem utilizes the volume and surface equilibrium equations:

$$\mathbf{div}(\boldsymbol{\sigma}^{(i)}) + \mathbf{b} = \mathbf{0} \quad \text{in } \Omega^{(i)} \quad (5.1)$$

$$\mathbf{div}_s \boldsymbol{\sigma}^{(i)} \cdot \mathbf{s} = -\llbracket \mathbf{t} \rrbracket = (\boldsymbol{\sigma}^{(2)} - \boldsymbol{\sigma}^{(1)}) \mathbf{n}^{(1)} \quad \text{on } \Gamma^{(i)} \quad (5.2)$$

With the boundary conditions:

$$\begin{cases} \boldsymbol{\sigma} \cdot \mathbf{n} = -\mathbf{F} & \text{on } \partial\Omega_{\mathbf{F}} \\ \mathbf{u} = \bar{\mathbf{u}} & \text{on } \partial\Omega_{\mathbf{u}} \end{cases} \quad (5.3)$$

where $\partial\Omega_{\mathbf{F}} \cup \partial\Omega_{\mathbf{u}} = \partial\Omega$ et $\partial\Omega_{\mathbf{F}} \cap \partial\Omega_{\mathbf{u}} = \emptyset$

The interface equilibrium equation (Eq. 5.2) used here is the Laplace-Young model [1] for coherent interface where the traction vector \mathbf{t} is discontinuous (see equation (5.2)) and the displacement is continuous:

$$\mathbf{u}^{(2)} - \mathbf{u}^{(1)} = \llbracket \mathbf{u} \rrbracket = \mathbf{0} \text{ on } \Gamma^{(i)} \quad (5.4)$$

In equations (5.2) and (5.4), superscripts (5.2) and (5.1) refer to the two sides of the interface $\Gamma^{(i)}$. For more details about the Laplace-Young model and the modelling of interfaces, the reader can consult the references [51], [52].

The weak formulation reduce to finding the solution in displacement \mathbf{u} belonging to $\mathcal{D} = \{\mathbf{u} = \bar{\mathbf{u}} \text{ on } \partial\Omega_u, \mathbf{u} \in H^1(\Omega^{(i)})\}$, such as [5-6]:

$$\int_{\Omega^{(i)}} \boldsymbol{\sigma}^{(i)}(\mathbf{u}) : \boldsymbol{\epsilon}^{(i)}(\boldsymbol{\delta}\mathbf{u}) d\Omega + \int_{\Gamma^{(i)}} \boldsymbol{\sigma}^{(i)}(\mathbf{u}) \cdot \mathbf{n}^{(i)} \cdot \boldsymbol{\delta}\mathbf{u} d\Gamma - \int_{\Omega^{(i)}} \mathbf{b} \cdot \boldsymbol{\delta}\mathbf{u} d\Omega - \int_{\partial\Omega_F^{(i)}} \mathbf{F} \cdot \boldsymbol{\delta}\mathbf{u} dA = 0 \quad (5.5)$$

Knowing that $\boldsymbol{\delta}\mathbf{u} \in \{\boldsymbol{\delta}\mathbf{u} = \mathbf{0} \text{ on } \partial\Omega_u, \boldsymbol{\delta}\mathbf{u} \in H^1(\Omega^{(i)})\}$.

By projecting the second term of equation (5.5) on both sides of $\Gamma^{(i)}$, and invoking the Laplace-Young Model given by equation (5.2), it yields

$$\int_{\Gamma} \boldsymbol{\sigma}(\mathbf{u}) \cdot \mathbf{n} \cdot \boldsymbol{\delta}\mathbf{u} d\Gamma = \int_{\Gamma} (\boldsymbol{\sigma}^{(2)} - \boldsymbol{\sigma}^{(1)}) \mathbf{n}^{(1)} \cdot \boldsymbol{\delta}\mathbf{u} d\Gamma = \int_{\Gamma} \mathbf{div}_s(\boldsymbol{\sigma}_s) \cdot \boldsymbol{\delta}\mathbf{u} d\Gamma \quad (5.6)$$

Given that $\boldsymbol{\sigma}_s$ and $\boldsymbol{\delta}\mathbf{u}$ are continuously differentiable and the symmetry of $\boldsymbol{\sigma}_s$, we can use the divergence operator property

$$\begin{aligned} \mathbf{div}_s(\boldsymbol{\sigma}_s \cdot \boldsymbol{\delta}\mathbf{u}) &= \mathbf{div}_s(\boldsymbol{\sigma}_s^T) \cdot \boldsymbol{\delta}\mathbf{u} + \boldsymbol{\sigma}_s^T : \nabla_s(\boldsymbol{\delta}\mathbf{u}) \Rightarrow \\ \int_{\Gamma} \mathbf{div}_s(\boldsymbol{\sigma}_s) \cdot \boldsymbol{\delta}\mathbf{u} d\Gamma &= \int_{\Gamma} \mathbf{div}_s(\boldsymbol{\sigma}_s \cdot \boldsymbol{\delta}\mathbf{u}) d\Gamma - \int_{\Gamma} \boldsymbol{\sigma}_s : \nabla_s(\boldsymbol{\delta}\mathbf{u}) d\Gamma \end{aligned} \quad (5.7)$$

Let we define \mathbf{P} as the surface projection matrix in term of the unit normal \mathbf{n} at every point \mathbf{x} of Γ as:

$$\mathbf{P}(\mathbf{x}) = \mathbf{I} - \mathbf{n}(\mathbf{x}) \otimes \mathbf{n}(\mathbf{x}) \quad (5.8)$$

Thus, this symmetric matrix acts as the identity one for surface quantities, which allows us to write these equalities:

$$\mathbf{div}_s(\boldsymbol{\sigma}_s \cdot \boldsymbol{\delta}\mathbf{u}) = \mathbf{div}_s(\mathbf{P}\boldsymbol{\sigma}_s\mathbf{P}\boldsymbol{\delta}\mathbf{u}) = \mathbf{div}_s(\mathbf{P}\boldsymbol{\sigma}_s\boldsymbol{\delta}\mathbf{u}_s) = \mathbf{div}_s(\boldsymbol{\sigma}_s\boldsymbol{\delta}\mathbf{u}_s) \quad (5.9)$$

$$\begin{aligned}
 \boldsymbol{\sigma}_s : \nabla_s(\boldsymbol{\delta u}) &= (\mathbf{P}\boldsymbol{\sigma}_s\mathbf{P}) : (\nabla_s(\boldsymbol{\delta u})\mathbf{P}) = (\mathbf{P}\boldsymbol{\sigma}_s) : (\mathbf{P}\nabla_s(\boldsymbol{\delta u})\mathbf{P}) \\
 &= \boldsymbol{\sigma}_s : \frac{1}{2}[\mathbf{P}\nabla_s(\boldsymbol{\delta u})\mathbf{P} + (\mathbf{P}\nabla_s(\boldsymbol{\delta u})\mathbf{P})^T] = \boldsymbol{\sigma}_s : \boldsymbol{\epsilon}_s
 \end{aligned} \quad (5.10)$$

By applying the Stokes' theorem and the equation (5.9), the first integral of the right-hand of equation (5.7) is reduced by one dimension as follow [6],

$$\int_{\Gamma} \mathbf{div}_s(\boldsymbol{\sigma}_s\boldsymbol{\delta u})d\Gamma = \int_{\Gamma} \mathbf{div}_s(\boldsymbol{\sigma}_s\boldsymbol{\delta u}_s)d\Gamma = \int_{\partial\Gamma} \boldsymbol{\sigma}_s\mathbf{m} \cdot \boldsymbol{\delta u}_s dl = \int_{\partial\Gamma} \hat{\mathbf{F}} \cdot \boldsymbol{\delta u}_s dl = \int_{\partial\Gamma} \hat{\mathbf{F}} \cdot \mathbf{P}\boldsymbol{\delta u} dl \quad (5.11)$$

This integral only occurs when the interface Γ is open and an external force $\hat{\mathbf{F}}$ acts on its external boundary contour $\partial\Gamma$ of outward normal \mathbf{m} (see figure 5.1) otherwise it is equal to zero.

By using the equation (5.10) for the second integral of the right-hand of equation (5.7) and the equation (5.11), the weak formulation (5.5) becomes

$$\int_{\Omega} \boldsymbol{\sigma}(\mathbf{u}) : \boldsymbol{\epsilon}(\boldsymbol{\delta u})d\Omega + \int_{\Gamma_1} \boldsymbol{\sigma}_s(\mathbf{u}) : \boldsymbol{\epsilon}_s(\boldsymbol{\delta u})d\Gamma = \int_{\Omega} \mathbf{b} \cdot \boldsymbol{\delta u} d\Omega + \int_{\partial\Omega_F} \mathbf{F} \cdot \boldsymbol{\delta u} dA + \int_{\partial\Gamma} \hat{\mathbf{F}} \cdot \mathbf{P}\boldsymbol{\delta u} dl \quad (5.12)$$

Introducing the bulk and surface constitutive laws, one can write [5-6]:

$$\boldsymbol{\sigma}(\mathbf{u}) = \mathbb{C} : (\boldsymbol{\epsilon}(\mathbf{u}) - \boldsymbol{\epsilon}^*) \quad \text{on } \Omega, \text{ and } \boldsymbol{\sigma}^s = \boldsymbol{\sigma}_0 + \mathbb{C}^s : \boldsymbol{\epsilon}_s \quad \text{on } \Gamma, \quad (5.13)$$

\mathbb{C} and \mathbb{C}^s are the isotropic elastic fourth order tensors of the volume Ω (Union of all $\Omega^{(i)}$) and of surface/interface Γ (Union of all $\Gamma^{(i)}$) domains, respectively. The stress $\boldsymbol{\sigma}_0$ is such that $\boldsymbol{\sigma}_0 = \tau_0\mathbf{P}$ where τ_0 represents a residual surface tension at the interface, and $\boldsymbol{\epsilon}^*$ is the eigenstrain applied to Ω^* (as part of Ω). The components of \mathbb{C}^s are defined using the relation [6]:

$$\mathbb{C}_{ijkl}^s = \lambda_s P_{ij}P_{kl} + \mu_s (P_{ik}P_{jl} + P_{il}P_{jk}) \quad (5.14)$$

where λ_s and μ_s are the Lamé's constants of the interface/surface.

Introducing equations (5.13) into equation (5.12), the weak variational formulation is finally expressed as,

$$\int_{\Omega} \boldsymbol{\epsilon}(\boldsymbol{\delta u}) : \mathbb{C} : \boldsymbol{\epsilon}(\mathbf{u}) d\Omega + \int_{\Gamma_1} \mathbf{P}\boldsymbol{\epsilon}(\boldsymbol{\delta u})\mathbf{P} : \mathbb{C}^s : \mathbf{P}\boldsymbol{\epsilon}(\mathbf{u})\mathbf{P} d\Gamma = \int_{\Omega} \boldsymbol{\delta u} \cdot \mathbf{b} d\Omega + \int_{\partial\Omega_F} \boldsymbol{\delta u} \cdot \mathbf{F} dA + \int_{\partial\Gamma} \hat{\mathbf{F}} \cdot \mathbf{P}\boldsymbol{\delta u} d\Gamma + \int_{\Gamma_1} \mathbf{P}\boldsymbol{\epsilon}(\boldsymbol{\delta u})\mathbf{P} : \boldsymbol{\sigma}_0 d\Gamma + \int_{\Omega} \boldsymbol{\epsilon}(\boldsymbol{\delta u}) : \mathbb{C} : \boldsymbol{\epsilon}^* d\Omega \quad (5.15)$$

In the case where the surface energy is not considered, as in our previous study [54], all surface terms of the above equation vanish and the weak form of the problem is simplified to:

$$\int_{\Omega} \boldsymbol{\epsilon}(\boldsymbol{\delta u}) : \mathbb{C} : \boldsymbol{\epsilon}(\mathbf{u}) d\Omega = \int_{\Omega} \boldsymbol{\delta u} \cdot \mathbf{b} d\Omega + \int_{\partial\Omega_F} \boldsymbol{\delta u} \cdot \mathbf{F} dA + \int_{\Omega} \boldsymbol{\epsilon}(\boldsymbol{\delta u}) : \mathbb{C} : \boldsymbol{\epsilon}^* d\Omega \quad (5.16)$$

Substituting the displacement approximation of equations (5.20-5.22) in the variational form of equation (5.15), leads to the following system of linear algebraic equations:

$$(\mathbf{K} + \mathbf{K}_s)\mathbf{u} = \mathbf{f} \quad (5.25)$$

The global stiffness matrices \mathbf{K} and \mathbf{K}_s are composed of elementary matrices K_{IJ} and K_{IJ}^s related to the I^{th} and J^{th} nodes of the element (I and J varying from 1 to 4 for a tetrahedral linear element). They are expressed as:

$$K_{IJ} = \int_{\Omega} \mathbf{B}_I^T \mathbf{C}^{(i)} \mathbf{B}_J d\Omega \quad (5.26)$$

$$K_{IJ}^s = \int_{\Gamma} \mathbf{B}_I^T \mathbf{M}_p^T \mathbf{C}^s \mathbf{M}_p \mathbf{B}_J d\Gamma \quad (5.27)$$

From equation (5.15), the global force vector is given by:

$$\mathbf{f} = \int_{\Omega} \mathbf{N}^T \mathbf{b} d\Omega + \int_{\partial\Omega_F} \mathbf{N}^T \mathbf{F} dA + \int_{\Omega} \mathbf{B}^T \mathbf{C}^{(i)} \boldsymbol{\epsilon}^* d\Omega + \int_{\partial\Gamma} \mathbf{N}^T \mathbf{P}\hat{\mathbf{F}} d\Gamma + \int_{\Gamma_1} \mathbf{B}^T \mathbf{M}_p^T \boldsymbol{\sigma}_0 d\Gamma \quad (5.28)$$

Based on Voigt notation, we can write:

$$\mathbf{C}^{(i)} = \begin{bmatrix} (\lambda^{(i)} + 2\mu^{(i)}) & \lambda^{(i)} & \lambda^{(i)} & 0 & 0 & 0 \\ \lambda^{(i)} & (\lambda^{(i)} + 2\mu^{(i)}) & \lambda^{(i)} & 0 & 0 & 0 \\ \lambda^{(i)} & \lambda^{(i)} & (\lambda^{(i)} + 2\mu^{(i)}) & 0 & 0 & 0 \\ 0 & 0 & 0 & \mu^{(i)} & 0 & 0 \\ 0 & 0 & 0 & 0 & \mu^{(i)} & 0 \\ 0 & 0 & 0 & 0 & 0 & \mu^{(i)} \end{bmatrix} \quad (5.29)$$

$\lambda^{(i)}$ and $\mu^{(i)}$ are the bulk Lamé's constants of the isotropic i^{th} phase of the composite. Strain and stress tensors can be also write as vectors:

$$\boldsymbol{\epsilon} = [\epsilon_{11} \quad \epsilon_{22} \quad \epsilon_{33} \quad 2\epsilon_{12} \quad 2\epsilon_{23} \quad 2\epsilon_{13}]^T, \quad \boldsymbol{\sigma} = [\sigma_{11} \quad \sigma_{22} \quad \sigma_{33} \quad \sigma_{12} \quad \sigma_{23} \quad \sigma_{13}]^T \quad (5.30)$$

Knowing that \mathbf{C}^S is symmetric and based on equation (5.14), one can write [11]:

$$\begin{aligned} C_{11}^S &= (\lambda_s + 2\mu_s)P_{11}P_{11}; & C_{12}^S &= \lambda_s P_{11}P_{22} + 2\mu_s P_{12}P_{12}; & C_{13}^S &= \lambda_s P_{11}P_{33} + 2\mu_s P_{13}P_{13}; \\ C_{14}^S &= (\lambda_s + 2\mu_s)P_{11}P_{12}; & C_{15}^S &= \lambda_s P_{11}P_{23} + 2\mu_s P_{12}P_{13}; & C_{16}^S &= (\lambda_s + 2\mu_s)P_{11}P_{13}; \\ C_{22}^S &= (\lambda_s + 2\mu_s)P_{22}P_{22}; & C_{23}^S &= \lambda_s P_{22}P_{33} + 2\mu_s P_{23}P_{23}; & C_{24}^S &= (\lambda_s + 2\mu_s)P_{22}P_{12}; \\ C_{25}^S &= (\lambda_s + 2\mu_s)P_{22}P_{23}; & C_{26}^S &= \lambda_s P_{22}P_{13} + 2\mu_s P_{12}P_{23}; & C_{33}^S &= (\lambda_s + 2\mu_s)P_{33}P_{33}; \\ C_{34}^S &= \lambda_s P_{12}P_{33} + 2\mu_s P_{13}P_{23}; & C_{35}^S &= (\lambda_s + 2\mu_s)P_{33}P_{23}; & C_{36}^S &= (\lambda_s + 2\mu_s)P_{33}P_{13}; \\ C_{44}^S &= \lambda_s P_{12}P_{12} + \mu_s (P_{11}P_{22} + P_{12}P_{12}); & C_{45}^S &= \lambda_s P_{12}P_{23} + \mu_s (P_{12}P_{23} + P_{22}P_{13}); \\ C_{46}^S &= \lambda_s P_{12}P_{13} + \mu_s (P_{11}P_{23} + P_{12}P_{13}); & C_{55}^S &= \lambda_s P_{23}P_{23} + \mu_s (P_{22}P_{33} + P_{23}P_{23}); \\ C_{56}^S &= \lambda_s P_{13}P_{23} + \mu_s (P_{12}P_{33} + P_{13}P_{23}); & C_{66}^S &= \lambda_s P_{13}P_{13} + \mu_s (P_{11}P_{33} + P_{13}P_{13}); \end{aligned} \quad (5.31)$$

The \mathbf{M}_p Matrix is given by:

$$\mathbf{M}_p = \begin{bmatrix} P_{11}P_{11} & P_{12}P_{12} & P_{13}P_{13} & P_{11}P_{12} & P_{12}P_{13} & P_{11}P_{13} \\ P_{12}P_{12} & P_{22}P_{22} & P_{23}P_{23} & P_{12}P_{22} & P_{22}P_{23} & P_{12}P_{23} \\ P_{13}P_{13} & P_{23}P_{23} & P_{33}P_{33} & P_{13}P_{23} & P_{23}P_{33} & P_{13}P_{33} \\ 2P_{11}P_{12} & 2P_{12}P_{22} & 2P_{13}P_{23} & P_{12}P_{12} + P_{11}P_{22} & P_{22}P_{13} + P_{12}P_{23} & P_{12}P_{13} + P_{11}P_{23} \\ 2P_{12}P_{13} & 2P_{22}P_{23} & 2P_{23}P_{33} & P_{23}P_{23} + P_{22}P_{33} & P_{13}P_{23} + P_{12}P_{33} & P_{13}P_{23} + P_{12}P_{33} \\ 2P_{11}P_{13} & 2P_{12}P_{23} & 2P_{13}P_{33} & P_{12}P_{13} + P_{11}P_{23} & P_{13}P_{23} + P_{12}P_{33} & P_{13}P_{13} + P_{11}P_{33} \end{bmatrix} \quad (5.32)$$

The matrix \mathbf{B} is given in the case of a not-cut element by its conventional form:

$$\mathbf{B}_I = \begin{bmatrix} \frac{\partial N_I}{\partial x_1} & 0 & 0 \\ 0 & \frac{\partial N_I}{\partial x_2} & 0 \\ 0 & 0 & \frac{\partial N_I}{\partial x_3} \\ \frac{\partial N_I}{\partial x_2} & \frac{\partial N_I}{\partial x_1} & 0 \\ 0 & \frac{\partial N_I}{\partial x_3} & \frac{\partial N_I}{\partial x_2} \\ \frac{\partial N_I}{\partial x_3} & 0 & \frac{\partial N_I}{\partial x_1} \end{bmatrix} \quad (5.33)$$

For non-cut linear tetrahedral element, the shape functions N_I are linear, of the form $\frac{1}{6V}(\alpha_I + \beta_I x_1 + \gamma_I x_2 + \delta_I x_3)$, for which the derivatives and therefore the different components of the matrix \mathbf{B} are constant. V is the element volume and the coefficients α , β , γ and δ are dependent of the coordinates of the element vertices. This allows to evaluate analytically all volume integrals (on Ω or Ω_i) given by equations (5.26-5.27).

This conventional matrix \mathbf{B} will also be used for all elements cut by a void since the displacement is not enriched in this case. Moreover, the volume integrals will be evaluated numerically using 8 Gauss points for each sub-tetrahedron situated outside the void. However, for elements cut by inclusion, the matrix \mathbf{B} is completed by other columns corresponding to the additional displacement DOFs (see equation (5.20)):

$$\mathbf{B}_I = \begin{bmatrix} \frac{\partial N_I}{\partial x_1} & 0 & 0 & \frac{\partial \hat{N}_I}{\partial x_1} & 0 & 0 \\ 0 & \frac{\partial N_I}{\partial x_2} & 0 & 0 & \frac{\partial \hat{N}_I}{\partial x_2} & 0 \\ 0 & 0 & \frac{\partial N_I}{\partial x_3} & 0 & 0 & \frac{\partial \hat{N}_I}{\partial x_3} \\ \frac{\partial N_I}{\partial x_2} & \frac{\partial N_I}{\partial x_1} & 0 & \frac{\partial \hat{N}_I}{\partial x_2} & \frac{\partial \hat{N}_I}{\partial x_1} & 0 \\ 0 & \frac{\partial N_I}{\partial x_3} & \frac{\partial N_I}{\partial x_2} & 0 & \frac{\partial \hat{N}_I}{\partial x_3} & \frac{\partial \hat{N}_I}{\partial x_2} \\ \frac{\partial N_I}{\partial x_3} & 0 & \frac{\partial N_I}{\partial x_1} & \frac{\partial \hat{N}_I}{\partial x_3} & 0 & \frac{\partial \hat{N}_I}{\partial x_1} \end{bmatrix} \quad (5.34)$$

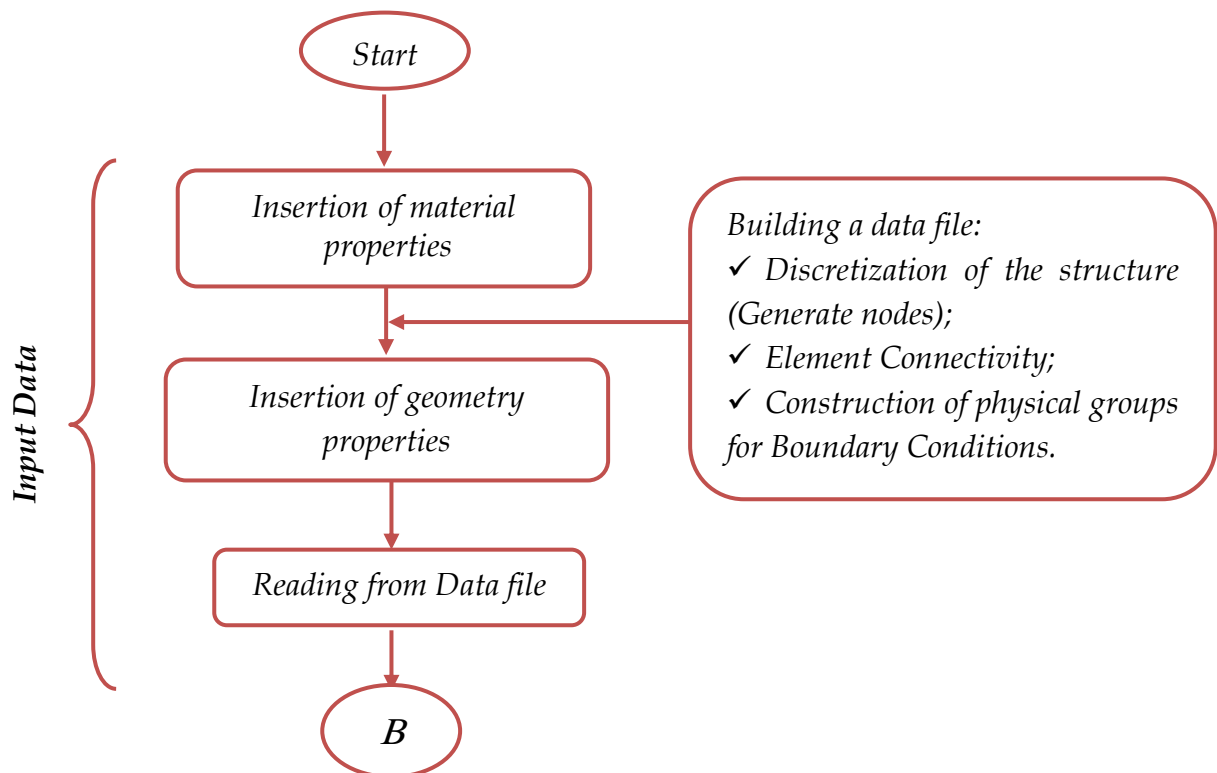
With $\hat{N}_I = \psi N_I$

In this case, the volume integrals are evaluated numerically using 8 gauss points for each sub-tetrahedron. The material associated with each gauss point x is assigned according to the sign of the discrete Level-Set function obtained by linear interpolation: $\phi(x) = \sum N_i \phi_i$.

For the surface integrals given by equations (5.27-5.28) which concern only the elements cut by the interface, evaluated on the surfaces surrounded by red dotted line in figure 5.2, the matrix B of equation (5.33) is used, since at the interface $\phi = 0 \Rightarrow \psi = 0$ in equation (5.22). This cancels the enrichment on the additional degree of freedom given by the second term of the displacement field expressed by equation (5.20). The additional stiffness terms in this case concern only the contribution of the surface integrals and correspond to the conventional degrees of freedom. As for the volume integrals for a non-cut element, the surface integrals are analytically evaluated.

5.2 Flowchart of elaborated code with surface effect:

In this part we introduce the flowchart of elaborated code with surface effect.



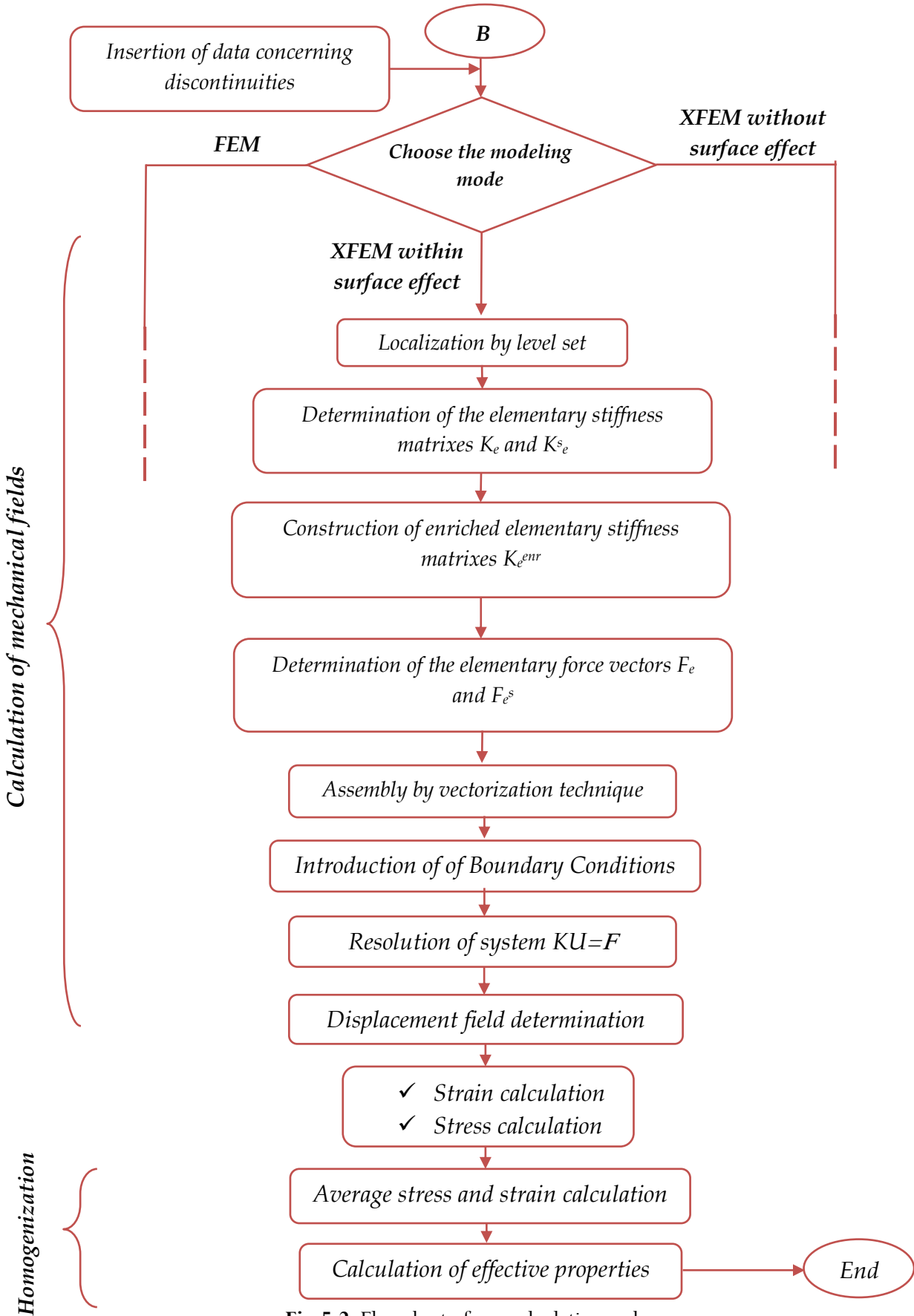


Fig 5.2: Flowchart of our calculation code.

5.3 Applications and numerical results:

In this section, various examples are treated in order to validate the developed 3D code, and to show its merits compared to 2D works, by comparison of the obtained results with those of literature. Numerical convergence tests are also performed so as to find the right mesh density, and to assess the stability of the numerical procedure. Assuming that for all treated examples both the residual surface tension and the applied load on the external interface boundaries are null ($\tau_0 = 0, \hat{\mathbf{F}} = 0$).

5.3.1 Cylindrical inclusion submitted to an Eigen-strain:

In this application, a cylindrical inclusion subjected to an Eigen-strain ϵ^* is embedded in an infinite medium, for which the interface between both phases being an imperfect coherent one. As the analytical solution is available for this problem, it provides a validation test regarding the evaluation of the size effect of nano-heterogeneity and the influence of the surface energy. It allows also to assess the effect of the longitudinal dimension on the predicted values since the analytical solution was developed in a plane strain framework. Finally, a convergence analysis of the implemented approach is proposed here.

The exact analytical solution of the strain and displacement fields was given by Sharma et al. [55]:

$$\epsilon_{rr}(\mathbf{r}) = \epsilon_{\theta\theta}(r) = A, \quad 0 \leq r \leq R_0 \quad (5.35)$$

$$\begin{cases} \epsilon_{rr}(\mathbf{r}) = -A \frac{R_0^2}{r^2} \\ \epsilon_{\theta\theta}(\mathbf{r}) = +A \frac{R_0^2}{r^2} \end{cases}, \quad r \geq R_0 \quad (5.36)$$

$$\mathbf{u}_r(\mathbf{r}) = \begin{cases} Ar, & 0 \leq r \leq R_0 \\ A \frac{R_0^2}{r}, & r \geq R_0 \end{cases} \quad (5.37)$$

with

$$\mathbf{A} = \frac{3K^M \epsilon^* - \tau_0/R_0}{2\mu^M + 3K^M + K^S/R_0} \quad (5.38)$$

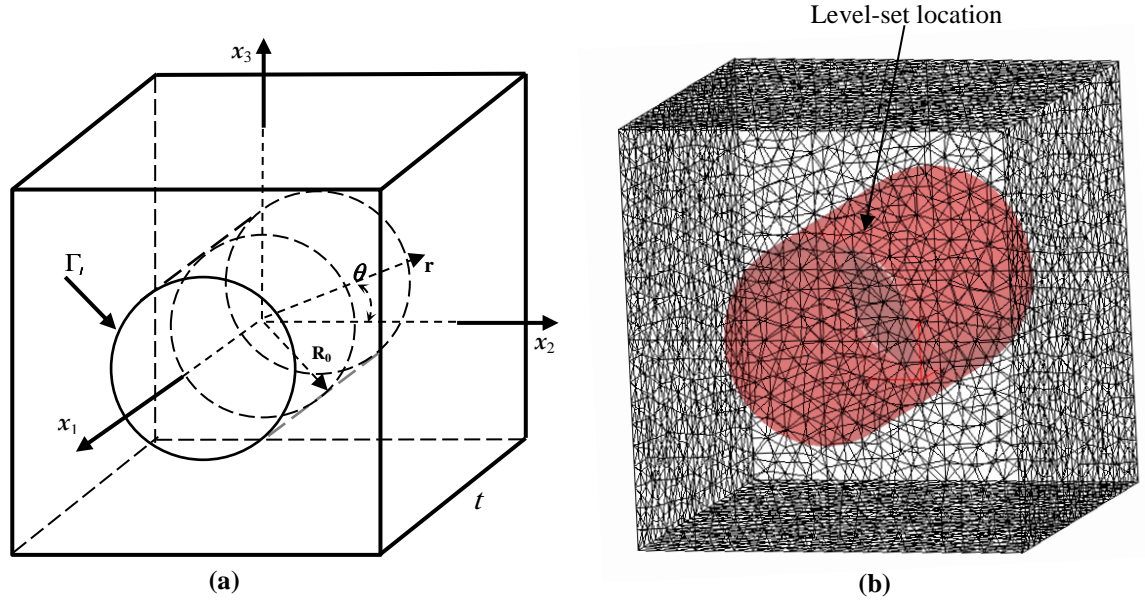


Fig.5.3: Cylindrical fiber into cubic matrix: a) Geometrical configuration; b) Level-set crossing the mesh.

In the former expressions, R_0 is the radius of the cylinder, $K'^M = 2(\lambda^M + \mu^M) / 3 = (C_{11} + C_{12}) / 3$ and $K'_s = (\lambda^S + 2\mu^S)$ are the bulk and the surface elastic moduli of the matrix and the interface, respectively, and $\epsilon^* = \epsilon_{22}^* = \epsilon_{33}^*$, $\epsilon_{11}^* = \epsilon_{12}^* = \epsilon_{23}^* = \epsilon_{13}^* = 0$ are the components of the ϵ^* tensor. In order to model this problem, a finite matrix cube enveloping the inclusion is considered (see figure 5.3), on which displacement boundary conditions are imposed according to the exact solution given by equation (5.37), to simulate an infinite medium.

The mechanical properties of the matrix and the fiber are identical, and equal to those of aluminum alloy $E=3MPa$ and $\nu = 0.3$. Regarding the interface parameters, three situations are considered according to atomic arrangement of aluminum: K'_s positive, negative or null. The surface parameters used, obtained by Miller et Shenoy [2] are listed in table 5.1.

Table 5.1: Surface elastic constants

Surface	λ_s	μ_s	K'_s
Al[111]	6.842 N/m	-0.375 N/m	12.932
Al[100]	3.48912 N/m	-6.2178 N/m	-5.457

In order to quantify the size effect due to the nanofiber as the contribution of the surface energy E_s to the total energy (the sum of surface energy E_s and bulk energy E_b), an indicator β , proposed by Yvonnet et al. [6], is calculated versus the radius R_0 . This indicator is defined as:

$$\beta = \frac{|E_s|}{|E_s| + |E_b|} \quad (5.39)$$

It can be evaluated numerically in two ways:

$$\beta = \frac{\left| \int_{\Gamma_1} \sigma_s(\mathbf{u}) : \epsilon_s(\mathbf{u}) d\Gamma \right|}{\left| \int_{\Gamma_1} \sigma_s(\mathbf{u}) : \epsilon_s(\mathbf{u}) d\Gamma \right| + \left| \int_{\Omega} \sigma(\mathbf{u}) : \epsilon(\mathbf{u}) d\Omega \right|} \quad (5.40)$$

$$\beta = \frac{|\mathbf{u} \mathbf{K}_s \mathbf{u}|}{|\mathbf{u} \mathbf{K}_s \mathbf{u}| + |\mathbf{u} \mathbf{K} \mathbf{u}|} \quad (5.41)$$

In this study, the second expression is adopted as it didn't require to evaluate stresses and strains. This expression is also be useful for defining a semi-analytic evaluation of β using the analytic expression of the vector \mathbf{u} given by equation (5.37) coupled with matrices \mathbf{K}_s and \mathbf{K} obtained numerically:

$$\beta_{\text{Semi-analy}} = \frac{|\mathbf{u}_{\text{analy}} \mathbf{K}_s \mathbf{u}_{\text{analy}}|}{|\mathbf{u}_{\text{analy}} \mathbf{K}_s \mathbf{u}_{\text{analy}}| + |\mathbf{u}_{\text{analy}} \mathbf{K} \mathbf{u}_{\text{analy}}|} \quad (5.42)$$

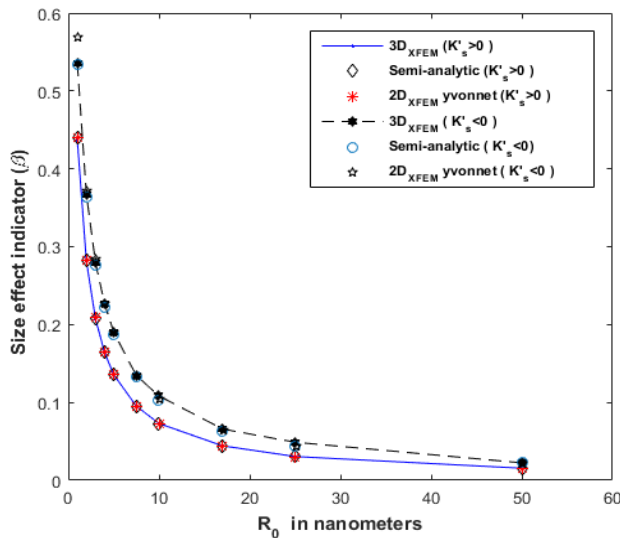


Fig.5.4: Indicator β versus fiber size.

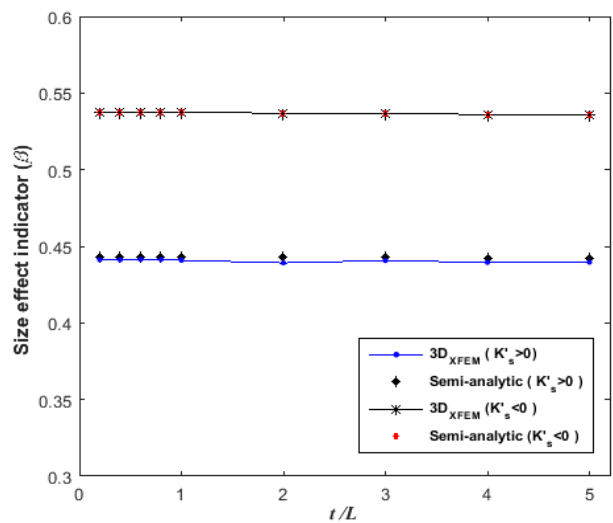


Fig.5.5: Indicator β versus thickness.

The obtained results, with a volume fraction $f=0.2$ are confronted to the semi-analytical solution as well as the solutions obtained by Yvonnet et al. [6] treating this problem in 2D plane strain context. As the energetic indicator β is of quadratic dependence to displacement (see equations 5.40 - 5.41), only low mesh density of $35 \times 35 \times 35$ nodes are needed to get accurate results as shown in figure 5.4, proving the effectiveness of the present approach.

The 3D nature of the developed code allows varying the thickness t of the matrix along the fiber axis, in order to assess the effect of the longitudinal dimension. Hence, β is evaluated for $R_0 = 1 \text{ nm}$ and $f = 0.2$ by varying the thickness from $L/5$ to $5L$ (L being the side of the cube). It comes from Figure 5.5 that there is no effect of the longitudinal dimension for the treated problem.

Based on the analytical solution, a convergence analysis is proposed in order to show the accuracy and the stability of the present approach and consequently the efficiency of the developed code for $R_0 = 2 \text{ nm}$ and $f = 0.2$. For this purpose, the relative energy norm error is evaluated by considering the analytical solution as the reference one as:

$$\mathbf{Er}_{\text{rel}} = \frac{\|E_{\text{tot}}^h - E_{\text{tot}}\|}{\|E_{\text{tot}}\|} = \frac{\sqrt{(\mathbf{u}^h - \mathbf{u}_{\text{analy}})(\mathbf{K}_s + \mathbf{K})(\mathbf{u}^h - \mathbf{u}_{\text{analy}})}}{\sqrt{\mathbf{u}_{\text{analy}}(\mathbf{K}_s + \mathbf{K})\mathbf{u}_{\text{analy}}}} \quad (5.43)$$

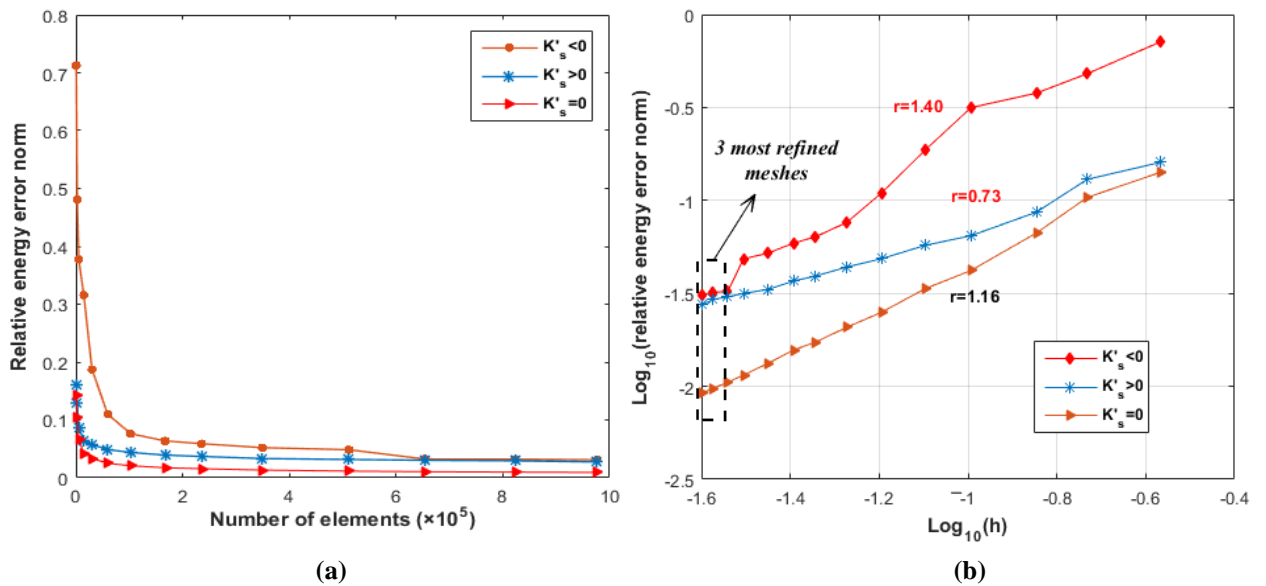


Fig.5.6: Relative energy error norm for the cylindrical inclusion problem: (a) versus number of elements; (b) versus the dimensionless mesh size

This error is first plotted versus the number of meshing elements in figure 5.6a. This figure shows that the error is stable and small (less than 1% for $K'_s = 0$ and less than 3% for $K'_s \neq 0$) from a refinement of approximately 700000 elements corresponding to approximately 120000 ($50 \times 50 \times 50$) nodes. Then, the error is plotted versus the element size $\bar{h} = h/L$ in a Log-Log representation in figure 5.5b. Based on its definition, the optimal convergence rate expected for relative error energy norm is $r = 1$ (in h^1). Figure 8b shows that for $K'_s = 0$ (in the absence of the surface effects), this expected value is approached in a stable way especially by refining the mesh ($r=1.16$ as an average value and $r=0.99$ for the first three points on its curve in figure 5.6b, corresponding to the most refined meshes). However for $K'_s > 0$, the solution converges within a non-optimal rate ($r=0.73$) but remains stable by refining the mesh (for the three most refined meshes, the rate still constant: $r=0.73$). Concerning $K'_s < 0$, the proposed approach leads also to a convergent solution without an optimal rate ($r=1.40$), but in a very unstable way in particular by refining the mesh ($r=0.30!!$ for the three most refined meshes).

From these findings, we can say that in the absence of the surface energy and despite the intervention of XFEM on the system of equations (5.34) by enriching the additional DOFs, the convergence rate optimality is very little affected and its value is very close to that of the conventional FEM, especially when meshes are refined. This result has also been obtained by [19] during its tests. This can be explained by the fact that in this case the discontinuity of material parameters within the bimaterial elements (those cut by the interface) is taken into account by the XFEM enrichment. Whereas with the presence of the surface energy ($K'_s > 0$ and $K'_s < 0$), the stiffness discontinuity caused by the interface parameters according to the stress jump given by the Laplace-Young model, is no longer taken into account, which considerably affects the optimality of convergence. Moreover, and contrary to the case $K'_s > 0$, the instability of convergence observed for the case $K'_s < 0$ is undoubtedly due to the addition of negative terms of surface stiffness to the diagonal elements of the global stiffness, thus affecting the diagonal dominance and therefore the conditioning of the system. This remark concerning the ill-conditioning of the system in the case of $K'_s < 0$ has also been mentioned by

both Gao et al. [66] using conventional FEM and Yvonnet et al. [6] using XFEM. This proves again that this issue appears to be due to the surface terms (especially when it is of negative sign) for which the XFEM enrichment is not active (see the last paragraph of section 3). Note that such situation is observed increase for example 5.4.4, which has led us to be limited to $K'_s = 0$ and $K'_s > 0$, despite the use of specific iterative solvers such as those recommended by [6-7] for this case, namely "the biconjugate gradients methods" (bicg and bicgstab under Matlab). It is worth also noting that a solution was sought in order to overcome the problem of ill-conditioning. Unfortunately, the only procedure we found in the literature, whose numerical implementation is relatively simple and efficient, deals with 2D domains such as in [56] where the Stable Generalized FEM was used.

5.3.2 Effective behavior of REV containing cylindrical void:

Several objectives are aimed through the study of the present example. As in the previous one, the validation of the proposed 3D approach is sought first by comparing the obtained results with the analytical solution and with other numerical results from the literature. Secondly, several parametric studies will be conducted concerning the effects of the nano-heterogeneity (nanovoid here) size, its volume fraction and its interface elastic parameters, on the effective stiffness in different directions (longitudinal and transversal), the longitudinal being parallel to the void axis. Finally, particular attention will be paid to the effective stiffness and the orthotropic rate of the nano-porous material, in two specific situations, namely below the nano-scale and by amplifying the surface elastic constants, where unexpected observations will be detected.

In this application, the same scheme of the previous example was adopted with a void instead of inclusion. The cube, now called REV in homogenization context, is subject to Periodic Boundary Conditions (PBC) along the x_2 axis (perpendicular to the void axis). This problem was also treated by Yvonnet et al. [6] in 2D with an aluminum alloy matrix whose mechanical properties are $E^M = 70GPa$ and $\nu^M = 0.32$. The surface elastic constants and the volume fraction are identical to those of Example 5.4.1. The obtained results by Quang and He

[43-44] analytically as well as those obtained by Yvonnet et al. [6] numerically will be used to validate the present work.

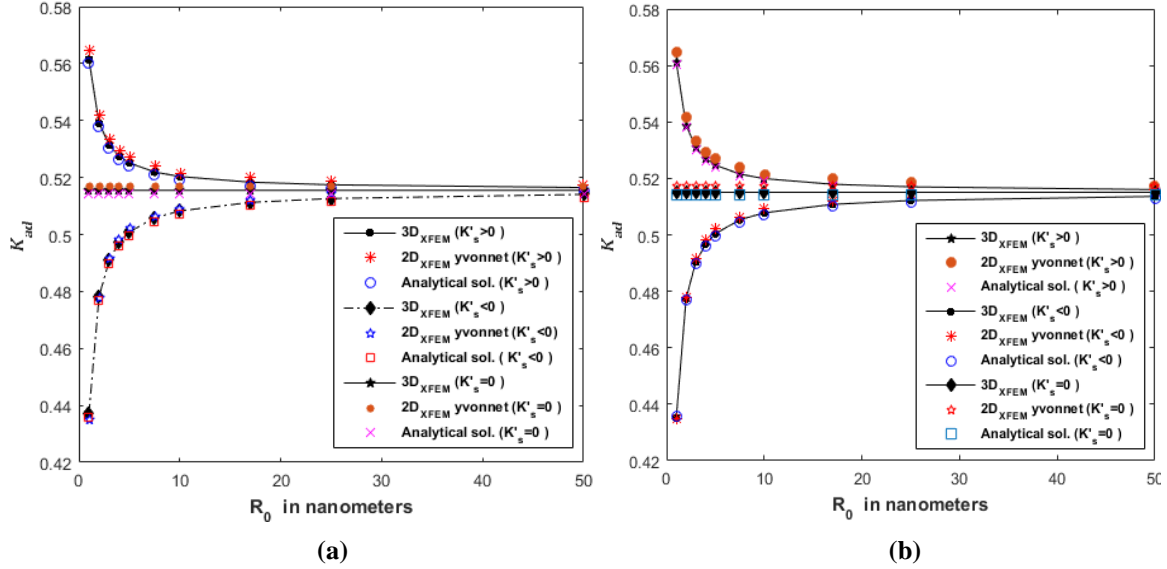


Fig.5.7: Dimensionless transverse bulk modulus versus void radius: **a)** with the first REV's configuration; **b)** with the second REV's configuration.

We are interested in evaluating the transverse effective bulk modulus, defined by [13] as $k^* = (C_{22} + C_{23})/2$, versus R_0 ranging from 1nm to 50nm. In the second stage, this same modulus is evaluated, by varying the volume fraction f from 0 to 0.6 for $R_0=1$ nm. All computations are made by considering both REV configurations (figure 2.3a and figure 2.3b) and a mesh density about $50 \times 50 \times 60$ nodes to evaluate the dimensionless transverse effective modulus $K_{ad} = k_{eff}^*/k_M^*$ because of its linear dependence to displacement. The different results are grouped in figures 5.7 and 5.8.

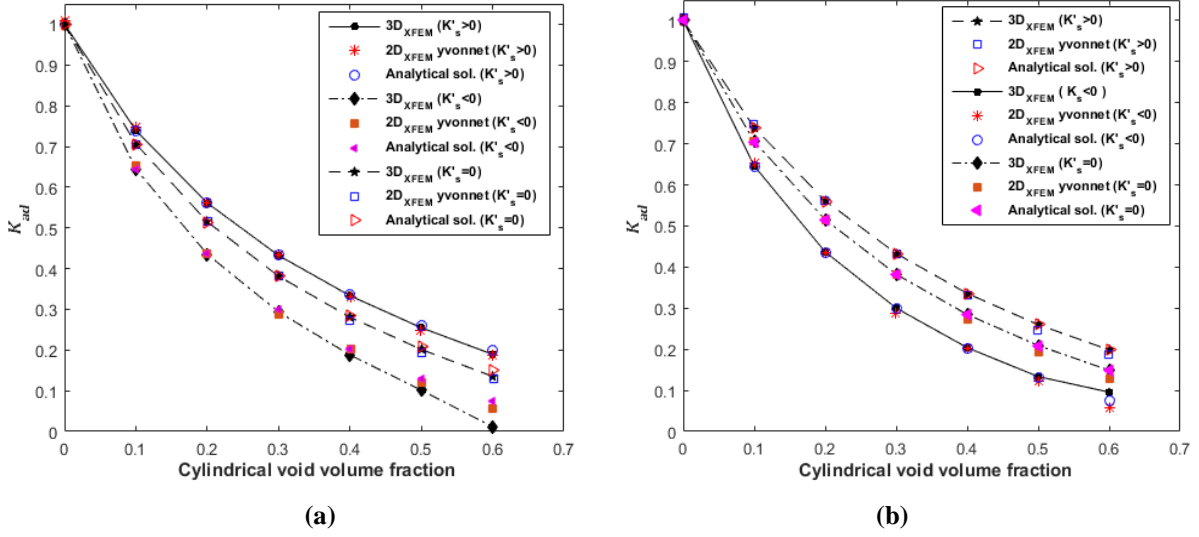


Fig.5.8: Dimensionless transverse bulk modulus with respect to volume fraction: **a)** with the first REV configuration; **b)** with the second REV configuration.

Figure 5.7 shows first that the effect of surface energy decreases with fiber size. The second observation concerns the good agreement between the different results. It is also noted that against the analytical solution, the 3D approach using the second configuration of the REV offers a slight improvement compared with other approximations including those of Yvonnet et al. [4]. The same remarks can be observed for figure 5.8 concerning the evolution of K_{ad} versus the volume fraction, which decreases when this latter increases.

The 3D aspect of the present study makes it possible to extend the analysis to the third dimension, namely stiffness along the void axis x_1 . For this purpose, the longitudinal effective modulus defined as $n^* = C_{11}$ is also quantified in dimensionless way by $n_{ad} = n_{eff}^*/n_M^*$. This parameter is given analytically by Quang and He [44]. The obtained results, by using the second configuration of REV, are shown in figure 5.9.

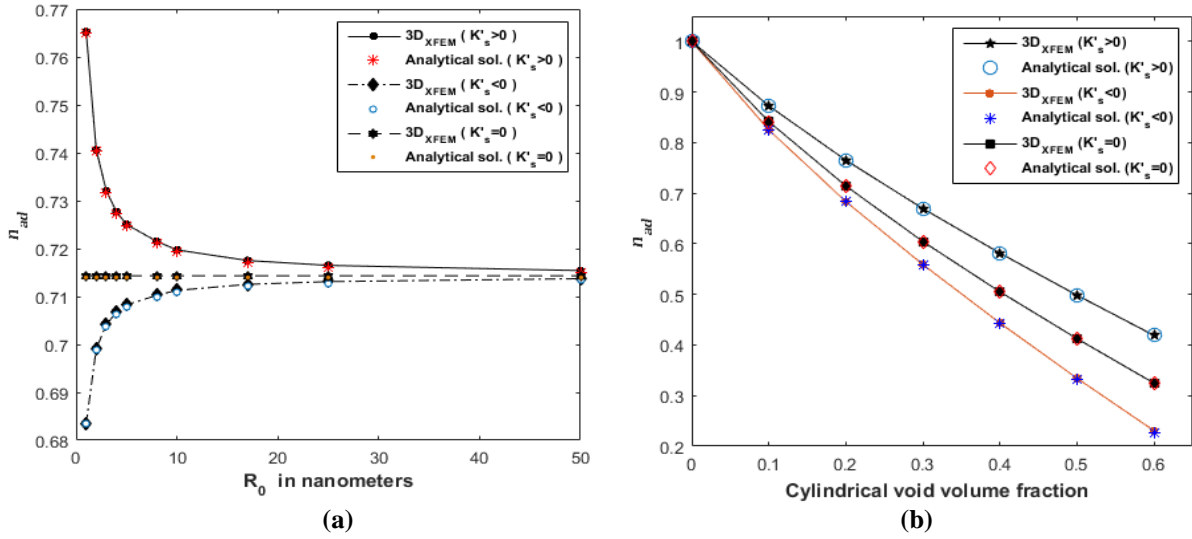


Fig.5.9: Dimensionless effective longitudinal bulk modulus: **a)** with respect to void size; **b)** with respect to volume fraction.

The agreement of the obtained results with the analytical solution is remarkable, thus testifying the quality of the results provided by the present numerical simulation tool. Like the K_{ad} parameter, n_{ad} is influenced by the surface energy, especially for the low values of R_0 .

We also observe that, regarding the curves corresponding to $K'_s > 0$, the evolution of both K_{ad} and n_{ad} has the tendency to reach the unit value. This means that the nanoporous medium is expected to be stiffer transversely and longitudinally than its matrix if R_0 decreases below 1 nm. The results of this theoretical test, for different volume fractions, are drawn in figure 5.10. These results show the existence of a critical value of $R_0 = 0.04$ nm for K_{ad} and $R_0 = 0.13$ nm for n_{ad} , below which the composite is stiffer than its parent material, and this for all values of the volume fraction.

Such results are very important from a technological point of view for the development of new materials that can be lighter and stiffer in the same time. However, the low values of R_0 may question the applicability of mathematical models based on solid mechanics theory (used here) for such near-atomic scales. This gives to these results rather a theoretical aspect. To avoid this kind of situation and to remain within the validity of the adopted models, one will not seek the gain in weight and in strength by size reduction but by proportional increase of the

impact of the surface energy. This is achieved by gradually amplifying the surface elastic constants of the interface. Note that a similar amplification procedure is also used in Chatzigeorgiou et al. [57] when predicting the effective behavior of nano composites analytically.

This test concerns an REV of $R_0 = 1 \text{ nm}$ with amplification of K'_s of the former case n times. The evolution of the parameters K_{ad} and n_{ad} versus the factor n is presented in figure 5.11a and 5.11b, respectively. These figures show, as expected, an increase of K_{ad} and n_{ad} by a factor n exceeding the unit value at approximately $n = 24$ for K_{ad} and $n = 8$ for n_{ad} for all values of volume fraction.

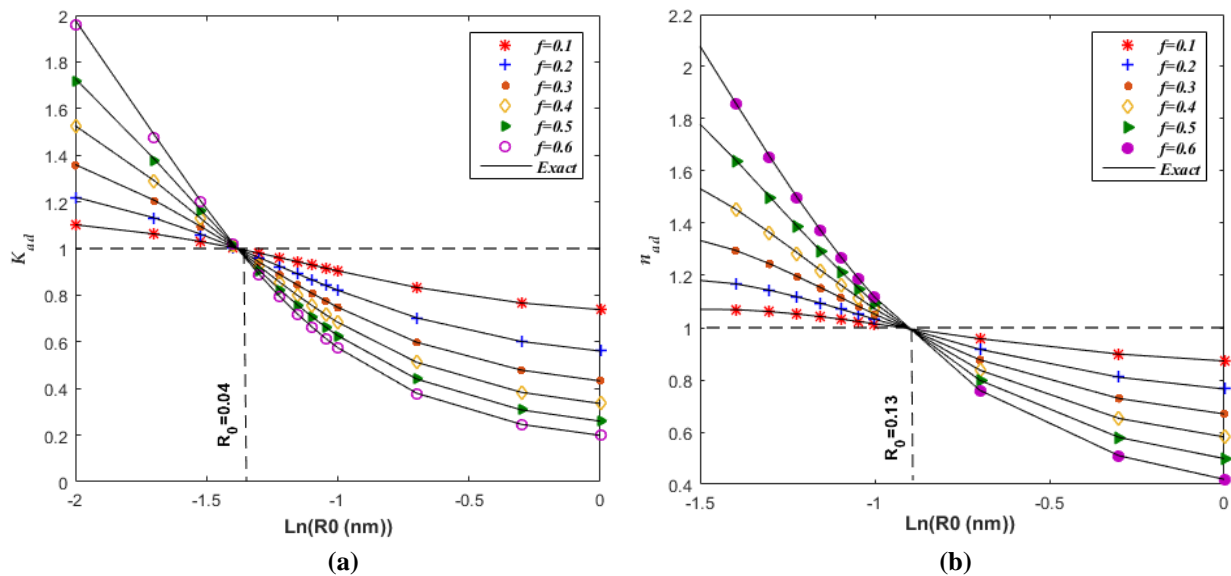


Fig.5.10: Dimensionless effective bulk moduli below nanoscale: **(a)** transverse modulus; **(b)** longitudinal modulus.

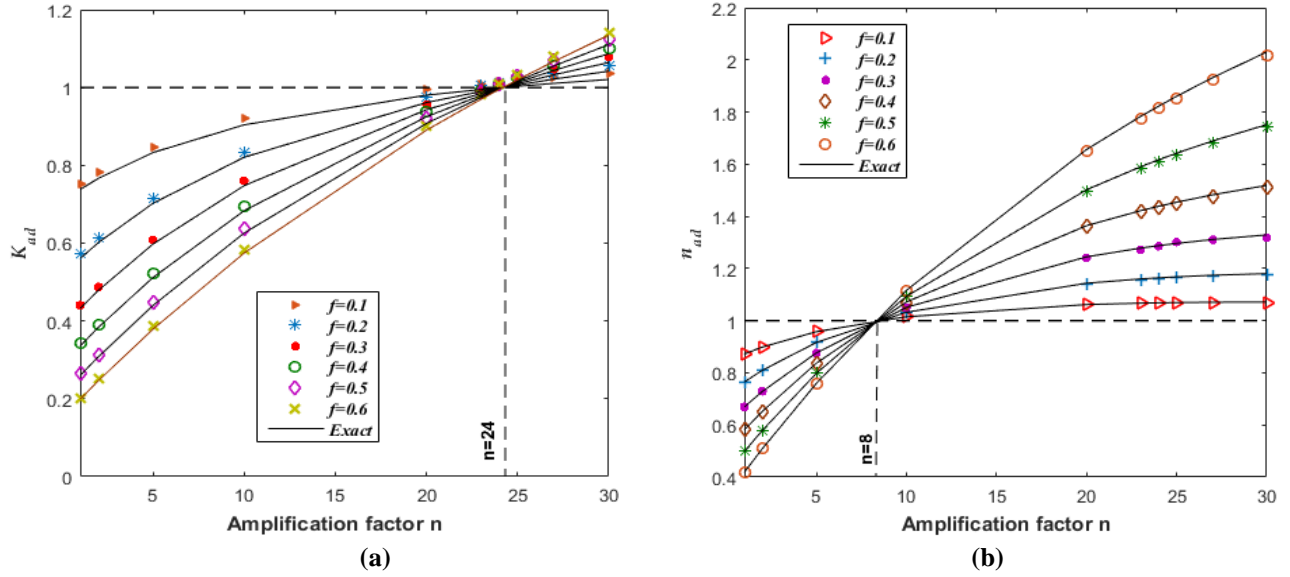


Fig.5.11: Dimensionless effective bulk moduli with amplifying surface characteristics: **(a)** transverse modulus; **(b)** longitudinal modulus

Note that other effective moduli given in [13] and engineering constants expressed by the relations (5.37) that can be evaluated with the present calculation tool have been omitted for the sake of brevity. However, special attention is paid to an important parameter characterizing the 3D behavior of this REV, namely the orthotropic ratio E_1/E_2 since $E_2=E_3$. This ratio is numerically evaluated as a function of R_0 and is displayed in figure 5.12. Like for all the quantities evaluated above, the orthotropic ratio is affected by the surface energy and has the tendency to reach the unit value for $K'_s > 0$, which may be called a pseudo-isotropy or quasi-isotropy ($E_1=E_2$) if R_0 decreases below 1nm. The results of this theoretical test are plotted in figure 5.12a. These results show a range of R_0 values corresponding to pseudo-isotropy ($E_1=E_2$). These values are between $0.038nm$ and $0.076nm$ depending on the volume fraction varying between 0.1 and 0.6 .

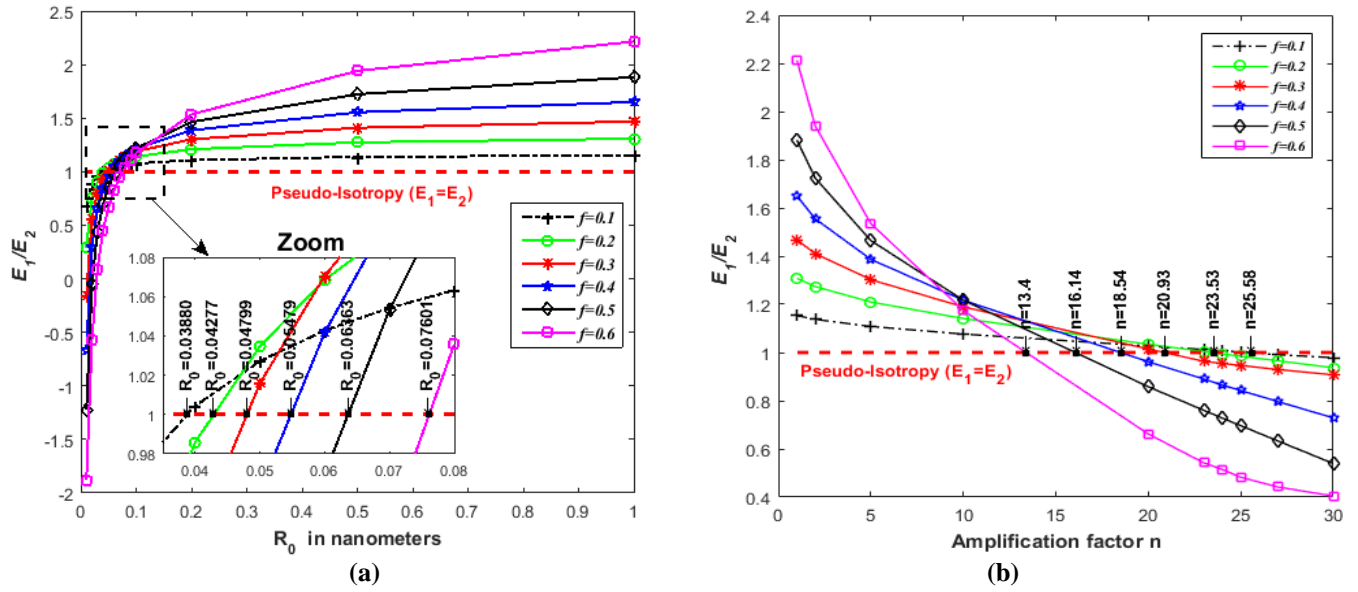


Fig.5.12: Orthotropic ratio for theoretical situations: **(a)** below nanoscale; **(b)** with amplifying surface characteristics.

Such results are very important from a technological point of view for the development of new materials that can work in contact with fluids. For these materials, the porosity is insured only in the direction of the cylindrical void axes (the axis x_1 here) while maintaining an identical tensile stiffness in three directions (longitudinal and transversal).

A similar amplification procedure used above is employed for an REV of $R_0 = 1nm$ with amplification of K'_S n times. The evolution of the ratio E_1/E_2 versus the factor n is presented in figure 5.12b. This figure shows, as expected, a decrease of the ratio E_1/E_2 with the factor n by crossing the unit value (the pseudo-isotropy) for each value of the volume fraction. The factor n allowing to get a pseudo-isotropy is found approximately between 13.40 and 25.58 for a volume fraction varying from 0.1 to 0.6, respectively.

As found by Kired et al. [58], these results open the door for the research of novel materials whose surface behavior is accentuated, with the aim of obtaining unexpected as well as interesting characteristics such as a pseudo-isotropy or stiffness superior to that of the parent material.

5.3.3 Spherical void with coherent interface and different surrounding material shapes:

To further validate and show the robustness of this work, this example is addressed in order to assess the effect of the shape of the surrounding medium (matrix) embedding nanovoid with coherent interface, and the effect of boundary conditions type applied to REV, on the accuracy of predictions compared to the analytical solution. In this example, the surrounding medium is supposed first of cylindrical shape containing spherical void, in accordance with the case studied by Yvonnet et al. [6] with 2D axisymmetric modeling (see Figure 5.13a). The analytical solution adopted for this problem will be that developed by Duan et al. [16], considering that the matrix is also of spherical shape which ensures an isotropic behavior of the composite. Hence, it should be noted that with a cylindrical matrix, the effective behavior is just approximated by isotropy. The analytical solution expresses the effective compressibility modulus $k^{eff} = \lambda^{eff} + (3/2) \mu^{eff} = (C_{11} + C_{12} + C_{13})/3$ as follows [16]:

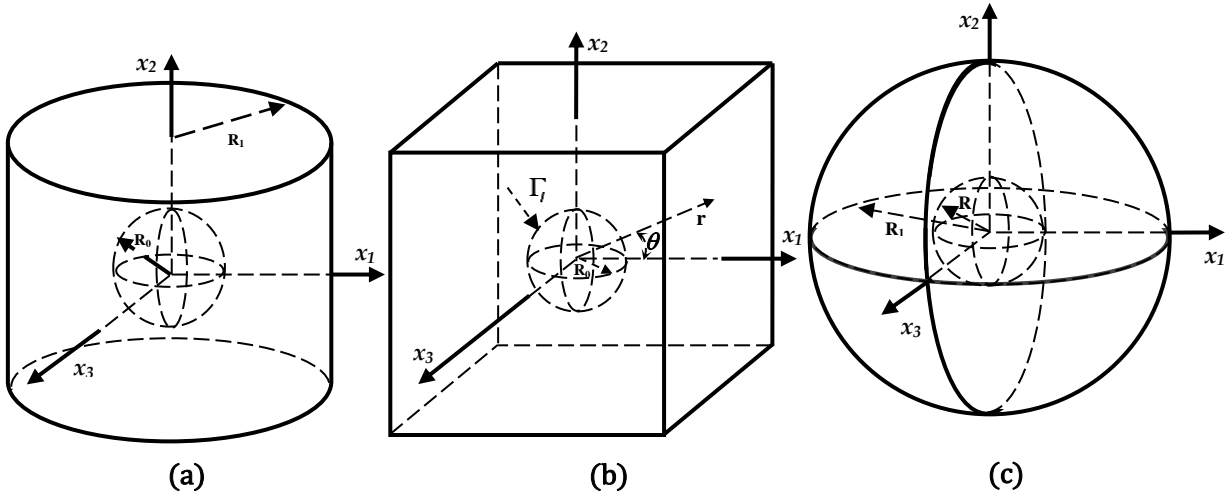


Fig.5.13: Spherical void with coherent interface: **(a)** Into cylindrical matrix; **(b)** Into cubic matrix; **(c)** Into spherical matrix.

$$\mathbf{k}^{eff} = \frac{3k^I(3k^M + 4fk^M)}{3[3(1-f)k^I + 3fk^M + 2\mu^M(2+k_r^S - fk_r^S)]} + \frac{2\mu^M[4f\mu^M k_r^S + 3k^M(2-2f+k_r^S)]}{3[3(1-f)k^I + 3k^M + 2\mu^M(2+k_r^S - fk_r^S)]} \quad (5.44)$$

In Eq. (5.44) $k_r^s = k^s / (R_0 \mu^M)$, the superscripts S, M and I denote the interface, the matrix and the inhomogeneity, respectively.

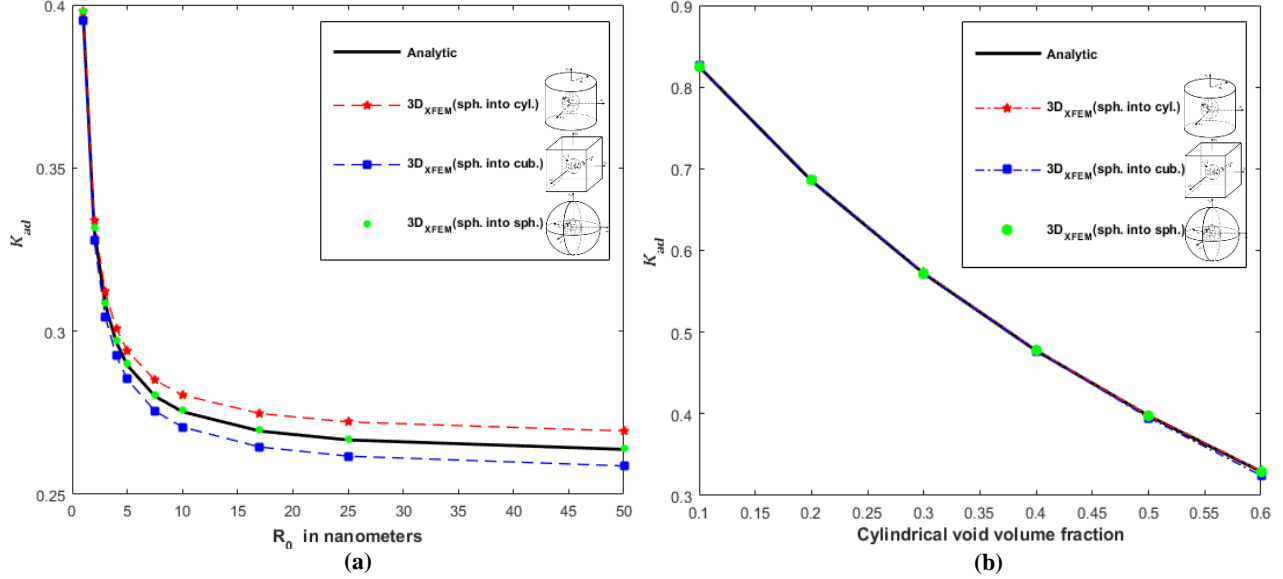


Fig.5.14: Dimensionless effective bulk modulus for different REV configurations and $K_s' > 0$: **a)** with respect to void size; **b)** with respect to volume fraction.

For the same elastic constants of the matrix and of the interface used in example 5.4.2, the evolution of $K_{ad} = k_{eff}/k_M$ is evaluated as a function of the void radius R_0 for $f = 0.5$ by the present approach and compared with that obtained numerically by Yvonnet et al. [6], and analytically by Duan et al. [16]. This elastic modulus will also be evaluated as a function of f for $R_0 = 1nm$. It should be mentioned that the non-cubic form of the REV employed here does not make it possible to use periodic boundary conditions. Therefore, a uniform strain boundary conditions, given by equations (5.43) with $\epsilon_{22}^0 = 1$, will be used.

Other matrix forms can be tested, such as the spherical shape (to get closer to the isotropic behavior) and the cubic form with periodic boundary conditions (to test the effect of the latter). These two configurations are described in Figure 5.13b and 5.13c. The different results are grouped in Figures 5.14-5.16.

Figures 5.14-5.16 show overall a remarkable agreement between the different results obtained with the different types of matrices; cylindrical, cubic and spherical, with a better

precision for the last type compared to the analytical solution especially for the curves giving k_{ad} versus R_0 . This is expected since the analytical solution provided by Duan et al. [59] assumes the matrix is spherical. Thus, the effect of the shape of the matrix as well as the type of the boundary conditions applied on REV can be significant only with respect to the size void, especially when the embedded void is large enough (see Figures 5.14a, 5.15a, 5.16a).

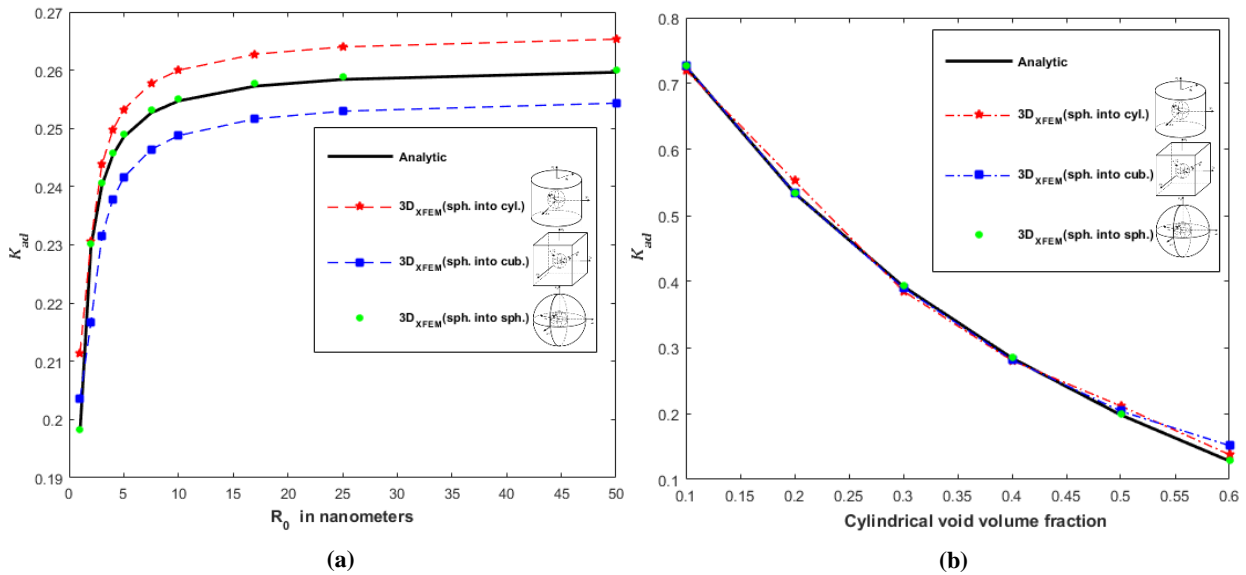


Fig.5.15: Dimensionless effective bulk modulus for different REV's configurations and $K_s' < 0$: **a)** with respect to void size; **b)** with respect to volume fraction.

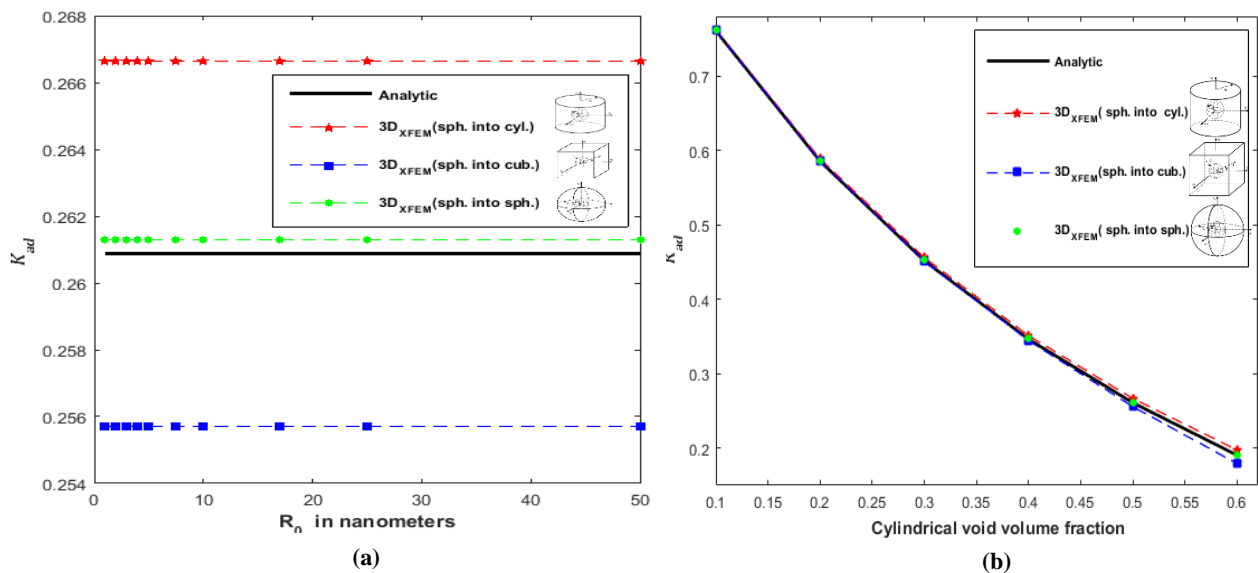


Fig.5.16: Dimensionless effective bulk modulus for different REV's configurations and $K_s' = 0$: **a)** with respect to void size; **b)** with respect to volume fraction.

5.3.4 Effect of flattening of nanovoids:

The aim of this part is first to analyze the effect of the flattening of voids on the effective behavior of nanoporous materials with taking into account the surface energy contribution of the coherent interface. The second objective of this application is to show the link between an extremely flat void and a crack of similar size with regard to the computed effective property. Another goal through this example is to assess the influence of the surface energy when the nanovoid is successively flattened. Finally, a convergence speed test is carried out here in order to show the interest regarding the numerical cost of replacing very flat voids by cracks, modeled by using the Heaviside-type enrichment in XFEM.

In this example, the effective behaviour of REV's containing flattened spherical void, flattened cylindrical void, penny shaped crack or through straight crack is analyzed for the same mechanical properties as in example 5.4.2. The instability of the numerical results due to ill-conditioning system of equations for $K'_s < 0$, leads us to consider only the cases $K'_s > 0$ and $K'_s = 0$. In the case of a crack, the displacement field is described by the equation (3.5-3.6) [24, 41, 60].

5.3.4.1 Spherical void flattened to a penny shaped crack:

The first case concerns a cube containing a spherical void gradually flattening along the x_1 direction (see Figure 6.17). For this case we define a flattening coefficient of the ellipsoid F_{apl} (major axis/small axis) and a surface fraction f_s (the projection area of the ellipsoid according to x_1 / the area of the cube face of normal x_1). This cube is subjected to six periodic conditions according to equations (2.21), which are applied independently; three longitudinal strains ($\epsilon_{11}^0, \epsilon_{22}^0, \epsilon_{33}^0$) along the principal axes (x_1, x_2, x_3) and three angular strains ($\epsilon_{12}^0, \epsilon_{23}^0, \epsilon_{13}^0$) in the three principal planes. For geometric reasons, including strong flattening ($F_{apl} > 10$), the mesh density should be densified in order to avoid elements doubly cut by the interface. For this intensive computation, a mesh exceeding 3 million elements is adopted here, so that to ensure the results reliability.

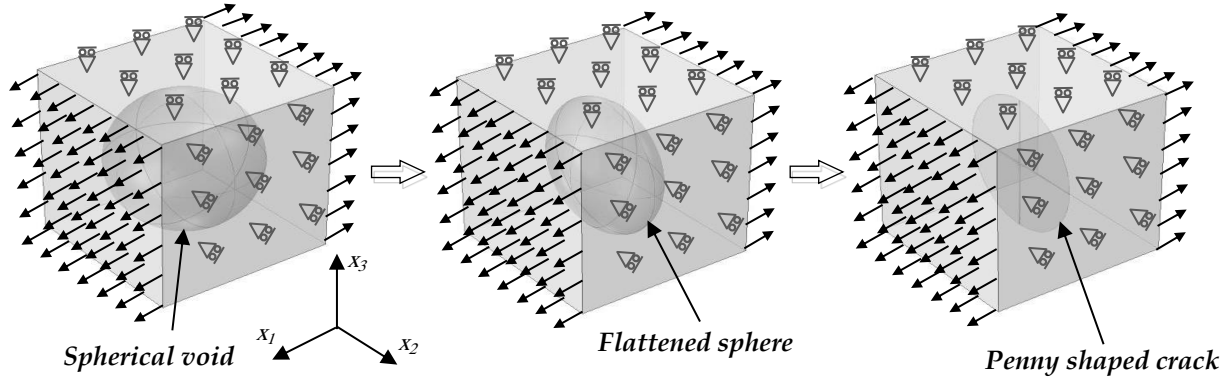


Fig.5.17: Progressive flattening of spherical void in an REV subjected to periodic conditions.

The numerical values of the dimensionless effective matrix $\mathbf{C}_{eff}^* = \mathbf{C}_{eff}/E^M$ (E^M is the Young's modulus of the composite matrix) as a function of the flattening parameterized by F_{apl} for $f_s = 0.3$ are presented as follows:

For $K_s = 0$

$$\mathbf{C}_{eff}^* = \begin{matrix} & F_{apl} = 1 & & F_{apl} = 5/3 & & F_{apl} = 5 & & F_{apl} = 20 \\ \begin{bmatrix} 1.201 & 0.568 & 0.568 & 0 & 0 & 0 \\ & 1.201 & 0.569 & 0 & 0 & 0 \\ & & 1.201 & 0 & 0 & 0 \\ & & & 0.296 & 0 & 0 \\ \text{Sym.} & & & & 0.296 & 0 \\ & & & & & 0.296 \end{bmatrix} & \Rightarrow & \begin{bmatrix} 1.224 & 0.596 & 0.596 & 0 & 0 & 0 \\ & 1.315 & 0.633 & 0 & 0 & 0 \\ & & 1.316 & 0 & 0 & 0 \\ & & & 0.326 & 0 & 0 \\ \text{Sym.} & & & & 0.331 & 0 \\ & & & & & 0.331 \end{bmatrix} & \Rightarrow & \begin{bmatrix} 1.216 & 0.584 & 0.585 & 0 & 0 & 0 \\ & 1.386 & 0.654 & 0 & 0 & 0 \\ & & 1.386 & 0 & 0 & 0 \\ & & & 0.353 & 0 & 0 \\ \text{Sym.} & & & & 0.363 & 0 \\ & & & & & 0.363 \end{bmatrix} & \Rightarrow & \begin{bmatrix} 1.180 & 0.575 & 0.575 & 0 & 0 & 0 \\ & 1.394 & 0.644 & 0 & 0 & 0 \\ & & 1.394 & 0 & 0 & 0 \\ & & & 0.375 & 0 & 0 \\ \text{Sym.} & & & & 0.368 & 0 \\ & & & & & 0.368 \end{bmatrix} \end{matrix}$$

For $K_s > 0$

$$\mathbf{C}_{eff}^* = \begin{matrix} & F_{apl} = 1 & & F_{apl} = 5/3 & & F_{apl} = 5 & & F_{apl} = 20 \\ \begin{bmatrix} 1.072 & 0.457 & 0.457 & 0 & 0 & 0 \\ & 1.072 & 0.457 & 0 & 0 & 0 \\ & & 1.072 & 0 & 0 & 0 \\ & & & 0.288 & 0 & 0 \\ \text{Sym.} & & & & 0.288 & 0 \\ & & & & & 0.288 \end{bmatrix} & \Rightarrow & \begin{bmatrix} 1.130 & 0.516 & 0.516 & 0 & 0 & 0 \\ & 1.219 & 0.541 & 0 & 0 & 0 \\ & & 1.219 & 0 & 0 & 0 \\ & & & 0.332 & 0 & 0 \\ \text{Sym.} & & & & 0.316 & 0 \\ & & & & & 0.316 \end{bmatrix} & \Rightarrow & \begin{bmatrix} 1.177 & 0.557 & 0.557 & 0 & 0 & 0 \\ & 1.343 & 0.608 & 0 & 0 & 0 \\ & & 1.343 & 0 & 0 & 0 \\ & & & 0.367 & 0 & 0 \\ \text{Sym.} & & & & 0.345 & 0 \\ & & & & & 0.345 \end{bmatrix} & \Rightarrow & \begin{bmatrix} 1.214 & 0.573 & 0.573 & 0 & 0 & 0 \\ & 1.378 & 0.625 & 0 & 0 & 0 \\ & & 1.378 & 0 & 0 & 0 \\ & & & 0.377 & 0 & 0 \\ \text{Sym.} & & & & 0.365 & 0 \\ & & & & & 0.365 \end{bmatrix} \end{matrix}$$

From these results, we note that the effective behavior of the REV is transformed with the flattening from cubic symmetry to tetragonal symmetry, which can be schematized in the following way:

$$\begin{bmatrix} C_{11} & C_{12} & C_{12} & 0 & 0 & 0 \\ \square & C_{11} & C_{12} & 0 & 0 & 0 \\ \square & \square & C_{11} & 0 & 0 & 0 \\ \square & \square & \square & C_{44} & 0 & 0 \\ \square & \text{Sym.} & \square & \square & C_{44} & 0 \\ \square & \square & \square & \square & \square & C_{44} \end{bmatrix} \Rightarrow \begin{bmatrix} C_{11} & C_{12} & C_{12} & 0 & 0 & 0 \\ \square & C_{22} & C_{23} & 0 & 0 & 0 \\ \square & \square & C_{22} & 0 & 0 & 0 \\ \square & \square & \square & C_{44} & 0 & 0 \\ \square & \text{Sym.} & \square & \square & C_{55} & 0 \\ \square & \square & \square & \square & \square & C_{55} \end{bmatrix}$$

To follow the evolution of the effective behavior versus the flattening, we were interested in two linear invariants proposed by Ahmed [41], which are base independent. These invariants are also employed in several other studies [60,61]. They are defined as [26,62]:

$$A_1 = C_{11} + C_{22} + C_{33} + 2(C_{44} + C_{55} + C_{66}) \quad (5.45)$$

$$A_2 = C_{11} + C_{22} + C_{33} + 2(C_{12} + C_{13} + C_{23}) = 9k \quad (5.46)$$

According to their respective definitions, it is noted that the invariant A_1 corresponds to longitudinal stiffness associated with shear stiffness, while A_2 reflects the compressibility stiffness which comprises longitudinal stiffness contributions combined to transverse ones. These invariants are evaluated in dimensionless form as $A_i^* = A_i/E^M$ for different surface fractions $f_s = \{0.3, 0.4, 0.5, 0.6\}$ of the flattened nanovoid. The obtained results are grouped together in figure 5.18.

Several observations can be drawn from this figure:

- The invariant A_1 is systematically lower than A_2 , since the shear stiffness is generally lower than the normal transverse one.
- The surface energy favorably influences different stiffnesses comprised in invariants A_1 and A_2 for different values of surface fraction.
- The different invariants decrease with the surface fraction, corresponding to a relative increase of the defect/flaw size compared to the REV.

- All the invariants evolve with the flattening to join those of a crack, and this for all the surface fractions, which implies the vanishing of the surface energy with the flattening.

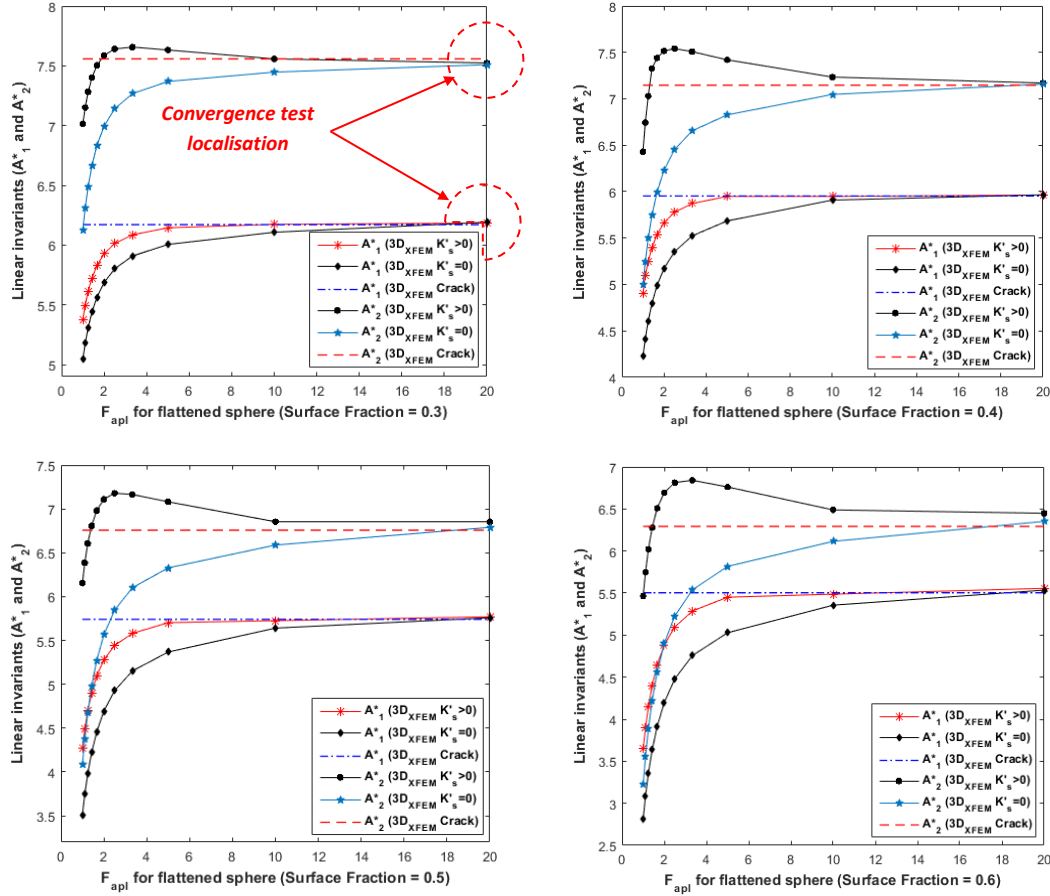


Fig.5.18: Dimensionless linear invariants versus flattening coefficient for different surface fractions.

All the invariants increase constantly with the flattening until reaching those of a crack, with the exception of the A_2 for $K'_s > 0$, which progresses with the flattening up to a maximum, located above that of a crack, then regresses to join that of a crack. This means that the surface energy affects the invariant A_2 , related only to tensile, more than A_1 which is associated with both tensile and shear.

5.3.4.2 Cylindrical void flattened to a through straight crack:

The second case is a cube containing a cylindrical void gradually flattened to have an elliptical section (see figure 5.18). A flattening coefficient of the ellipse F_{apl} is defined as major axis/small axis and a surface fraction f_s is also defined as the projection area of void / the

$$\begin{bmatrix} C_{11} & C_{12} & C_{12} & 0 & 0 & 0 \\ \square & C_{22} & C_{23} & 0 & 0 & 0 \\ \square & \square & C_{22} & 0 & 0 & 0 \\ \square & \square & \square & C_{44} & 0 & 0 \\ \square & \text{Sym.} & \square & \square & C_{55} & 0 \\ \square & \square & \square & \square & \square & C_{55} \end{bmatrix} \Rightarrow \begin{bmatrix} C_{11} & C_{12} & C_{13} & 0 & 0 & 0 \\ \square & C_{22} & C_{23} & 0 & 0 & 0 \\ \square & \square & C_{33} & 0 & 0 & 0 \\ \square & \square & \square & C_{44} & 0 & 0 \\ \square & \text{Sym.} & \square & \square & C_{55} & 0 \\ \square & \square & \square & \square & \square & C_{66} \end{bmatrix}$$

In order to follow the evolution of the effective behavior as a function of the flattening for different surface fractions $f_s = \{0.3, 0.4, 0.5, 0.6\}$, the linear invariants in dimensionless form described above were studied. The results obtained are reported together in figure 5.19.

Very similar remarks to those made for the flattening sphere of the above example can be made again, given the great qualitative similarity between the respective curves of figures 5.18 and 5.20. The difference is only of quantitative kind given the lower stiffness for the flattened cylinder especially for the invariant A_2 . This is due to the relatively small volume of the flattened sphere compared to the flattened cylinder for the same surface fraction.

5.3.4.3 Mesh refinement effect for flattening problem:

As mentioned above, the problem of void flattening, especially for high ratio, requires a very refined mesh in order to obtain an acceptable numerical convergence. To demonstrate the efficiency in this type of intensive calculation, and in the absence of an exact solution to calculate the invariants A_1 and A_2 , a convergence test between the case of a very flat void ($F_{apl} = 20$) and a crack, versus the density of the mesh is presented in figure 5.21. For the sake of brevity, the test is limited to the case $f_s = 0.3$, surrounded by red circles in figures 5.17 and 5.18. Figure 5.21 shows the interest of such intensive computation since the different parameters converge only after 2.5 million elements for the sphere flattening and 3 million elements for the cylinder flattening. It should also be noted that the calculation for the crack stabilizes much earlier than the flattened voids (at around 0.2 million elements). The interest of replacing voids that are extremely flattened by cracks of comparable size is thus demonstrated. This last remark once points out also the interest of using the XFEM with enrichments given by equations (3.5-3.6) for cracked medium.

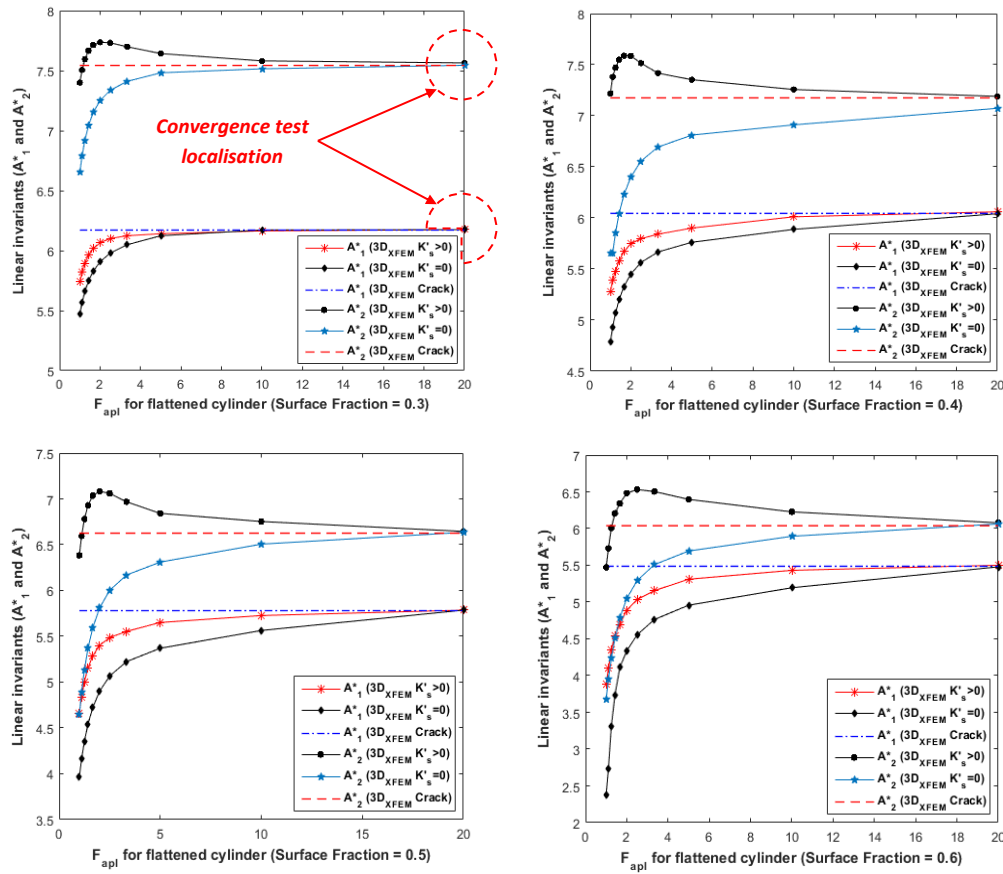


Fig.5.20: Dimensionless linear invariants versus flattening coefficient for different surface fractions.

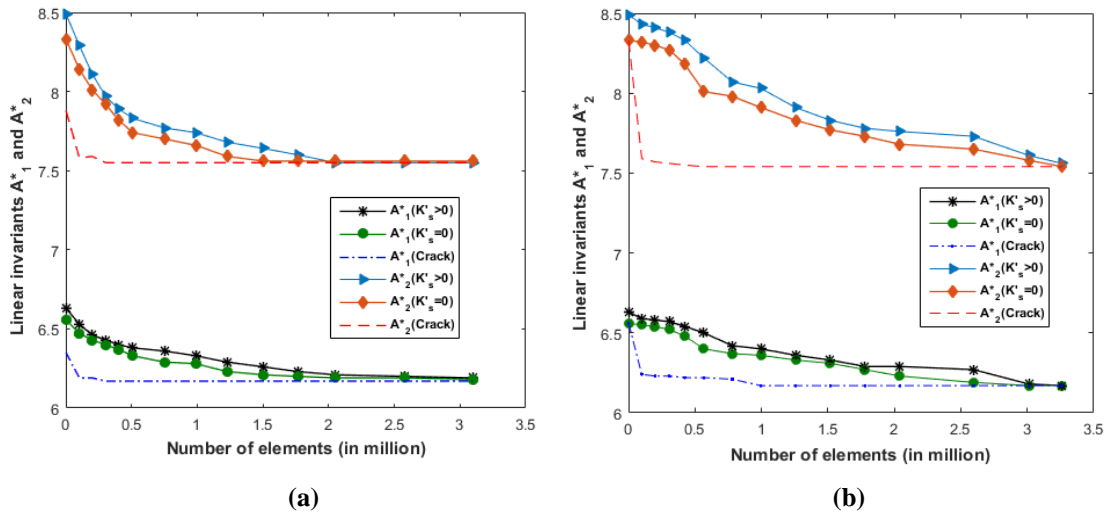


Fig.5.21: Convergence test for $f_s = 0.3$ and $F_{apl} = 20$: (a) For flattened sphere; (b) For flattened cylinder.

5.4 Conclusion:

Through the examples treated in this chapter, it was developed a 3D modeling tool for structural analysis based on XFEM/FEM combined with the Level-Set technique, dedicated in particular to numerical homogenization. This tool enables to study the effective properties of mediums containing nano-inclusions, voids and/or nanocracks.

Most of the treated problems aim to validate the developed numerical simulation code through the comparison of the obtained results with analytical and numerically ones from the literature. These comparisons have led overall to a very good agreement. The desire to highlight the contribution that the 3D aspect of this work can provide compared to other studies is constantly present in the various discussed simulations, citing among these, the analysis of the normal stiffness along the longitudinal axis of cylindrical nanovoids contained in a nanoporous material, which is rarely analyzed in literature. This allowed us to also study 3D pseudo-isotropy of such material.

The last examples addressed in this chapter concern the flattening of three-dimensional nanovoids with and without the surface energy effect. The purpose of these tests is to verify the correspondence, in terms of effective behavior, between the extremely flattened voids and cracks of comparable shape and size, as well as the impact of the surface energy for this limiting case.

Concluding remarks and outlook

Concluding remarks and outlook

In this work, it was possible to develop a 3D modelling tool for structural analysis based on XFEM/FEM combined with the Level-Set technique, dedicated in particular to numerical homogenization. This tool enables to study the effective properties of mediums containing inclusions, voids and/or cracks.

Most of the treated problems aim to validate the developed numerical simulation code through the comparison of the obtained results with analytical and numerical ones for displacement field and homogenization analysis from the literature. These comparisons have led overall to a very good agreement. The desire to highlight the contribution that the 3D aspect of this work can provide compared to other studies is constantly present in the various discussed simulations, citing among these, the analysis of the normal stiffness along the longitudinal axis of cylindrical nano voids contained in a nanoporous material, which is rarely analysed in literature. This allowed us also to study 3D pseudo-isotropy of such material.

The last examples addressed in the chapter 4 and 5 concerns the flattening of three-dimensional nanovoids with and without the surface energy effect. The purpose of these tests is to verify the correspondence, in terms of effective behavior, between the extremely flattened voids and cracks of comparable shape and size, as well as the impact of the surface energy for this limiting case. In which results are as interesting as they are comparable to those obtained here.

Among the obtained results from the various simulations carried out in chapter 4 and 5, one can point out the following:

Concluding remarks and outlook

- ✓ The obtained results were compared with those obtained using Caste3M2018 based on conventional FEM. The good agreement observed between the two methods was more than satisfactory, attesting to the accuracy and the effectiveness of the present approach.
- ✓ 3D evaluation of the impact of nanofiber surface energy on the effective properties of the composite as a function of nanofiber size, at the same time validated the plane strain (2D) modelling of the problem in this case with a wider choice of the REV's thickness (taken comparable to the transverse dimensions in this study).
- ✓ Existence of a theoretical size (below nanoscale) for which the composite containing axial voids, initially isotropic transverse or orthotropic, becomes lighter, stiffer and/or pseudo-isotropic (the same normal stiffness along the three principal directions). This unusual effective behavior can also be obtained if the elastic properties of the interface are amplified over defined ratio.
- ✓ The low effect of the shape of the matrix as well as the type of the boundary conditions applied on REV on the predicted effective behaviour of nanostructures.
- ✓ The progressive vanishing of the surface energy effect with the flattening of voids to disappear completely when they become cracks.
- ✓ Numerically evidencing that the effective behavior of nanoporous material joins that of cracked one with crack of comparable size, by flattening the nano-void.
- ✓ Regardless the presence of surface energy, the flattening of a spherical nano void transforms the REV behavior from cubic symmetry to tetragonal symmetry. While the flattening of a cylindrical nano void transforms the effective behavior from tetragonal symmetry to orthotropic symmetry.
- ✓ Reliability of the present approach as well as the present code proved by efficiency tests of numerical convergence.

Concluding remarks and outlook

✓ The numerical efficiency that is much better when simulating a crack compared to the simulation of flattened voids, thus proving the utility of the XFEM through the Heaviside-type enrichment on the additional degrees of freedom.

In the last part of this work in chapter 6, a new development was carried out concerning the interaction energy effect on the effective behaviour of composites containing nanovoids without and within the surface energy. After some validation tests, this part were dedicated to quantify the interaction energy effect on REV's containing voids randomized distributed with several configuration (three different organizing ways). All these studies are tested for tow voids shapes (spherical and cylindrical). The obtained results show that the interaction energy has an important role on symmetry kind, the rigidity, the manufacturing procedure simplicity of the studied nanocomposites.

As outlook of this work, one can imagine some suites:

- The interaction energy between voids and inclusions with presence of cracks.
- The interaction energy effect of nanostructures containing multiple random cracks.
- The study of other shapes of nanovoids (cone, cube, torus, a like-star...etc.).
- The extension of number of realizations over to 40 by using machine with higher properties.

References

References

-
- [1] K. Mozaffari, S. Yang, and P. Sharma, "Surface Energy and Nanoscale Mechanics," *Handb. Mater. Model.*, no. February, 2019. https://doi.org/10.1007/978-3-319-50257-1_48-1
- [2] R. E. Miller and V. B. Shenoy, "Size-dependent elastic properties of nanosized structural elements," *Nanotechnology*, vol. 11, no. 3, pp. 139–147, 2000.
- [3] S. Kango, S. Kalia, A. Celli, J. Njuguna, Y. Habibi, and R. Kumar, "Progress in Polymer Science Surface modification of inorganic nanoparticles for development of organic – inorganic nanocomposites — A review," *Prog. Polym. Sci.*, vol. 38, no. 8, pp. 1232–1261, 2013.
- [4] H. L. Duan, J. Wang, and B. L. Karihaloo, "Nanoporous materials can be made stiffer than non-porous counterparts by surface modification", *Acta Materialia*, vol. 54, pp. 2983–2990, 2006.
- [5] M. R. Kired, B. E. Hachi, D. Hachi, and M. Haboussi, "Effects of nano-voids and nano-cracks on the elastic properties of a host medium: XFEM modeling with the level-set function and free surface energy," *Acta Mech. Sin. Xuebao*, vol. 35, no. 4, pp. 799–811, 2019.
- [6] J. Yvonnet, H. Le Quang, and Q. C. He, "An XFEM/level set approach to modelling surface/interface effects and to computing the size-dependent effective properties of nanocomposites," *Comput. Mech.*, vol. 42, no. 1, pp. 119–131, 2008.
- [7] M. Farsad, F. J. Vernerey, and H. S. Park, "An extended finite element / level set method to study surface effects on the mechanical behavior and properties of nanomaterials" , *Int. J. Numer. Methods Eng.*. June, pp. 1466–1489, 2010.
- [8] G. Chatzigeorgiou, F. Meraghni, and A. Javili, "Generalized interfacial energy and size effects in composites", *Journal of the Mechanics and Physics of Solids*, vol. 106, pp. 257–282, 2017.
- [9] V. I. Kushch, S. G. Mogilevskaya, H. K. Stolarski, and S. L. Crouch, "Elastic interaction of spherical nanoinhomogeneities with GurtinMurdoch type interfaces," *J. Mech. Phys. Solids*, vol. 59, no. 9, pp. 1702–1716, 2011.
- [10] J. Yvonnet, Q. He, and C. Toulemonde, "Numerical modelling of the effective conductivities of composites with arbitrarily shaped inclusions and highly conducting interface", *Composites Science and Technology*, vol. 68, pp. 2818–2825, 2008.
- [11] X. Lu. *Modélisation électro-mécanique multi-échelle des nanocomposites graphène/polymère*. Autre. Université Paris-Saclay, 2017. Français. NNT : 2017SACL058ff. tel-01756392v2f
- [12] X. Lu, J. Yvonnet, F. Detrez, and J. Bai, "Multiscale modeling of nonlinear electric conductivity in graphene-reinforced nanocomposites taking into account tunnelling effect," *J. Comput. Phys.*, no. January, 2017.
- [13] X. Lu, F. Detrez, J. Yvonnet, and J. Bai, "graphene / polymer nanocomposites Multiscale study of influence of interfacial decohesion on piezoresistivity of graphene / polymer nanocomposites", *Modelling Simul. Mater. Sci. Eng.*, no. December, 2018.
- [14] M. Haboussi, A. Sankar, and M. Ganapathi, "Nonlinear axisymmetric dynamic buckling of functionally graded graphene reinforced porous nanocomposite spherical caps," *Mech. Adv. Mater. Struct.*, vol. 0, no. 0, pp. 1–14, 2019.
- [15] M. E. Gurtin and A. Ian Murdoch, "A continuum theory of elastic material surfaces," *Arch. Ration. Mech. Anal.*, vol. 57, no. 4, pp. 291–323, 1975.
- [16] S. Ren, J. Liu, S. Gu, and Q. He, "An XFEM-based numerical procedure for the analysis of poroelastic composites with coherent imperfect interface", *Comput. Mater. Sci.*, 2014.
-

References

- [17] N. Sukumar, D. L. Chopp, N. Moës, and T. Belytschko, "Modeling holes and inclusions by level sets in the extended finite-element method," *Comput. Methods Appl. Mech. Eng.*, vol. 190, no. 46–47, pp. 6183–6200, 2001.
- [18] A. B. Tran et al., "A multiple level-set approach to prevent numerical artefacts in complex microstructures with nearby inclusions within XFEM. *Int. J. Numer. Methods Eng.*, Wiley, 2011, 85 (11), pp.1436-1459. 10.1002/nme.3025. hal-00692223f.
- [19] N. Moës et al., "A computational approach to handle complex microstructure geometries", *Comput. Methods Appl. Mech. Eng.*, 2016. [https://doi.org/10.1016/S0045-7825\(03\)00346-3](https://doi.org/10.1016/S0045-7825(03)00346-3)
- [20] Z. Liu, J. Oswald, and T. Belytschko, "XFEM modeling of ultrasonic wave propagation in polymer matrix particulate / fibrous composites," *Wave Motion*, vol. 50, no. 3, pp. 389–401, 2013.
- [21] D. P. Bach, D. Brancherie, and L. Cauvin, "Size effect in nanocomposites : XFEM / level set approach and interface element approach," *Finite Elem. Anal. Des.*, vol. 165, no. July, pp. 41–51, 2019.
- [22] N. Bonfils, N. Chevaugeon, N. Moës, "Treating volumetric inequality constraint in a continuum media with a coupled X-FEM / level-set strategy," *Comput. Methods Appl. Mech. Eng.*, vol. 205–208, pp. 16–28, 2012.
- [23] C. Geuzaine and J. F. Remacle, "Gmsh: A 3-D finite element mesh generator with built-in pre- and post-processing facilities," *Int. J. Numer. Methods Eng.*, vol. 79, no. 11, pp. 1309–1331, 2009.
- [24] F. Ahmad, "Invariants and structural invariants of the anisotropic elasticity tensor," *Q. J. Mech. Appl. Math.*, vol. 55, no. 4, pp. 597–606, 2002
- [25] J.B. Ever, *Finite Element Analysis of Composite Materials with Abaqus*, CRC Press, Boca Raton, 2013, <https://doi.org/10.1201/b14788>
- [26] M. R. Kired, "Contribution to the modeling of structures based on nano- composites in the presence of multiple heterogeneities," no. May, 2019.
- [26] INRS, Santé et sécurité au travail. *Médecine Mal. Infect.* 37, 14 (2007).
- [27] A. A. Griffiths, "The phenomena of rupture and flow in solids," *Masinovedenie*, no. 1, pp. 9–14, 1995.
- [28] Westergaard, H. M. Bearing pressures and cracks. *Journal of Applied Mechanics*, 6:49–53. (1939).
- [29] G.R. Irwin – Analysis of stresses and strains near the end of crack traversing a plate, *J. of Appl. Mech. Transactions*, pp.361-364, 1957.
- [30] G.I. Barenblatt. *Mathematical theory of equilibrium cracks in brittle fracture. Adv. Appl. Mec.*..7.55-129. (1962).
- [31] J.W. Hutchinson – Singular behaviour at the end of a tensile crack in a hardening material, *J. Mech. Phys. Solids*, Pergamon Press, Vol. 16, pp. 13-31,1968.
- [32] N. Calvo, F. Del Pin, S. R. Idelsohn, and O. Eugenio, "The meshless Finite element method," vol. 912, no. December 2001, pp. 893–912, 2003.
- [33] K. Mohammedi, *Méthodes Numériques Sans Maillages*, PhD thesis. University M'Hamed Bougara of Boumerdes, livre, (2017).
- [34] A. Seghir, "Cours Méthode des Éléments Finis," 2014. T. Belytschko and T. Black, "ELASTIC CRACK GROWTH IN FINITE ELEMENTS", *Int. J. Numer. Meth. Engng.*, vol. 620, no. July 1998, pp. 601–620, 1999.
- [36] N. Moës, J. Dolbow, T. E. D. Belytschko, "A FINITE ELEMENT METHOD FOR CRACK GROWTH WITHOUT REMESHING", *Int. J. Numer. Meth. Engng.*, vol. 150, no. February, pp. 131–150, 1999.
- [37] N. Sukumar, D. L. Chopp, N. Moës, and T. Belytschko, "Modeling holes and inclusions by level sets in the extended finite-element method," *Comput. Methods Appl. Mech.*

References

- Eng., vol. 190, no. 46–47, pp. 6183–6200, 2001.
- [38] J. Chessa and T. Belytschko, “Arbitrary discontinuities in space – time finite elements by level sets and X-FEM,” no. April, pp. 2595–2614, 2004.
- [39] M. Stolarska, D. L. Chopp, N. Moes, and T. Belytschko, “Modelling crack growth by level sets in the extended finite element method,” no. October 2000, pp. 943–960, 2001.
- [40] T. Belytschko, C. Parimi, N. Moes, N. Sukumar, and S. Usui, “Structured extended finite element methods for solids defined by implicit surfaces,” vol. 635, no. July 2002, pp. 609–635, 2003.
- [41] C. Chateau, L. Gélébart, M. Bornert, and J. Crépin, “Micromechanical modeling of the elastic behavior of unidirectional CVI SiC/SiC composites,” *Int. J. Solids Struct.*, vol. 58, pp. 322–334, 2015.
- [42] H. J. Böhm, “A Short Introduction to Basics Aspects of Continuum Micromechanics,” vol. 206, no. November, p. 130, 2012.
- [43] H. Le Quang and Q. C. He, “Size-dependent effective thermoelastic properties of nanocomposites with spherically anisotropic phases,” *J. Mech. Phys. Solids*, vol. 55, no. 9, pp. 1899–1931, 2007.
- [44] H. Le Quang and Q. C. He, “Estimation of the effective thermoelastic moduli of fibrous nanocomposites with cylindrically anisotropic phases,” *Arch. Appl. Mech.*, vol. 79, no. 3, pp. 225–248, 2009.
- [45] D. M. Benziane, . Nouvelle approche pour la modélisation des problèmes multi-échelles en mécanique : la méthode 95/5. Sciences de l’ingénieur [physics]. Arts et Métiers ParisTech, 2007. Français. ffnNT : 2007ENAM0007ff. ffpastel-00002617f.
- [46] J. Yvonnet, Q. He, and C. Toulemonde, “Numerical modelling of the effective conductivities of composites with arbitrarily shaped inclusions and highly conducting interface,” vol. 68, pp. 2818–2825, 2008.
- [47] Samull G., Approche X-FEM pour la fissuration sous contact des structures industrielles. PhD thesis. L’école central de Nantes: (2006). http://www.imsia.cnrs.fr/IMG/pdf/These_SIAVELIS.pdf.
- [48] Awais A., eXtended Finite Element Method (XFEM) Modelling arbitrary discontinuities and Failure analysis. Master Degree, Istituto Universitario di Studi Superiori di Pavia, university degli studi pavai. (2009). <http://www-2.unipv.it/compmech/dissertations/ahmedmsc.pdf>.
- [49] Geuzaine C., Remacle J. F., Gmsh Reference Manual; A finite Element Mesh Generator with Built-in Pre- and Post-Processing Facilities, Edition 4.4.1, <http://gmsh.info/doc/texinfo/gmsh.html>, 25 July 2019.
- [50] Belytschko .T, Parimi C., Moës N., Sukumar N. and Usui S., Structured extended finite element methods for solids defined by implicit surfaces. *international journal for numerical methods in engineering* *Int. J. Numer. Meth. Engng* 2003; 56:609–635, DOI: 10.1002/nme.686.
- [51] M. E. Gurtin and A. Ian Murdoch, “A continuum theory of elastic material surfaces,” *Arch. Ration. Mech. Anal.*, vol. 57, no. 4, pp. 291–323, 1975.
- [52] Y. Benveniste, “A general interface model for a three-dimensional curved thin anisotropic interphase between two anisotropic media,” *J. Mech. Phys. Solids*, vol. 54, no. 4, pp. 708–734, 2006.
- [53] W. Gao, S. Yu, and G. Huang, “Finite element characterization of the size-dependent mechanical behaviour in nanosystems,” *Nanotechnology*, vol. 17, no. 4, pp. 1118–1122, 2006.
- [54] A.E. Benkhechiba, M. Guesmia, B.E. Hachi, D. Hachi, and M. Moussaoui, “Contribution to the modelling and homogenization of 3D structures in the presence of flaws by XFEM”, *Engineering Failure Analysis*, vol. 107, 2020.

References

- [55] P. Sharma and S. Ganti, "Size-dependent eshelby's tensor for embedded nano-inclusions incorporating surface/interface energies," *J. Appl. Mech. Trans. ASME*, vol. 71, no. 5, pp. 663–671, 2004.
- [56] I. Babuška, U. Banerjee, and K. Kergrene, "Strongly stable generalized finite element method: Application to interface problems," *Comput. Methods Appl. Mech. Eng.*, vol. 327, pp. 58–92, 2017.
- [57] G. Chatzigeorgiou, F. Meraghni, and A. Javili, "Generalized interfacial energy and size effects in composites", *Journal of the Mechanics and Physics of Solids*, vol. 106, pp. 257–282, 2017.
- [58] M. R. Kired, B. E. Hachi, D. Hachi, and M. Haboussi, "Influence des nano-vides et des nano-fissures sur les constantes élastiques effectives d'un milieu : Approche numérique par XFEM et Level-Set", *CFM2019*, pp. 1–9, 2019.
- [59] H. L. Duan, J. Wang, Z. P. Huang, and B. L. Karihaloo, "Size-dependent effective elastic constants of solids containing nano-inhomogeneities with interface stress," *J. Mech. Phys. Solids*, vol. 53, no. 7, pp. 1574–1596, 2005.
- [60] M. Ahmad, R. Faiz, and A. Naila, "Linear Invariants of a Cartesian Tensor Under $SO(2)$, $SO(3)$ and $SO(4)$ ", *Int. J. Theor. Phys.*, pp. 479–487, 2011
- [61] G.J. Dvorak, *Micromechanics of Composite Materials*. 2013. DOI 10.1007/978-94-007-4101-0 .
- [62] Q. He, "DECOMPOSITION OF ELASTICITY TENSORS AND TENSORS THAT ARE STRUCTURALLY INVARIANT", *Quar. J. Mech. Appl. Math.*, vol. 59, no. 3, 2006.
- [63] F. Chalou and F. Montheillet, "The Interaction of Two Spherical Gas Bubbles in an Infinite Elastic Solid," *J. Appl. Mech. Trans. ASME*, vol. 70, no. 6, pp. 789–798, 2003.
- [64] R. Lasser, *Tritium in Metals and Helium-3*. 1989. Springer series in materials science; v.9). DOI: 10.1007/978-3-642-73510-3.
- [65] V. C. Orsini and M. A. Zikry, "Void growth and interaction in crystalline materials," *Int. J. Plast.*, vol. 17, no. 10, pp. 1393–1417, 2001.
- [66] W. Gao, S. Yu, and G. Huang, "Finite element characterization of the size-dependent mechanical behaviour in nanosystems," *Nanotechnology*, vol. 17, no. 4, pp. 1118–1122, 2006.

Appendix A1: Some pictures of the developed code interface.

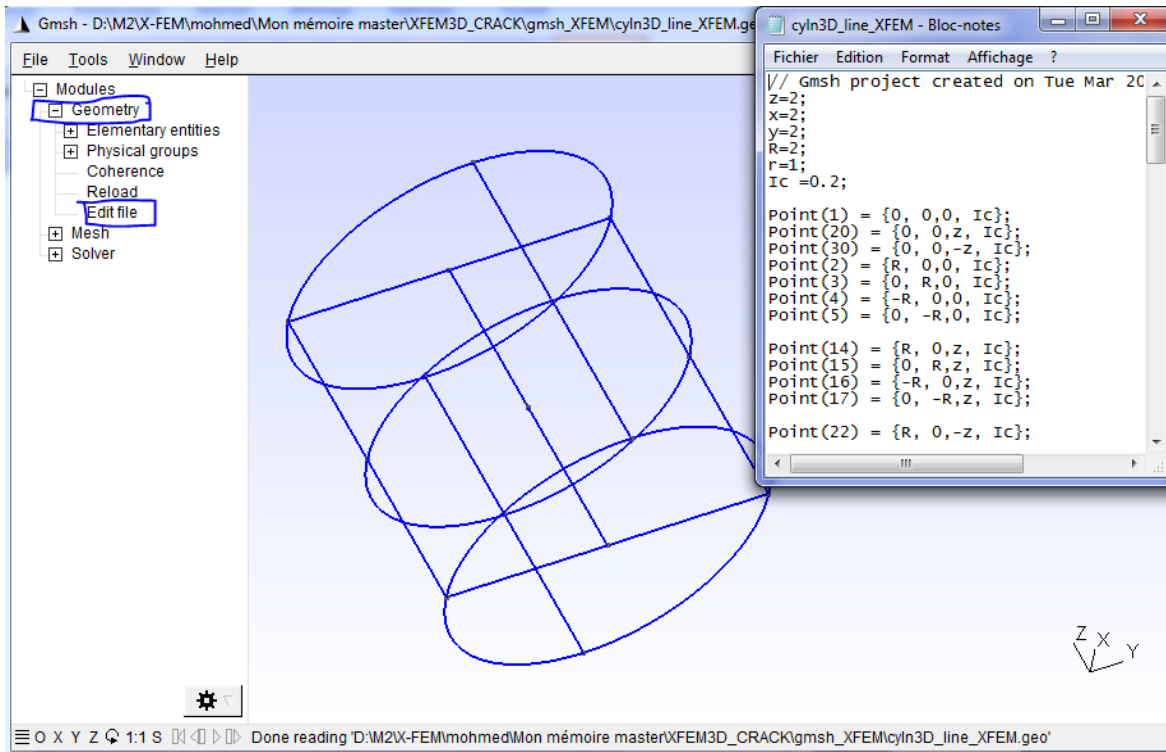


Fig.1: Definition geometry using text file.

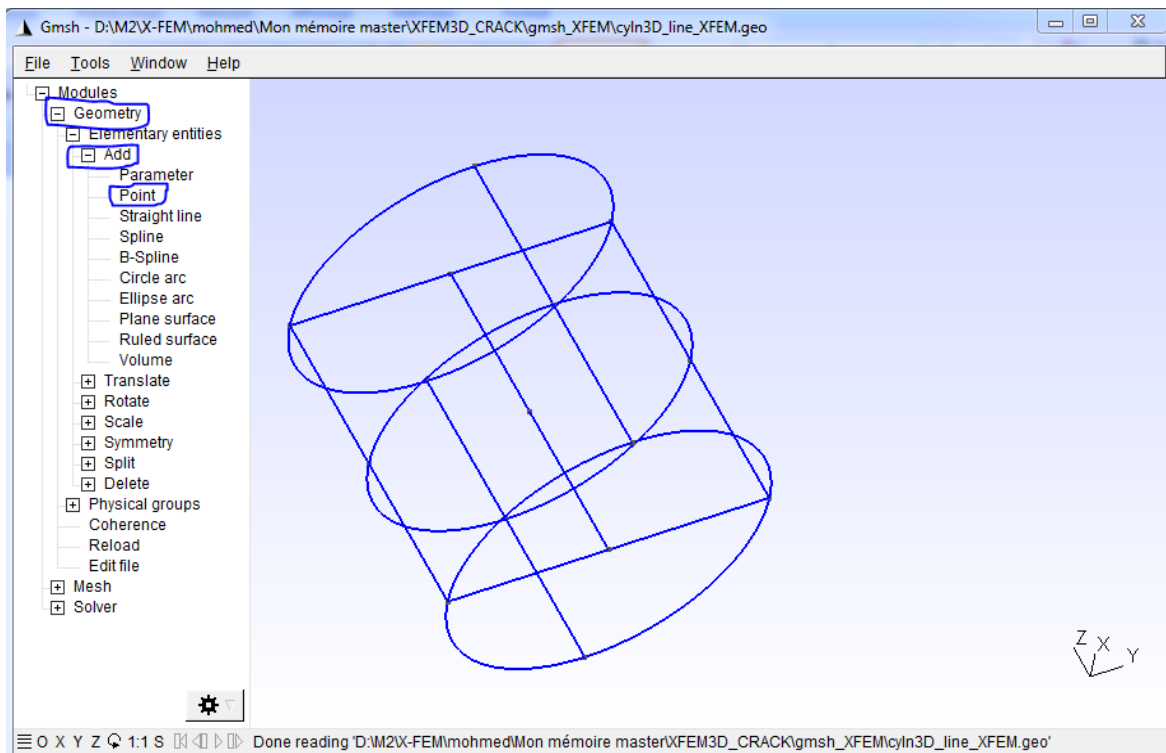


Fig.2: Definition of geometry at the level of the graphical interface of G-msh

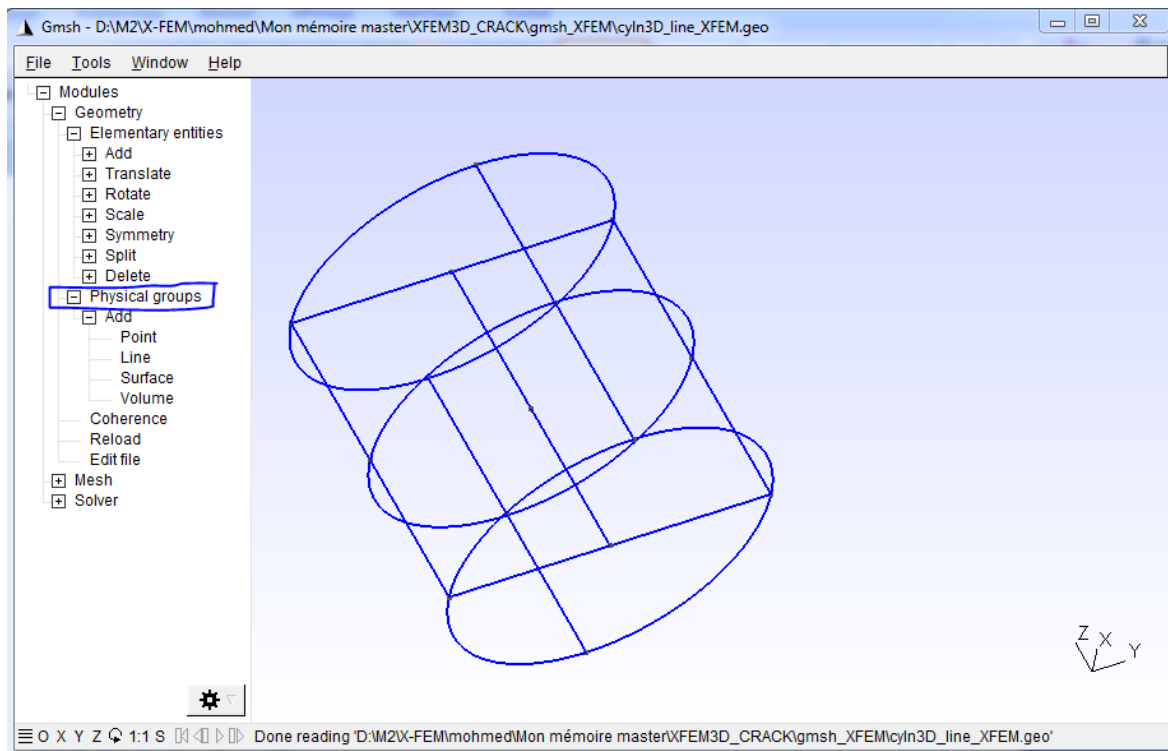


Fig.3: Selection of physical groups.

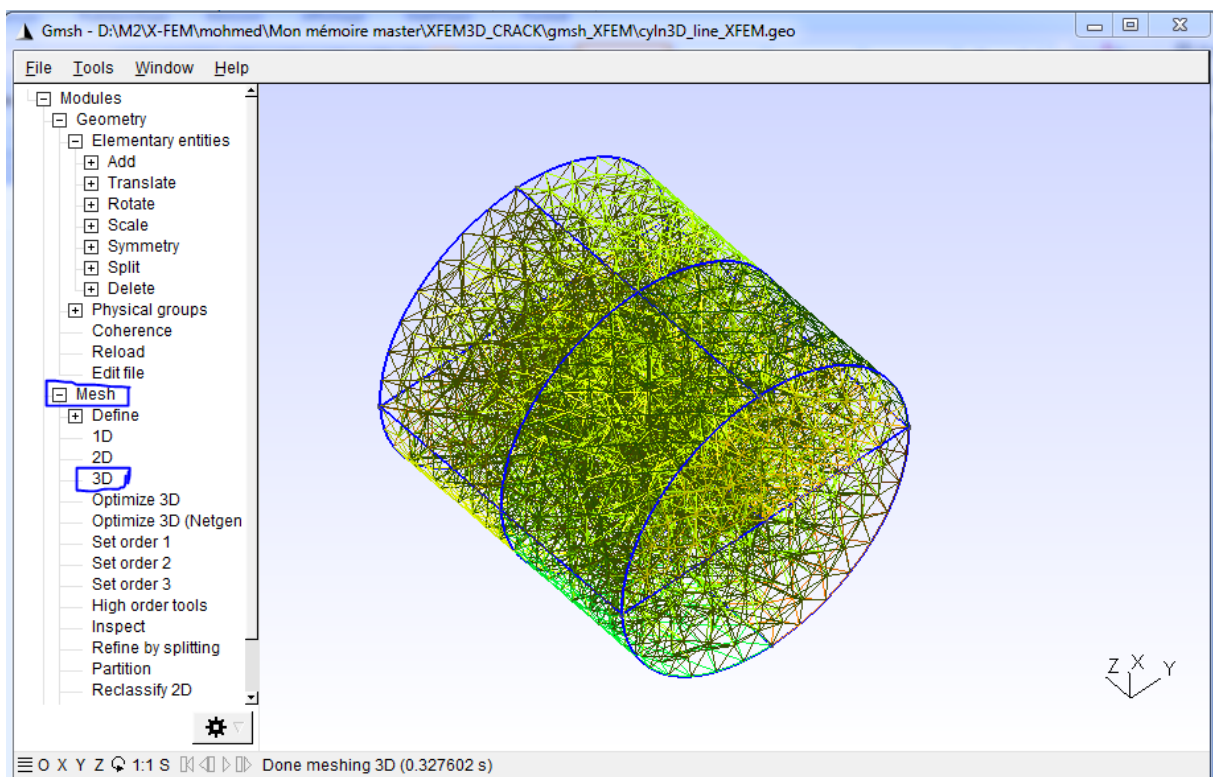


Fig.4: Mesh generation

Appendix A2: Flowchart for the different adapted configurations of the randomized distributions of voids.

